

Impact of casting parameters and chemical composition on the solidification behaviour of Al-Si-Cu hypoeutectic alloy

Dissertation

zur Erlangung des akademischen Grades

**Doktoringenieurin / Doktoringenieur
(Dr.-Ing.)**

von Dipl.-Ing. Jelena Pavlovic-Krstic
geb. am 02.01.1979. in Zajecar, Serbien

genehmigt durch die Fakultät für Maschinenbau

der Otto-von-Guericke-Universität Magdeburg

Gutachter:

Prof. Dr.-Ing. habil Rüdiger Bähr
Prof. Dr.-Ing. Klaus Eigenfeld
Dr.-Ing. Mile Djurdjevic

Promotionskolloquium am 19.03.2010

Preface

This Thesis was done at the University of Magdeburg, the Faculty of Mechanical Engineering, during my three years stay and involvement as a researcher at the Institute for Manufacturing Technologies and Quality Assurance. My PhD Thesis is focused on the solidification behaviour and the parameters controlling the solidification features of Al-Si-Cu alloy with special emphasis on the secondary dendrite arm spacing. Throughout the three years period of my PhD work, the results have been published in national and international journals as well as in national and international conference proceedings.

The research and experimental work was carried out under the supervision of Prof. Dr.-Ing. Rüdiger Bähr.

It is the greatest honour to be able to work under supervision of Prof. Dr.-Ing. Rüdiger Bähr. I am gratified him for accepting my application and involved me to work on the project in cooperation with the Nemak company from where come the major motivation for my PhD Thesis. I would like to thank Prof. Bähr for all of his help, assistance, inspiration and guidance on the all aspects.

Beside Prof. Bähr, I own my special gratitude to Dr.-Ing. Mile Djurdjevic, from the Nemak, Linz with whom I was closely working during all my PhD work. His help on my PhD Thesis was invaluable and I am grateful him for his encouragement and friendship.

I would also like to thank Prof. Eigenfeld from the Technische Universität Bergakademie Freiberg for accepting to be co-referee of this thesis.

I sincerely thank Dr.-Ing Glenn Byczinsky from Nemak Canada for his advice and help throughout my research.

I am especially grateful to my colleague Jörg Holze who helped me a lot during the experimental work in the casting laboratory and who was always very good friend. I express my gratitude to my colleagues, academic and technical staff in the Department who helped me so sincerely in the course of my research.

Above all, I would like to thank my whole family who always supported all my decisions and my scientific activities. To my husband I owe so much and there are no words to express my feelings for his love and never-ending support and belief in me.

Magdeburg, 2009

Abstract

The use of cast aluminum alloys in automotive structural applications is growing rapidly because of the need to reduce weight. The service life of a aluminum cast component is determined by the size, form and distribution of microstructure features throughout the casting, especially in those regions that are critically stressed. Grain size, secondary dendrite arm spacing (SDAS), distribution of phases, the presence of secondary phases or intermetallic compounds, the morphology of silicon particles (size, shape and distribution) and finally, defects (firstly, porosity) play a key role in the behavior of aluminum alloys under static and dynamical loads. Basically, finer microstructure features (lower SDAS values) leads to better mechanical properties.

Although the SDAS is not only factor affecting the mechanical properties of Al-Si alloys, in recent years the researchers have turn special attention to this microstructure feature. Unlike the other microstructure features, SDAS values is quite well correlated the static properties (R_m , A%) as well as fatigue life time of casting components, i.d. lower SDAS higher R_m and A% and longer fatigue life time. In addition to, it was found that SDAS decrease leads to the reduction of porosity in the sample and the quantity of detrimental intermetallic phases, Al_5FeSi (the phase is considered as one of stress concentration factors in aluminum alloy).

Because of the evident importance of SDAS, more and more automotive companies have defined a SDAS limit in their engineering specifications for aluminium castings, engine parts such as cylinder head. Concerning to demand of SDAS automotive companies have defined their own but very stringent demands for SDAS in the area of combustion chamber surface which is thermally and mechanically stressed parts in cylinder heads.

The majority of this PhD thesis is focused on the parameters controlling the value of SDAS in Al-Si7-Cu3 hypoeutectic alloys which is used for production of cylinder heads. The cooling rate/solidification time is certainly a parameter that strongly affects the SDAS. In this work the solidification time has been varied through the variation of the mold temperature and cooling condition. The effect of pouring temperature on SDAS in Al-Si7-Cu3 melt has been also examined.

Although the cooling rate has a leading role as a parameter, mostly the experimental work in this PhD Thesis has been focused on the examination of the chemical composition variation in on the SDAS value in AlSi7Cu3 alloy. This effect is not easy recognized due to the leading effect of the cooling rate, but it has been shown in this work that effect of chemical

composition couldn't be neglected. The thermal analysis and microstructure analysis was used. Since, the effect of the chemistry on the SDAS and other solidification features such as α Al- dendrite nucleation (liquidus) temperature, Dendrite Coherency Point (DCP), Al-Si eutectic nucleation temperature, Al-Cu eutectic temperature and solidus temperature has not been extensively investigated in the literature, this PhD thesis deals particularly with that problematic. The obtained results reveal that decrease of pouring temperature from 750 to 650 °C reduces the SDAS value in Al-Si7-Cu3 alloy about 6 μm . The variation of mold temperature as 250, 300, 350°C with and without water cooling of the mold show that decrease of mold temperature from 350 to 250 °C without water cooling of mold reduce the SDAS value in AlSi7Cu3 alloy from 25.9 to 19.2 μm . In the presence of water cooling, the SDAS values are lowered from 22.2 to 19 μm , that indicates the pure effect of mold temperature is diminished in the presence of water cooling although the results are related to the finer SDAS. The alloying elements investigated has ranged as: Si (7-9 wt%), Cu (1-4 wt%), Mg (0.2-3.0 wt%), Ti (0.08-0.14 wt%), Zn (0.8-3.0 wt%) and Sr (0-210 ppm). It was found that major alloying elements, Si and Cu strongly shift the SDAS to lower values, but surprising effect of Ti, Mg and Zn on SDAS has been observed. The similar trend has been found in the case of DCP point which lowered as the content of Si, Cu, Mg, Zn and Ti increases, while the addition of Sr did not influence the SDAS and DCP. Additionally, the kinetic parameter defined as time difference between time corresponding to the DCP point and Al-Si eutectic nucleation point is highly correlated to the SDAS. On the contrary, such trend was not been noticed by total solidification time as a function of chemistry. In that event, one novel kinetic parameter of controlling dendritic growth could be taken into consideration when the effect of chemistry is analysed.

Kurzfassung

Die Verwendung von Aluminium-Legierungen in der Automobileindustrie wächst rapide, Ziel ist es, Bauteile mit geringerem Gewicht zu produzieren. Die Lebensdauer eines Aluminium-Gussteiles wird durch die Größe, Form und Verteilung der mikrostrukturellen Merkmale im gesamten Bereich des Gussteiles ermittelt, insbesondere in jenen Regionen, die kritisch beansprucht werden. Korngröße, sekundärer Dendritenarmabstand (SDAS), die Verteilung der Phasen, das Vorhandensein von sekundären Phasen oder intermetallischen Verbindungen, die Morphologie der Silizium-Partikel (Größe, Form und Verteilung) und schließlich Mängel (Porosität) spielen eine wichtige Rolle beim Verhalten von Aluminium-Legierungen unter statischen und dynamischen Beanspruchungen. Grundsätzlich führen feinere Mikrostrukturmerkmale (SDAS niedrigeren Werte) zu besseren mechanischen Eigenschaften.

Obwohl der SDAS nicht der einzige Parameter ist, der die mechanischen Eigenschaften von Al-Si Legierungen beeinflusst, fokussieren Forscher ihre Aufmerksamkeit besonders in den letzten Jahren zunehmend auf diese Mikrostrukturmerkmale. Im Gegensatz zu anderen Mikrostrukturmerkmalen werden durch SDAS Werte die mechanischen Eigenschaften (Zugfestigkeit, R_m und Bruchdehnung, $A\%$) sowie Lebensdauer von Gussteilen stark beeinflusst. Es gilt deshalb bei niedriger SDAS höheren R_m und $A\%$ und längere Lebensdauer des Bauteils. Zusätzlich dazu wurde festgestellt, dass die Reduzierung des SDAS zur Verringerung der Porosität in und der Menge der schädlichen intermetallischen Phasen, Al_5FeSi in der Probe führt.

Wegen der offensichtlichen Bedeutung des SDAS haben immer mehr Unternehmen der Automobilindustrie eine SDAS-Obergrenze in ihrer technischen Spezifikationen für Aluminium-Gussteile, Motorenteile wie z.B. der Zylinderkopf festgelegt. Automobilunternehmen haben ihre individuellen und sehr strikten Anforderungen an den SDAS im Brennraumberiech. Diese ist mit der thermischen und mechanischen Beanspruchung in diesem Bereich der Zylinderköpfe zu begründen.

Der größte Teil der vorliegenden Doktorarbeit konzentriert sich auf die SDAS Werte der untereutektischen $AlSi7Cu3$ Legierungen, die für die Produktion von Zylinderköpfen genutzt wird. Die Abkühlgeschwindigkeit bzw. Erstarrungszeit ist der maßgebende Parameter, welche die SDAS-Bildung stark beeinflusst. In dieser Arbeit wurde die Erstarrungszeit untersucht, das Hauptaugenmerk lag hierbei auf die Variation der Werkzeugwandtemperatur und den

Abkühlungsbedingungen. Zu anderem wurde der Effekt der Gießtemperatur auf den SDAS in der AlSi7Cu3 Schmelze untersucht.

Bei Untersuchungen im Bereich der Abkühlgeschwindigkeit wurde folgende Ergebnisse festgestellt: Es zeigt sich, dass die Abnahme der Gießtemperatur von 750 bis 650 °C die SDAS Wert in AlSi7Cu3 Legierung ca. 6 µm reduziert. Es wurde eine Variation der Werkzeugwandtemperatur von 250, 300, 350 °C mit und ohne Wasserkühlung des Werkzeugs zeigen, dass die Abnahme der Werkzeugwandtemperatur von 350 bis 250 °C ohne Wasserkühlung durchgeführt. Es zeigte sich, dass bei einer Abnahme der Werkzeugwandtemperatur von 350 auf 250 °C ohne Wasserkühlung zu Verringerung des SDAS Wert von 25,9 bis 19,2 µm führte. Mit Einsatz der Wasserkühlung ließen sich die SDAS Werte nochmals von 22,2 auf 19 µm reduzieren.

Obwohl die Abkühlgeschwindigkeit eine wichtige Rolle spielt, wurde vor allem in den experimentellen Arbeiten dieser Dissertation das Augenmerk auf die chemische Zusammensetzung der AlSi7Cu3 Legierung gelegt. Dieser Punkt ist noch nicht tiefgründig untersucht. Es wird deshalb in dieser Arbeit gezeigt, dass der Effekt der chemischen Zusammensetzung nicht vernachlässigt werden darf.

Da die Wirkung der chemische Zusammensetzung auf den SDAS und andere Erstarrungsmerkmale wie Al- α -Dendriten Keimbildung (Liquidus)-Temperatur, Dendritenkohärenzpunkt (DCP), Al-Si-Eutektikum-Keimbildungstemperatur, Al-Cu-Eutektischen-Temperatur und Solidustemperatur nicht in der Literatur ausführlich untersucht wurden, befasst sich die vorliegende Dissertation insbesondere mit dieser Problematik.

Die Legierungselemente der untersuchten Legierung befinden sich im Bereich von: Si (7-9 Gew.%), Cu (1-4 Gew.%), Mg (0,2-3,0 Gew.%), Ti (0,08-0,14 Gew.%), Zn (0,8-3,0 Gew. %) und Sr (0-210 ppm). Es wurde festgestellt, dass die Hauptlegierungselemente, Si und Cu, einen entscheidenden Einfluss auf die Bildung geringerer SDAS-Werte hat. Des weiteren wurde beobachtet, dass Zn, Mg und besonders Ti einen Einfluss auf die SDAS-Bildung haben. Weiterhin ist zu erkennen, dass Si, Cu, Mg, Zn und Ti den DCP-Wert senken. Die Zugabe von Sr hat jedoch keinen Einfluss auf die SDAS und DCP-Werte. Im Fall der chemischen Zusammensetzung könnte ein neuartiger kinetischer Parameter zur Kontrollierung des dendritischen Wachstums in Betracht gezogen werden. Dieser Parameter ist definiert aus der Zeitdifferenz zwischen DCP-Punkt und dem Al-Si-Eutektikum-Keimbildungspunkt, welcher mit dem SDAS besser als die lokale Erstarrungszeit korreliert.

Content

Preface

Abstract

Kurzfassung

1. Introduction	1
2. Objectives and Motivation	3
3. Literature review	5
3.1. Aluminum and aluminum alloys	5
3.1.1. Casting alloy designation	7
3.1.2. Aluminum-Silicon-Copper (3xx) system	8
3.1.3. Casting of aluminium alloys	11
3.2. Cylinder head	13
3.2.1. Casting processes for production of aluminum cylinder heads	13
3.2.2. Function of cylinder head in car engine	15
3.2.3. Materials/alloys selection for car engine cylinder head	17
3.2.4. Requested metallurgical and mechanical characteristics	18
3.3. Solidification features of aluminum and aluminum alloys	21
3.3.1. Nucleation and growth of α -aluminum phase	22
3.3.2. Morphological instability of solid-liquid interface – constitutional undercooling	25
3.3.3. Primary and secondary dendrite arm spacing	32
3.3.4. Solidification features of Al-Si-Cu alloys with the emphasis on dendrite coherency	36

3.3.5. Modelling of microstructure parameters	42
4. Experimental part	44
4.1. Design of laboratory experiments	44
4.2. Experimental procedure	46
4.2.1. Materials	46
4.2.2. Industrial tests - tilt pouring die casting process	47
4.2.3. Laboratory tests in permanent metal mold	50
4.2.4. Laboratory tests in ceramic mold	53
4.3. Experimental methods and techniques	54
4.3.1. Thermal analysis	54
4.3.2. Chemical analysis	57
4.3.3. Metallographic analysis	59
4.3.3.1. Light optical microscopy and Image analysis	59
4.3.3.2. Scanning electron microscopy – Energy Dispersive X-ray analysis	61
4.3.4. Computer tomography (CT) method	63
4.3.5. Simulation method	66
5. Results and discussion	68
5.1. Microstructure characterization of the basic AlSi7Cu3 alloy- LOM, SEM-EDX and CT results	68
5.2. Results of tilt pouring die casting process	76
5.2.1. Computer-aided cooling curves in cylinder head	76
5.2.2. Secondary dendrite arm spacing in cylinder head	77
5.3. Results of laboratory tests in permanent mold	79
5.3.1. The effect of mold temperature and cooling conditions on secondary dendrite arm spacing	79

5.4. Results of laboratory tests in ceramic mold - effect of pouring temperature on SDAS	84
5.5. Results of laboratory tests in ceramic crucible - effect of chemical composition on the solidification features	85
5.5.1. The effect of silicon and copper	86
5.5.2. The effect of titanium	95
5.5.3. The effect of zinc	104
5.5.4. The effect of magnesium	111
5.5.5. The effect of strontium	117
5.6. Comparative effect of different parameters	122
6. Conclusions	127
7. Literature	129
8. List of figures and tables	142
APPENDICES	146
NOMENCLATURE	148
LEBENS LAUF	151

1. Introduction

The importance of improved energy efficiency in recent decades reflects the effects of increased gasoline and oil costs to the consumer and graduated government-mandated fuel-efficiency standards for automobile and truck manufacturers. Environmental concerns, global competitiveness and raw material concerns reinforce the incentives to reduce fuel consumption while preserving product performance and cost objectives.

The most cost-effective means of addressing these challenges has been the submission of lightweight materials in existing and projected automotive design [1].

The use of cast aluminum alloys in automotive structural applications is growing rapidly because of the need to reduce weight. The service life of a cast component is determined by the microstructural distribution throughout the casting, especially in those regions that are critically stressed. For that reason it is of crucial importance to understand the phenomena that occur during the solidification of alloys as well the effect of different process parameters affecting the microstructure and consequently mechanical properties of the alloys. When Al-Si alloys are cooling down from the liquid state the initial formation of stable α -Al crystals generates a large enough constitutional undercooling effect that drives the dendrite formation over other morphologies that exhibit normal growth modes. Microstructural evolution then continues with the formation of primary dendrite arms, then secondary and tertiary dendrite arms. As dendrites grow in the liquid the rejected solute is displaced at the dendrite tips and by lateral diffusion in the spaces between adjacent dendrite arms. The concentration gradients in solute and solvent atoms between neighbouring dendrites drive the eventual dissolution of smaller dendrites while larger dendrites continually grow, leading to a gradual increase in measured secondary dendrite arm spacing (SDAS), the average spacing between the centres of adjacent dendrites. In hypoeutectic Al-Si alloy systems the enrichment of solute in interdendritic regions eventually drives Al-Si eutectic growth within the interdendritic regions. As solidification of dendrites and the Al-Si eutectic continues further solute enrichment (e.g. Si, Fe, Mn, Mg, Cu and Cr) drives more complex secondary phase constituent formation such as the β -Al₅FeSi, α -Al₈Fe₂Si, α -Al₁₂Fe₃Si₂, α -Al₁₅(Fe,Cr,Mn)₃Si₂, δ -Al₄FeSi₆, p-Al₈Mg₃FeSi₆, Q-Al₅Mg₈Cu₂Si₆, Al₂Cu and Mg₂Si.

Mechanical properties of Al-Si cast alloys depend on several microstructural parameters. Grain size, secondary dendrite arm spacing (SDAS), the shape, size and distribution of secondary phases or intermetallic compounds, the morphology of silicon particles (size, shape

and distribution) and finally, defects (porosity) play a key role in the behavior of aluminum alloys under static and dynamical loads. Basically, finer microstructure features (lower SDAS values) leads to the better mechanical properties.

Although the SDAS is not only factor affecting the mechanical properties of as-cast Al-Si-Cu alloys, SDAS determines the casting quality. Unlike the other microstructure features, SDAS correlates quite well with the tensile properties (ultimate tensile strength and elongation) as well as fatigue life time of casting components, i.d. lower SDAS higher ultimate tensile strength and elongation and longer fatigue life time. In addition to, it was shown that SDAS decrease leads to the reduction of porosity level (especially shrinkage porosity) and the quantity of detrimental intermetallic phases, Al_5FeSi (the phase is considered as one of stress concentration factors in aluminum alloy).

The majority of this study is focused on the SDAS in Al-Si-Cu hypoeutectic alloys and the parameters controlling the solidification behavior of Al-Si-Cu alloy.

2. Motivation and objectives

Because of the evident importance of SDAS, more and more automotive companies have defined so far a SDAS limit in their engineering specifications for aluminium castings (engine parts such as cylinder head and engine block). The automotive companies have defined the demands for SDAS in the area of combustion chamber surface which is the most thermally and mechanically stressed parts in cylinder heads. Generally, the requested value of SDAS depends on the model of cylinder heads (BMW, Porsche, VW, Fiat etc.). The value of SDAS ranges from 20 to 40 μm and that is measured at the distance of 3 – 5 mm from the combustion chamber surface. It is worth mentioning that, in some cylinder heads more rigorous demands must be met where SDAS at 4 mm from the combustion chamber surface must be less than 20 μm . On industrial production, the control of solidification rate (and therefore the SDAS values) is quite difficult to achieve, because of the complex casting geometry including the presence of many cavities and different wall thickness as well.

For that reason, reference castings are frequently employed when the solidification rate has to be accurately controlled and different microstructures have to be achieved. Therefore, in these castings, the solidification conditions can be set up by varying the thickness and the material of the mold, as well as the sample size. In this way, the factors affecting SDAS, the relationship between SDAS and mechanical properties of as-cast aluminum alloys can be easily better assessed and the information can be subsequently transferred to real-shaped casting.

Of the many phenomena that occur during the solidification of castings, there are four that control structure and consequently mechanical properties: chemical composition, liquid metal treatment, cooling rate and temperature gradient. Among them the cooling rate plays the most significant role. The effect of cooling rate on the structural features of aluminium alloys such as grain size, secondary dendrite arm spacing (SDAS), eutectic silicon structure and the morphology of iron and manganese phases has been investigated in the literature. However, the chemical composition of the alloys has also some effect on this structural characteristic.

The effect of chemical composition has become more important in the recent years since the majority of the permanent mold and die castings are produced from the secondary alloys.

The secondary alloys inherently contain a higher percentage of some alloying elements (Mg, Zn, Cu, Fe etc.), it becomes a heavy burden on the part of secondary smelters to remove the

excess of the alloying elements. Therefore, there has been an active campaign to change the allowable level of the alloying elements.

Unfortunately, effect of the chemical composition on solidification behaviour and SDAS value of Al-Si-Cu alloy have not been extensively investigated in the literature since this effect has not been easily recognized due to the leading effect of the cooling rate.

The purpose of this study was to evaluate the individual effect of varying alloying elements on the solidification behaviour and microstructure features such as SDAS of AlSi7Cu3 alloy. In order to assess the effect of alloying elements on the solidification behaviour of AlSi7Cu3 alloy, i.e. the liquidus temperature, dendrite coherency point (DCP), Al-Si precipitation temperature, Al-Cu precipitation temperature and T_{sol} as well SDAS value, the method of computer aided cooling curves supplemented by subsequent metallographic analysis have been used in present study. The Si, Cu and Ti contents have been ranged from 7-9 wt%, 1-4 wt%, 0.08-0.14 wt% respectively, according to the specification of the basic alloy. On the contrary, Mg and Zn contents were varied in the range of 0.2-3.0 wt% which was the common concentration range of these elements in the secondary alloys. The impact of solidification time on the SDAS value of AlSi7Cu3 alloy has been proven through the variation of mold temperature (250-350 °C) with and without the water cooling of the mold wall. The variation of the casting parameter such as pouring temperature (650-750°C) on SDAS of the basic alloy AlSi7Cu3 has been also examined in the present study.

3. Literature review

3.1. Aluminum and aluminum alloys

Aluminum alloys are characterized by their low relative density which can vary slightly above and below the density of pure aluminum depending on the major alloying elements. In addition to their light weight, other advantages of aluminum casting alloys include relatively low melting temperatures, negligible gas solubility with the exception of hydrogen, excellent castability especially near the eutectic composition of 11.7% related to Al-Si alloys, good machinability and surface finishing, good corrosion resistance and good electrical and thermal conductivity. A volumetric shrinkage of between 3.5% and 8.5% occurring during solidification constitutes the major drawback of aluminum castings. The shrinkage coefficient should be taken into account during mold design in order to obtain dimensional accuracy and to avoid hot tearing and shrinkage porosity.

Aluminum alloys constitute a group of cast materials which, in tonnage terms, is second only to ferrous castings. World-wide, approximately 20% of total aluminum production is, on average, converted into cast parts.

The physical and mechanical properties of aluminium castings may be altered through:

- ***Alloying composition:*** The composition of alloys determines the potential for achieving special physical and mechanical properties. Alloy content is designed to produce characteristics that include castability as well as desired performance capabilities. The interaction of alloying elements is recognized in promoting desired microstructural phases and solid-solution effects for the development of these properties. A wide range of metals can be added to aluminium [2]. Among those regularly added and controlled as alloying elements are zinc, magnesium, copper, silicon, iron, lithium, manganese, nickel, silver, tin and titanium. The solid solubilities of these elements in aluminum vary considerably (Table 3-1.). Some are used as solid solution strengtheners, while others are added because they form various desirable intermetallic compounds.
- ***Cooling rate during and after solidification:*** The conditions under which solidification takes place determine the structural features that affect the physical and mechanical properties of an alloy.

- **Casting process:** There are a large number of casting processes and each imposes different rates of heat extraction and solidification rates
- **Heat treatment:** Mechanical properties can be altered by post-solidification heat treatment, including annealing, solution process and precipitation aging.

Table 3-1 Solid solubility of elements in aluminum [2]

Element	Temperature, °C	Maximum solid solubility, wt %
Cadmium	649	0.4
Cobalt	657	<0.02
Copper	548	5.65
Chromium	661	0.77
Germanium	424	7.2
Iron	655	0.05
Lithium	600	4.2
Magnesium	450	17.4
Manganese	658	1.82
Nickel	640	0.04
Silicon	577	1.65
Silver	566	55.6
Tin	228	0.06
Titanium	665	1.3
Vanadium	661	0.4
Zinc	443	70.0
Zirconium	660.5	0.28

The selection of an alloy composition for a particular application is based on three parameters:

- castability (a complex property depending on feeding tendency, mold geometry and alloy solidification characteristics);
- mechanical properties and usage properties;
- costs.

3.1.1. Casting alloy designation

Specifications for casting alloys are clearly distinguished from those of wrought alloys and are defined by their chemical compositions [3].

Each country has developed its own aluminum casting alloy nomenclature and designation and so far no internationally accepted system has been adopted for identification. Alloy systems are classified by a number system (ANSI) or by names indicating their main alloying constituents (DIN and ISO). As a major step towards alignment of Aluminium and Aluminium Alloy compositions on an international basis, most countries have agreed to adopt the 4 digit classification for wrought alloy composition designation. The European reference for the alloys will be identified with the preface EN and AW which indicated European Normative and Aluminium Wrought alloys, respectively. In all other respects the alloy numbers and composition limits are identical to those registered by the Aluminium Association [1, 4].

Wrought aluminum is identified with a four digit number which identifies the alloying elements, followed by a dash, a letter identifying the type of heat treatment and 1 to 4 digit number identifying the specific temper (e.g. 6061-T6, the most common free-machining aluminum alloy). The Aluminum Association (AA) has adopted a nomenclature of cast aluminum alloys similar to that of wrought alloys. Cast aluminum alloys use a four to five digit number with a decimal point. The main alloying elements in the AA system are as in the Table 3-2 can be seen.

The meaning of the four designation digits are as following:

- First digit: Principal alloying element(s)
- Second and third digits: Specific alloy designation (number has no significance but is unique)
- Fourth digit: Casting (0) or ingot (1, 2) designation

In all casting alloy designations, this fourth digit, that to right of the decimal point indicates product form. In that case, 0 denotes castings; 1 denotes standard ingot and 2 denotes ingot having composition range narrower than but within those of standard ingot.

In designation of the 1xx.x type, the second and third digits indicate minimum aluminium content (99.00% or greater). For example, alloy 170.0 contains a minimum of 99.70% Al.

In 2xx.x through 8xx.x designations for aluminium alloys, the second and third digits have no numerical significance, but only arbitrarily identify individual alloys in the group.

Table 3-2 Classification of Casting Aluminum Alloys (Aluminum Association)

	AA	Major alloying elements	Atoms in solution	Precipitation hardening		
CASTING ALLOYS	1xx.x	Min 99% Al			Non-heat treatable alloys	
	4xx.x	Si	✓			
	EN AB	5xx.x	Mg (<7%)			
	EN AC	2xx.x	Cu			Heat treatable alloys
	EN AM	3xx.x	Si+Cu/Mg			
		7xx.x	Zn	✓	✓	
	8xx.x	Sn				
	9xx.x	miscellaneous				

*letters preceding the alloy numbers have the following meaning

EN = European Norm

A = Aluminium, B = Ingot, C = Cast Alloy, M = Master Alloy

The new European reference for alloys will be identified with the preface EN followed by a blank space followed by A which indicates aluminium then B,C, or M which indicate respectively ingots for re-melting, casting or master alloys.

Casting aluminium alloys based on those to which silicon is added as the main alloying element are probably the most important for engineering applications. This is because of the high fluidity provided by alloys with near eutectic composition. The castings have high corrosion resistance, combined with a low coefficient of thermal expansion and good weldability [5].

3.1.2. Aluminum-Silicon-Copper (3xx.x) system of alloys

Among the most widely used aluminium casting alloys are those that beside silicon (Si) contain copper (Cu) as well. The amounts of both additions vary widely, so that copper predominates in some alloys and silicon in other. Alloys containing higher hypoeutectic concentrations of silicon are normally better suited for more complex castings and for permanent mold and die casting processes.

Aluminum-silicon-copper alloys with less than 5.6 wt% Cu are heat treatable, but the more important alloys of this family are those also containing magnesium.

A small number of other elements are added to aluminium in order to modify its basic properties. The most important are iron, magnesium, manganese, silicon, titanium, chromium and zinc. These can be grouped into those with high solid solubility and those with low solid solubility (see Table 3-1).

Specifications for aluminium alloy chemical compositions include the effects of major, minor and impurities elements. Major alloying elements define the ranges of elements that control castability and property development. Minor alloying elements control solidification behavior, modify eutectic structure, refine primary phases, promote or suppress phase transformation and reduce oxidation. Impurity elements influence castability and the form of suitable phases that at times limit or promote desired properties.

Preferred major, minor and impurity element concentrations and relationships may not be defined by alloy specifications. Stoichiometric ratios for favoured phase formation can be specified, but also may not be controlled or defined. Concentration limits allow biasing of composition or castability and solidification property development. For maximum strength, the concentration of elements that form hardening phase can be maximized. Improved ductility results from finer structure restricting insoluble-elements concentrations and by controlling the concentrations of impurities in ratios that favour the formation of the least specified detrimental intermetallic constituents [5, 6].

Effect of alloying elements

Silicon

The outstanding effect of silicon in aluminium alloys is the improvement of casting characteristics. Additions of silicon dramatically improve fluidity, hot tear resistance and feeding characteristics. The most prominently used compositions in all aluminium casting processes are those which silicon plays a major role. Commercial alloys include the hypoeutectic and hyper eutectic ranges up to about 30% Si. Aluminium-silicon alloys are typically resistant to solidification cracking and display excellent castability and feeding characteristics.

Silicon combines with magnesium to form Mg_2Si in heat treatable alloys. It combines with iron and other elements to form complex insoluble phases. Silicon also reduces relative density and coefficient of thermal expansion.

Increasing silicon content improves fluidity for filling thin walls and for reproducing more intricate designs and details. The fraction of liquid in the solidification range is dictated by the initial composition and by the degree of non-equilibrium cooling. For higher-solidification rate processes such as pressure die and permanent mold casting and for thinner sections in which more rapid solidification takes place, shrinkage porosity is strongly affected by the temperature at which mass feeding from liquid to partially solidified structures no longer occurs (dendrite coherency point). Feeding to minimize shrinkage porosity improves as the volume fraction solid is increased at the temperature at which mass feeding ceases. For this reason, the most desirable silicon content of aluminium-silicon alloys corresponds to the characteristic process solidification rate.

Copper

The addition of copper to Al-Si alloys enables the formation of Al-Al₂Cu eutectic and/or Al₂Cu phases and other intermetallic compounds, which increase strength and machinability of casting parts. Copper also increases heat treatability of the alloy. On the other side, copper reduces resistance to general corrosion and in specific compositions and material conditions increases stress-corrosion susceptibility. Addition of copper decreases significantly the melting point of the alloy. Therefore, the copper increases the solidification range of the alloy reducing the hot tear resistance and increasing the potential for interdendritic shrinkage [6].

Magnesium

The addition of magnesium to aluminium-silicon alloys forms the basis for an extremely important and useful family of compositions that combines outstanding casting characteristics with excellent properties after heat treatment. Magnesium is the basis for strength and hardness development in heat treated aluminium-silicon alloys containing copper, nickel and other elements with the same purpose. The hardening-phase Mg₂Si displays a useful solubility limit corresponding to approximately 0.70 wt% Mg, beyond which either no further strengthening occurs or matrix softening takes place. Corrosion resistance is also excellent and a low level of thermal expansion is retained [7]

Titanium

Titanium is extensively used to refine the grain structure of aluminium casting alloys, often in combination with smaller amounts of boron. The operable phase is TiAl₃ with lattice spacing closely matched to that of aluminium. Titanium in excess of the stoichiometry of TiB₂ is

necessary for effective grain refinement. Titanium is often employed at concentrations greater than those required for grain refinement to reduce cracking tendencies in hot-short compositions [8, 9].

Strontium

Eutectic modification is a common process performed in Al-Si as-cast alloys primarily to improve mechanical properties, particularly elongation, by promoting a structural refinement of the inherently brittle eutectic silicon phase. It is well known that trace additions of strontium (a few hundred parts per million) to hypoeutectic Al-Si alloys result in a transformation of the eutectic silicon morphology from a coarse plate-like structure to a well-refined fibrous structure. Lower concentrations are effective with higher solidification rates. Higher additional levels might be associated with casting porosity. Strontium has been regarded as ineffective as a modifier at slow solidification rates, but some investigators report beneficial effects in 319.0 and 356.0 alloys when >200ppm Sr is present [10, 11].

Zinc

Behaviour of zinc in aluminium casting is not completely examined. Accompanied by the addition of copper and/or magnesium, however, zinc results in attractive heat treatable or naturally aging compositions. A number of such compositions are in common use. Zinc is also commonly found in secondary alloys and die casting compositions. In these alloys, tolerance for up to 3% Zn allows the use of lower-grade alloy scrap.

3.1.3. Casting of aluminum alloys

Foundry alloys are obtained either from electrolytic aluminum to which are added the constituent elements or from recycled aluminum metal. Presently it is estimated that more than 50% of aluminum cast parts are made from recycled metal [12, 13].

Today, there are a large number of industrial casting processes which hierarchical classification is presented in Fig 3-1. These can be classified based on the mold material, method of producing the mold and the pressure on molten metal during filling (gravity, centrifugal force, vacuum, low pressure, high pressure). Permanent or metal molds are used in gravity and pressure die casting processes, suitable for producing a large number of components.

In general, aluminum castings can be produced by more than one process. Quality requirements, technical limitations and economic considerations dictate the choice of a casting process.

The three main casting processes for production of aluminium castings are as follows:

- sand casting: large castings (up to several tons), produced in quantities of from one to several thousand castings;
- permanent mold casting (gravity and low pressure): medium size castings (up to 100 kg); in quantities of from 1000 to 100,000;
- high pressure die casting: small castings (up to 50 kg); in large quantities (10.000 to 100.000).

These castings and production sizes are typical, but of course exceptions are always possible. Other casting processes include: investment casting (lost wax), lost foam casting, plaster molding, ceramic molding, centrifugal casting and new and emerging processes such as squeeze casting and semi-solid casting [1, 3, 14].

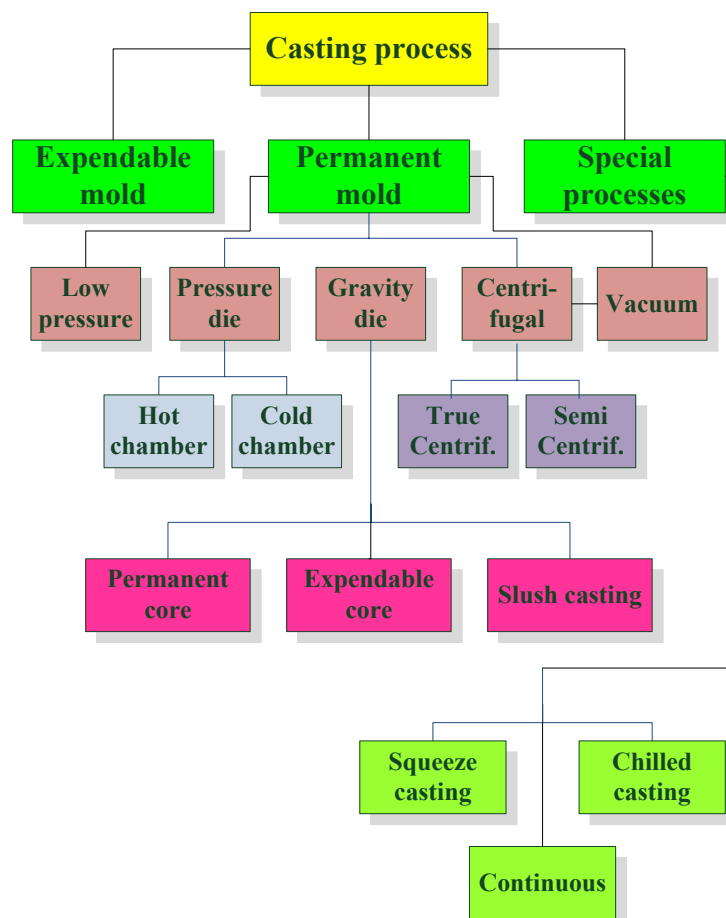


Fig. 3-1 Hierarchical classification of various casting processes [14]

Aluminium castings are very powerful and versatile techniques for manufacturing semi- or finished products with intricate shapes. Those techniques are continuously improved and developed to satisfy the user needs and to penetrate new markets. Innovations are mainly oriented to the automobile sector which is the most important market for castings. This continual improvement and development will ensure that aluminium castings continue to play a vital role in this field.

3.2. Cylinder head

3.2.1. Casting processes for production of aluminium cylinder heads

According to known practice, cylinder heads are manufactured mostly by casting. The casting technologies can be classified based on the following criteria:

- 1) various acting force on the metal flow during filling the mold,
- 2) the mold material and
- 3) the gating system.

Usually, casting molds are used whose outer margins are formed by casting dies, made of steel for example. To form inlet and outlet channels as well as a space for the cooling water in the cylinder heads (so-called water chamber), sand cores are suspended in the casting dies. Gravity casting is nowadays very well established in foundry industries for production of aluminium cylinder heads. Gravity casting occurs without any outside influences, apart from gravity itself using sand mold, permanent mold or lost foam shell. One of the key factors that significantly influences the quality of cast products is a design of a gating system. The gating system refers to those channels through which the metal flows from the ladle to the mold cavity. The use of a good gating system is even more important if the casting is produced by a gravity process. If the poor gating techniques are used, lower casting quality is achieved, due to a turbulent flow of the melt through the gating system [15]. There are three types of conventional mold processes for the casting of cylinder heads which are distinguished by the

position of gating system. All of them are schematic presented in Fig. 3-2. The top casting method ensures the directional solidification process as well as better cooling of the combustion chamber area which leads to improved mechanical properties of cast parts. The most complex and the most difficult task by gravity top casting method is related to the defects directly caused by turbulence. It is certainly difficult to influence the free-fall of the melt. Comparing the top to the bottom gating system, the advantage of the bottom casting method is laminar flow of the molten metal into the mold. On the other side, the limitations of bottom casting represent the cooling conditions in combustion chamber leading to the negative influence on the mechanical properties. The presence of shrinkage and gas pores in cast structure are to be expected because the lack of directional solidification.

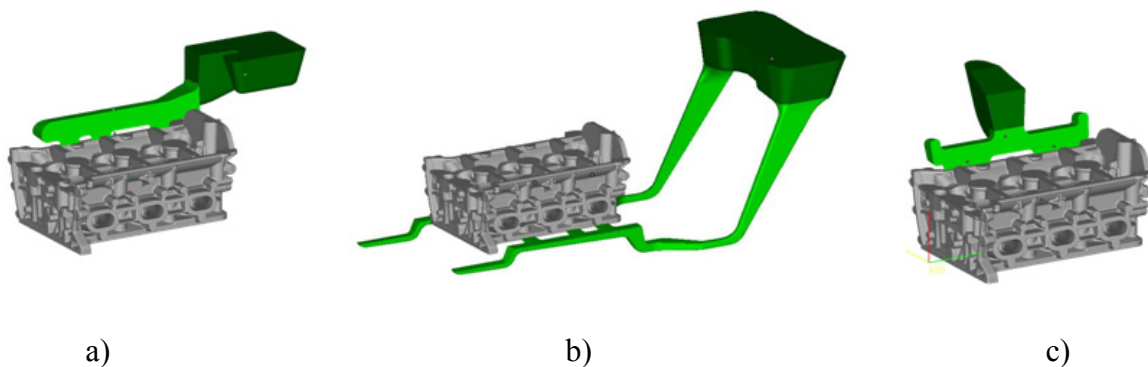


Fig. 3-2 Example of cylinder heads with gating system poured by gravity a) top casting b) bottom casting and c) tilt casting [15]

Taking into consideration the tilt pouring casting method it can be underlined that this method posses all advantages present by the top casting but at the same time reduces the turbulent flow of the melt due to the tilting of the whole system during filling process.

In the production of the cylinder head by gravity casting process the quality of casting is strongly influenced by filling conditions of gating system and mold cavity. Particularly the pouring process of light metals is very dynamic and complex [16-18]. The flow velocities in some gating areas are very high. The inadequate gating system or speeding of the metal stream can cause the turbulent flow of metal that initiates the formation of oxides as well mold erosion. On the other side, slow metal flow and fast solidification are reason for cold shots.

The production praxis of cylinder heads by gravity casting process showed that the quality of the cast products is related to the filling pattern of the gating system and the filling pattern of the mold. Of course, other important factors that affect the quality of cast products such as the melt temperature, the mold temperature, filling time and alloy have to be considered.

3.2.2. Function of car engine cylinder heads

The cylinder head is a key to the performance of the internal combustion engine, as the shape of the combustion chamber, inlet passages and ports determines a major portion of the volumetric efficiency and compression ratio of the engine [19]. In an internal combustion engine, the cylinder head sits above the cylinders and consists of a platform containing part of the combustion chamber and the location of the valves and spark plugs. In Fig. 3-3 it can be seen an example of car engine including its parts (left side) and the appropriate cylinder head (right side) [20].

The cylinder head is connected to the top of the engine block and allows air/fuel mixture and exhaust into and out of the cylinder block. The cylinder head has the duty of holding the air/fuel mixture charge inside the cylinder as it combusts, forcing the piston downward. The cylinder head is connected to the engine block using head bolts, using a head gasket to seal both parts.

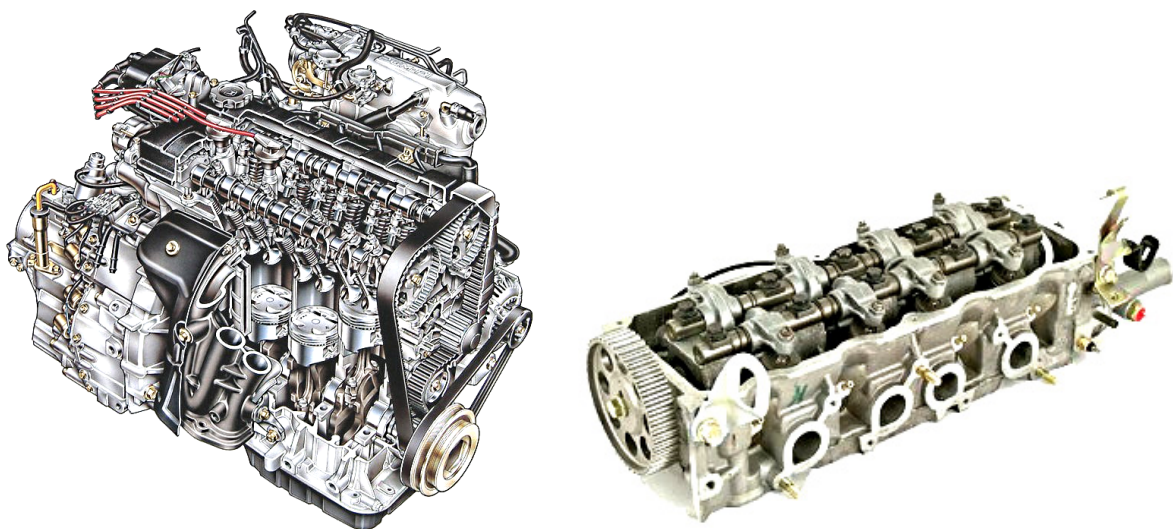


Fig. 3-3 Example of engine and appropriate cylinder head [20]

Coaxial with the valve seatings are the valve guides, which are carried in bosses of the cylinder head. Their length must be such as to present an adequate bearing surface to resist any side loading on the valve stems and also to provide a ready path of heat transfer from the exhaust valve head. The valve may seat either directly in the material of the cylinder head or, in harder-wearing rings, inserted therein. Valve seat inserts are usually confined to engines where the cylinder head material is aluminium alloy.

In recent years the main driving force for the evolution of automotive engines have come from legislation (exhaust emissions, fuel consumption) and from end user expectations (increased output, better driveability and comfort). The results of this development process have been the setting of clear trends in terms of:

- weight reduction, due to wider application of light materials;
- increased power density and tendency to downsizing of the engines; future expected values are up to 65 kW/l for Direct Injection Diesel Engines and up to 75 kW/l for boosted Gasoline Direct Injection engines;
- introduction of advanced combustion systems for both Spark (SI) and Compression (CI) Ignition engines.

As a consequence of the above described engine development trends, specifications required to aluminum cylinder head castings are becoming more and more severe, due to:

- high power density, resulting in higher operating temperatures;
- increased combustion pressures, meaning higher mechanical stresses (static and dynamic) on the material that combined with thermal cycles may cause significant reduction in fatigue life of the component;
- multi ports layouts and application of advanced combustion systems, leading to very complex geometries and thin cooling water passages.

In next generation engines combustion pressure is expected to rise to 180-200 bar range for CI engines and to 100-120 bar range for boosted SI engines, while maximum combustion chamber wall temperatures, usually found at the bridge between exhaust valves, might rise well over 250°C and approach 300°C. These new requirements have pushed the casting supplier to develop new process solutions with the aim of increasing the quality of castings, minimizing defects (porosity, inclusions etc.) and improving the microstructure of the material (dendritic arm spacing), in order to achieve better mechanical properties [19, 20].

3.2.3. Materials selection for car engine cylinder heads

The global environmental and traffic concerns, identified as a negative inheritance of the last century, should be addressed in this century to minimize the future impact of the expanding vehicle population. Among the global concerns, the reduction of CO₂ and other auto emissions is an especially important challenge. The development of new systems and technologies are, of course, being carried out to tackle these issues. At the same time, vehicle weight has shown a trend of increasing recently, due, in a part, to the addition of equipment that increases safety and comfort. Unfortunately, increased vehicle weight has a negative impact on lowering emissions. Considering this background, successfully vehicle weight reduction has been identified as one of the most important needs to meeting future automotive goals. To this end, the application of aluminium, the lightest practical metal, is so attractive for weight reduction that there are now many researchers working on the development of aluminium alloys for automotive [21-24].

To fulfil the rising requirements of the cylinder head without new material inventions the existing capabilities must be improved. Therefore two possibilities exist:

- Optimisation of the existing (aluminum alloys) material (fine tuning of chemical composition)
- Alternative casting method and the construction principles

To optimise the cast materials it is important to improve the quality of the microstructure in order to achieve a lower porosity and a higher ductility. Precipitation hardening and reinforced particle systems are possible for an improvement [25].

Alternative construction principles as changing the valve seat geometry, optimising the water circulation or changing the valve diamond geometry can reduce the material loading [26].

A further option is to split cylinder heads. That allows to produce two parts with two similar/or different materials.

In order to meet automotive legislation requiring low-exhaust emission, reducing part weight and cost as well as improving performance, it might be said that the heat treatable Al-Si-X alloys are still developed (X=Cu, Mg and Zn) [27, 28]. Use of aluminium in engine components has the advantage of a material with a higher thermal conductivity than cast iron, which allows for higher working temperatures in the combustion chamber and contributes to increase the power rating of the engine while requiring lower amounts of refrigeration liquids

[29, 30]. Changing from iron to aluminium has not been an easy task for industry, as it is required for aluminium parts to withstand more stringent conditions than those to which iron castings are subjected, which are promoted by the higher working temperatures of the engine that may enhance the reduction in strength of the material at the time that increases the possibility of promoting thermal fatigue [27, 31].

Aluminium-Silicon-Copper alloys such as 308.0, 319.0, 360.0, 380.0 and 384.0 offer good casting characteristics, higher strength and hardness and improved machinability with reduced ductility and lower resistance to corrosion. These and similar general purpose alloys are often produced in the as-cast condition and the typical application of these alloys is related to *cylinder heads*.

Aluminium-Silicon-Magnesium alloys including 356.0 and A356.0 have excellent casting characteristics and resistance to corrosion. Heat treatment provides combinations of tensile and physical properties that make them attractive for many applications, among them *cylinder heads*.

The well-known advantages associated to the use of aluminium alloys (light weight, good mechanical behaviour, good corrosion resistance, etc.) constitute the driving force for the introduction, on one hand, of new applications and design and, on the other hand, for the development of new processing solutions. Especially, dramatic improvement in tensile and fatigue strengths at elevated temperatures are demanded for engine parts, such as cylinder heads, engine blocks, which are the thermally and mechanically stressed parts. The inhomogeneous and time-dependent temperature fields during start–stop processes in engine result in thermally induced fatigue loadings with low frequency and, especially in the “hot” regions of the components (for example combustion chamber surface of cylinder heads), large plastic strain amplitudes. On the other hand, the combustion pressure and oscillating masses result in a mechanical fatigue loading with distinctly higher frequencies and smaller strain amplitudes than the thermal fatigue cycles [3, 16, 32, 33].

3.2.4. Requested metallurgical and mechanical characteristics of car engine cylinder head

The mechanical properties of cast aluminum alloys are largely dependent upon the solidification microstructure of the alloys. The service life of a cast component is determined by the microstructural distribution throughout the casting, especially in those regions that are critically stressed. In the drive toward lightweight vehicle production, the description and prediction of the microstructure in shape castings has become important. This is because the

microstructure length scales are required in the mechanical property models used for design optimization. The use of predictive property models is critical due to the need to replace heavy ferrous parts with aluminum alloy castings and the limited experience with the use and long term performance of aluminum alloy castings [34-36].

Secondary dendrite arm spacing (SDAS), which is defined as the distance between the protruding adjacent secondary arms of a dendrite, has been used in recent years to describe the metallurgical structure of cast materials. Castings having a finer microstructure show better static and fatigue properties and, particularly for cast aluminium alloys, this improvement is related to a lower SDAS value [37, 38].

Generally, most mechanical and structural components are subjected to various ranges of temperature variation in service conditions. Thus, the thermal gradients induced in these parts result in internal stresses and strains and these thermal cycles originate the process of low-cycle fatigue [39], which initiates with the process of crack nucleation and propagation.

Automotive part, such as cylinder head, is an example of parts submitted to thermal cycles and, therefore, to thermo-mechanical fatigue (TMF) process. In such component, fatigue fractures occur due to starting-shutdown cycles, which involve temperature changes up to 300 °C. The aluminum alloys used for this application present mechanical behavior that involves plasticity in low temperature and large viscoplasticity at high temperatures. These alloys are also subjected to aging process, especially at temperatures above 150 °C, [40] so different strain mechanisms are acting during the thermomechanical cycling applied to the material, making the understanding of the whole fatigue process very complex.

The efforts will be done to improve the performance of these materials by controlling the microstructure features, for example, in the cooling rate, aiming at reducing the secondary dendrite arms spacings and porosity [41, 42, 43, 44].

Speaking about the fatigue life time of cylinder head, in reference [45] it was emphasized that the pore size is the key factor controlling fatigue lifetime in E319 cast aluminum alloys. However, the distribution of pore size and other microstructural features causes great variability in fatigue lifetime. Therefore, SDAS influences fatigue lifetime by controlling the size and distribution of the porosity as it was reported by the authors of this work.

V. Firouz et. al have the same opinion that thermal fatigue life can be improved effectively by decreasing of SDAS, porosity volume fraction and coarse intermetallic contents. They found that fracture surface of the fine SDAS samples showed more traces of plastic deformation, whilst fracture surface of large SDAS ones showed even cleavage fracture [46].

On the other side, there are also authors who believe that the positive effect of low SDAS values is intensified at low cycles, while porosity (and particularly its size) plays a key-role at high cycles [47]. A small SDAS also reduces the time required for homogenisation heat treatments since the diffusion distances are shorter.

Because of the evident importance of SDAS, more and more automotive companies have defined so far a SDAS limit in their engineering specifications, particularly for SDAS in the area of combustion chamber surface which is the most thermally and mechanically stressed parts in cylinder heads. Generally, the requested values of SDAS vary from model to the model of cylinder heads (BMW, Porsche, VW, Fiat etc.). The value of SDAS ranges from 20 to 40 μm and that is measured at the distance of 3 – 5 mm from the combustion chamber surface. It is worth mentioning that, in some cylinder heads more rigorous demands must be met where SDAS at 4 mm from the combustion chamber surface must be less than 20 μm , as it is illustrated in Fig. 3-4 [38]. On industrial production, the control of solidification rate (and therefore the SDAS values) is quite difficult to achieve, because of the complex casting geometry including the presence of many cavities and different wall thickness as well.

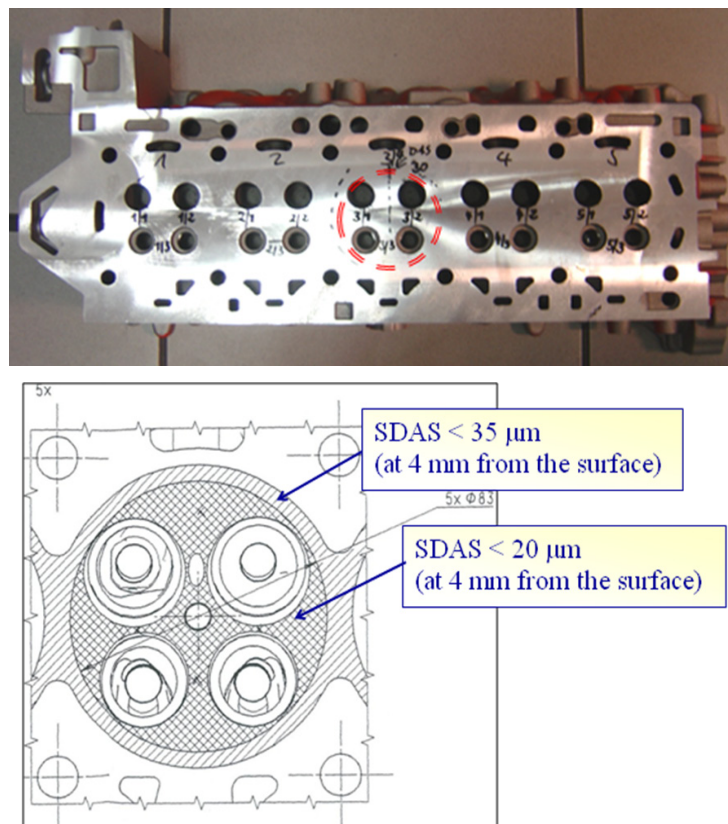


Fig. 3-4 Car engine cylinder head and demands on SDAS in outer and inner part of cylinder in combustion chamber area [38]

3.3 Solidification process of aluminum and aluminum alloys

The solidification of cast aluminum alloys starts with separation of a primary α aluminum-phase from the liquid. After nucleation, when the temperature lowers, the primary phase grows as solid crystals having dendritic shape. When the eutectic temperature has been reached, the solidification proceeds at constant temperature with the formation of the eutectic solid phase in the space left between dendritic arms.

The dendritic microstructure of as-cast state of alloys is a direct effect of the material solidifying under given conditions. It is well known that dendritic microstructure shows significant sensitivity on global casting parameters, e.g. temperature and cooling rate. On the other side, the effect of more localised parameters such as concentration gradient in different zones of casting must be taken into account. Geometry of dendrites, being sensitive to mass and heat transfer conditions and their evolution over duration of casting process, can be considered as a result of how these parameters change in situ. This information can be valuable tool for process control and optimisation.

In literature survey there is a number of different theoretical and experimental models to treat dendritic growth. These models permit the correlation of microstructural features with solidification process parameters.

Two important quantitative microstructural parameters, the primary dendrite arm spacing, λ_1 (DAS) and the secondary dendrite arm spacing, λ_2 (SDAS) can be related to the thermal field derived parameters as it is expressed by the following equations [48, 53, 106]:

$$\lambda_1 = \text{DAS} = A G_L^a R^b \quad (3-1)$$

$$\lambda_2 = \text{SDAS} = C t_f^n \quad (3-2)$$

where G_L is the thermal gradient in the liquid in front of dendrites, R is the solid-liquid interface velocity, t_f is the solidification time (which can be evaluated as the ratio between the liquidus-solidus temperature interval and the cooling rate during solidification), A , a , b , C and n are constants (related to the alloys). Exponent n is in the range of 1/3 to 1/2 for secondary dendrite arm spacing in aluminium alloys.

According to Grugel [48], although the primary dendrite spacing is constant during a steady-state solidification process, the secondary dendrite spacing modifies notably along the

primary arms. Such a behavior can be explained on the basis of a coarsening process of the dendrite branches during the solidification. Several researchers, including Whisler and Kattamis [49] and Feurer [50] have analyzed the coarsening phenomenon in dendritic growth. One of the most effective models to deal with a correlation between secondary dendritic arm spacing and solidification parameters was proposed by Feurer [50]. For secondary arm spacing, Feurer developed a theoretical model that relates SDAS, to the local solidification time, t_f . The Feurer model was developed, based on the work of Kattamis et al. [49]. According to Feurer [50], SDAS is a function of the local solidification time, t_f , and is given by the equation:

$$\text{SDAS} = 5.5(Mt_f)^{1/3} \quad (3-3)$$

where M is defined as coarsening parameter and value of M is usually in the range of 1-10 for aluminum alloys and the exponent value is in the range of 1/3 to 1/2 for aluminum alloys.

The secondary dendrite arm spacing (SDAS) is determined by solidification time through the mushy zone, with longer solidification time resulting in larger values of SDAS.

The size of the dendrites is affected not only by heat transfer rate during solidification of the casting into mold but also the chemical composition of the alloy. The effect of major and minor alloying elements on the solidification behaviour and the microstructure feature, SDAS of Al-Si-Cu alloy has been extensively studied in this work.

3.3.1. Nucleation and growth of α -Al phase

The concept of solidification comprises two basic phenomena: nucleation and growth of crystals from the melt. By lowering the temperature of a metal melt below the equilibrium liquidus temperature, solid becomes the thermodynamically stable form of matter and a transformation from liquid to solid starts. The rate of this process depends primarily on the rate of heat extraction from the system and the driving force, free energy (ΔG) for nucleation, as well as growth of crystals, is a function of the degree of undercooling (ΔT) which is created during the solidification process relative to the equilibrium conditions. The primary process determines the size and morphology of crystals formed from a melt, and it is important, therefore, to control the early stages of the solidification process. Many of final properties of

the castings are determined by the conditions under which the primary crystals are nucleated and started to grow [51, 52].

The solidification process involves extraction of heat from the melt in a more or less controlled manner. Heat extraction changes the energy of the phases (solid and liquid) in two ways:

- 1- There is a decrease in the enthalpy of the liquid or solid, due to cooling,
- 2- There is a decrease in enthalpy, due to the transformation from liquid to solid, which is equal to the latent heat of fusion, ΔH_f : defined to be negative for the liquid-to-solid transformation (exothermic reaction).

Heat extraction is achieved by applying a suitable means of cooling to the melt in order to create an external heat flux, q_e . The resultant cooling rate, dT/dt can be deduced from a simple heat balance if the metal is isothermal (low cooling rate) and the specific heats of the liquid and the solid are the same. Using the latent heat per unit volume $\Delta h_f = \Delta H_f/v_m$, in order to confirm the dimensions of the other factors, then

$$q_e \left(\frac{A'}{V} \right) = -c \left(\frac{dT}{dt} \right) - \Delta h_f \left(\frac{dfs}{dt} \right) \quad (3-4)$$

so that:

$$\dot{T} = \frac{dT}{dt} = -q_e \left(\frac{A'}{V \cdot c} \right) - \left(\frac{dfs}{dt} \right) \left(\frac{\Delta h_f}{c} \right) \quad (3-5)$$

The first term on the right-hand-side of equation (3-5) reflects the effect of casting geometry (ratio of surface area of the casting, A' , to its volume, V) upon the extraction of sensible heat, while the second term takes account of the continuing evolution of latent heat of fusion during solidification. It can be seen from this equation that, during solidification, heating will occur if the second term on the right-hand-side of equation (3-5) becomes greater than the first one. This phenomenon is known as recalescence [51, 53].

For an alloy, where solidification occurs over a range of temperatures, the variation of the fraction of solid as a function of time must be calculated from the relationships (3-6):

$$\frac{df_s}{dt} = \left(\frac{dT}{dt} \right) \left(\frac{df_s}{dT} \right) \quad (3-6)$$

since f_s is a function of temperature. In this case:

$$\dot{T} = \frac{-q_e \left(\frac{A'}{V \cdot c} \right)}{1 + \left(\frac{\Delta h_f}{c} \right) \left(\frac{df_s}{dT} \right)} \quad (3-7)$$

It is seen that solidification decreases the cooling rate since both df_s/dT and Δh_f are negative.

The transformation of one phase into another requires rearrangement of the atoms. This may involve a relatively short-range (atomic) rearrangement to form a new crystal structure, as in the case of pure substance. Alternatively, atomic movement may be required over much larger, but still microscopic distances as in the case of alloy solidification where mass diffusion controls the transformation.

Solidification, as a phase transformation is driven by thermal fluctuations and can only occur when the probability of transfer of atoms from the parent phase to the product phase is higher than that for the opposite direction. Therefore, stable regions of the new phase have to form. In solid metals, random fluctuations may create minute crystalline regions (clusters, embryos) even at temperatures greater than the melting point, but these will not be stable. Indeed, they continue to be unstable to some temperature below the melting point because the relatively large excess energy required for surface creation tends to weight the 'energy balance' against their survival when they are small. Once nucleation has occurred, atom transfer to the crystals has to continue in order to ensure their growth. Although thermodynamics says that below the melting point the solid state is the stable state of the material, the appearance of the solid state needs additional energy, which is provided by undercooling below the equilibrium melting temperature. The larger the undercooling the more energy is contained in the undercooled melt. At a certain undercooling, nuclei of the solid phase can form inside the melt (homogeneous nucleation), but mostly they will appear at mold walls (heterogeneous nucleation), since the energy to form them there or at foreign particles inside the melt is smaller.

Once a nucleus is formed, it will continue to grow. Such growth will be limited by:

- the kinetics of atom attachment to the interface,
- capillarity,
- diffusion of heat and mass.

The growth rate of a crystal depends upon the net difference between the rates of attachment and detachment of atoms at the interface. The rate of attachment depends upon the rate of diffusion in the liquid, while the rate of detachment depends on the number of nearest neighbours binding the atom to the interface. In general, reorientation of a complicated molecule in the melt, surface diffusion and other steps may be required. An atomically flat interface will maximise the bonding between atoms in the crystal and those in the interface. Thus, such an interface will expose few bonds to atoms arriving via diffusion through the liquid. Such a crystal has a tendency to close up any gap in its solid-liquid interface at the atomic scale. This leads to crystals which are faceted at the microscopic scale and usually exhibit high undercooling. An atomically rough interface always exposes a lot of favourable sites for the attachment of atoms from the liquid. Such an interface tends to remain rough and leads to smooth crystals which are non-faceted at the microscopic scale and exhibit low kinetic undercooling [51, 53].

3.3.2. Morphological instability of solid-liquid interface – constitutional undercooling

To explain the idea of “constitutional undercooling”, a binary alloy that solidifies at a constant velocity is considered (see Fig.3-6). The concept of constitutional undercooling only states when the solid-liquid front becomes unstable; it does not predict the most stable growth mode, its shape, etc. This problem was solved by Mullins and Sekerka [54], who introduced another important aspect: the curvature of a perturbation. The melting point of a planar front differs from that of a curved interface. Convex interfaces have a lower melting point than concave shaped ones. This means, if a perturbation is highly curved, it melts back easier than would a shallow curved interface. A perturbation induces a perturbed solute or thermal field and either heat or solute (or both) have to be transported away from the tips by diffusion. The longer the wavelength of the perturbation the larger the diffusion distance to equilibrate the concentration profile. Diffusion of heat or solute would prefer a sharply curved interface. The competition between transport and curvature determines the wavelength that is selected.

The concentration profile can be converted into a virtual temperature profile indicating a position ahead of the interface where the concentration there would be in equilibrium. The difference between the real temperature and the virtual, equilibrium phase diagram temperature defines a region in which two conditions can prevail: the real temperature always is much larger than the virtual temperature or vice versa. The first case means whenever a perturbation grows in advance of the interface, it sees a region which is hotter and thus melts

back. If the virtual temperature is larger than the real one, a perturbation sees a region which is in reality colder and thus it can grow.

At a given temperature gradient a low solidification velocity will yield a planar interface, which becomes cellular at higher velocities. These cells become unstable and develop into dendrites. At even larger velocities a planar solidification front can be achieved again.

Three limiting cases will be considered in the following paragraphs.

The first of these is **equilibrium solidification** (Figure 3-5) and the movement of a planar solidification front along a bar of liquid metal which contains a solute with an initial concentration of C_0 . This type of solidification can be achieved in practice by using a special furnace to impose a steep temperature gradient on a crucible holding the metal.

This assumes that total mixing takes place in both the liquid and the solid. This requires complete diffusion to take place in the solid, which is usually impossible. When liquid metal starts to solidify at a particular temperature, a certain volume fraction of solid has formed, f_s , leaving a certain volume fraction of liquid, f_L , where $f_s + f_L = 1$.

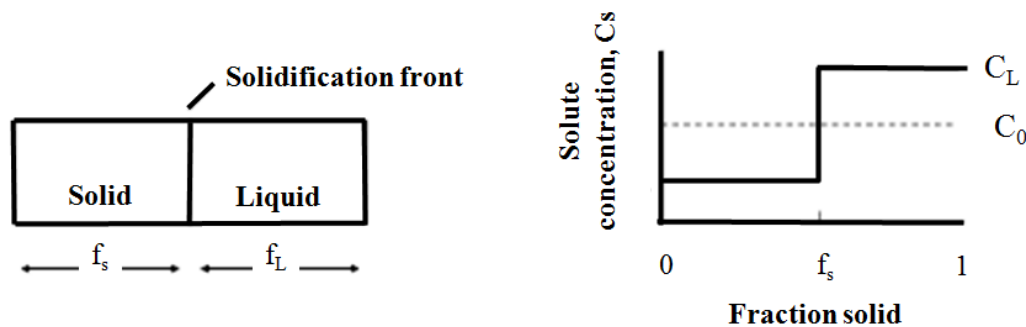


Fig. 3-5 Solidification under equilibrium conditions [32]

The law of the conservation of mass requires that:

(Solute in solid) + (Solute in liquid) = (total solute) or

$$C_s f_s + C_L f_L = C_0 \quad (3-8)$$

where C_s and C_L are the concentrations of the solute in the solid and liquid respectively.

The above equation can be shown to be merely a re-statement of the **lever rule** by substituting for $f_L = 1 - f_S$ Equation (3-8) then becomes:

$$f_S = \frac{C_0 - C_L}{C_S - C_L} = \frac{L_1}{L_2} \quad (3-9)$$

As it is shown in Fig. 3-6, the molten alloy is cooled down having an initial solute concentration of C_0 , a liquidus temperature of T_L and a solidus temperature of T_S . At a temperature T where the fraction solid is f_S , $L_1 = C_0 - C_L$ and $L_2 = C_S - C_L$ and substitution of these values in equation (3-9) gives actually the equilibrium lever rule (see Fig. 3-6).

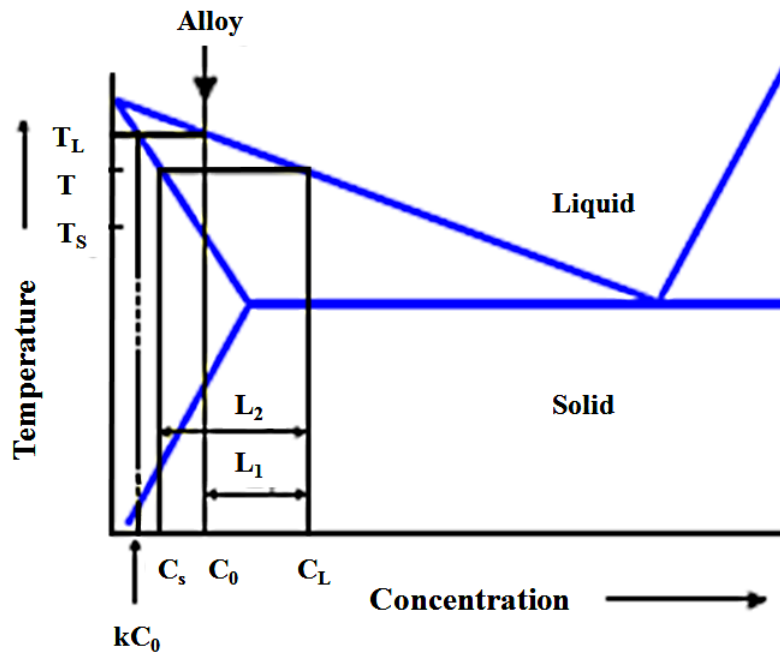


Fig. 3-6 Binary Phase Diagram and equilibrium solidification

The second case considers **the non-equilibrium solidification** that derives the Scheil's equation that is widely used to describe the solidification behaviour. The top part of Fig. 3-7 left again shows the progression of solidification with a front between solid and liquid moving from left to right. The bottom half shows solute concentration as a function of the fraction solid.

The initial uniform solute concentration in the liquid is C_0 . The first solid to form has a composition of $k \cdot C_0$, where k is the partition coefficient between the solid and liquid phases,

i.e. $k = C_S / C_L$. When the initial solid is formed, the excess solute is rejected ahead of the advancing front. Based on the Scheil's rule the following assumptions are made:

1. There is efficient mixing in the liquid so that there is a uniform solute distribution, giving a uniform concentration C_L ;
2. There is no diffusion of solute in the solid phase, which can arise if the rate of cooling is high or if the rate of diffusion is low. This is usually quite a good approximation for most substitutional solutes, such as Mn in Fe, or Cu in Al.

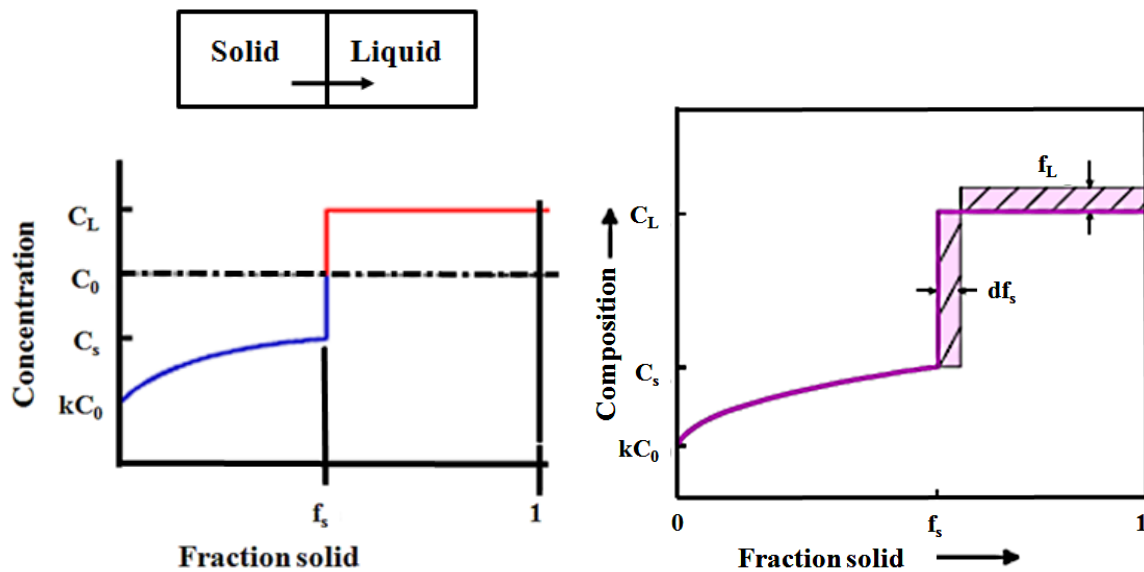


Fig. 3-7 Solidification under non-equilibrium condition

As the solid-liquid interface advances by a small amount df_s with the rejected solute, then the solute concentration in the liquid increases by dC_L . By the definition $k = dC_S / dC_L$ hence the shaded areas in Fig. 3-7 right can be defined by **Scheil's equation** or so called **non-equilibrium lever rule**:

$$C_S = kC_0(1 - f_s)^{k-1} \quad (3-10)$$

It applies with reasonable accuracy to all substitutional solutes, such as Cu, Zn and Mg in Al and Cu, Cr and Mn in Fe.

The third model or so called **solute rejection model** assumes that perfect mixing occurs in the liquid and there is no diffusion in the solid. As solute is rejected ahead of the advancing front,

it diffuses away in the liquid to give a steady-state profile. Under these conditions, the solute rejected into the liquid builds up to a peak concentration of C_0/k ahead of the moving front, as it is seen in Fig. 3-8.

In order to determine the stability of growth front, the actual temperature gradient, G , applied to the liquid has to be considered. When G is high, the temperature of the liquid ahead of the solidification front (T) is always above the melting point (T_L). This leads to conditions for stable planar growth, i.e. there is no constitutional undercooling. However, if the temperature gradient is lower, the liquid ahead of the front is effectively undercooled below its freezing point (Fig. 3-8). This unstable condition leads to cellular or even dendritic growth. Thus the condition for stable growth can be defined as the following:

$$G \geq \frac{T_L - T_S}{d} \quad (3-11)$$

Substituting for the thickness of solute layer, d with $d=D/R$, (D - coefficient of diffusion of the solute in the liquid, R -the rate of the solidification front) gives

$$\frac{G}{R} \geq \frac{T_L - T_S}{D} \quad (3-12)$$

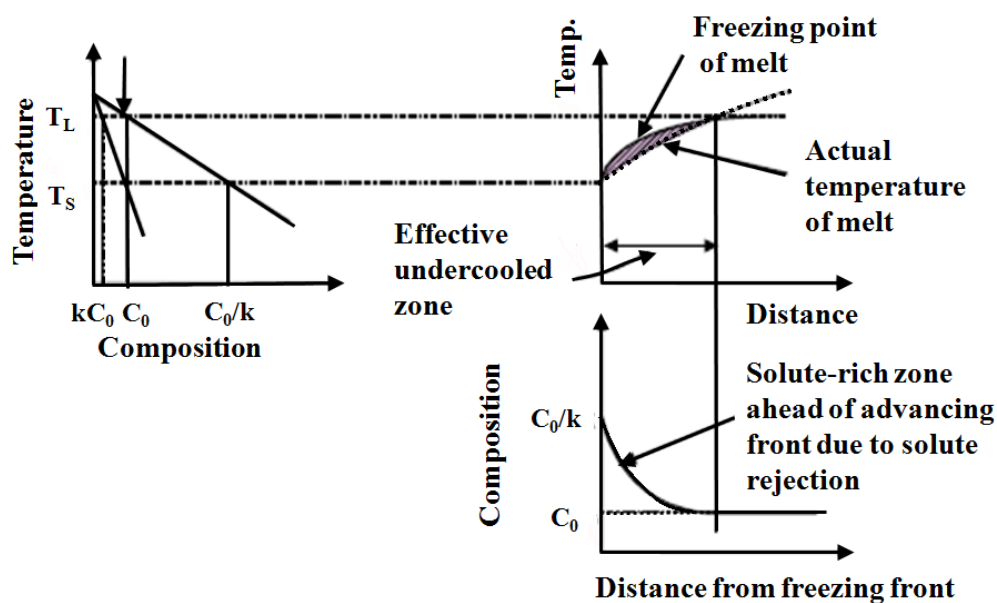


Fig. 3-8 Link between the Constitutional Phase Diagram and Constitutional Undercooling [32]

This is the condition which roughly defines that there is no constitutional undercooling ahead of the interface which therefore remains stable and flat. If the equality is reversed, then the liquid ahead of the solidification front is effectively undercooled below its freezing point causing the unstable situation which leads to cellular or dendritic growth. This instability arises because any slight perturbation of the growing front causes the front to move into a region of higher effective undercooling, so growth is accelerated. This is of course a run-away situation, leading to the disintegration of the planar front into a series of long, finger-like growth forms such as cells or, more extremely, as dendrites [38].

Fig. 3-9 shows how the growth morphology changes from planar to cellular and then to dendritic as the compositionally-induced undercooling increases. Although metals and alloys can solidify in any of these modes, the most common form in real castings is dendritic solidification. A dendrite can be defined as the basic tree-like growth form of the solidification front which occurs when instability predicted by the constitutional undercooling condition is high.

When regular cells, form and grow at relatively low rates, they grow perpendicular to the liquid-solid interface regardless of crystal orientation.

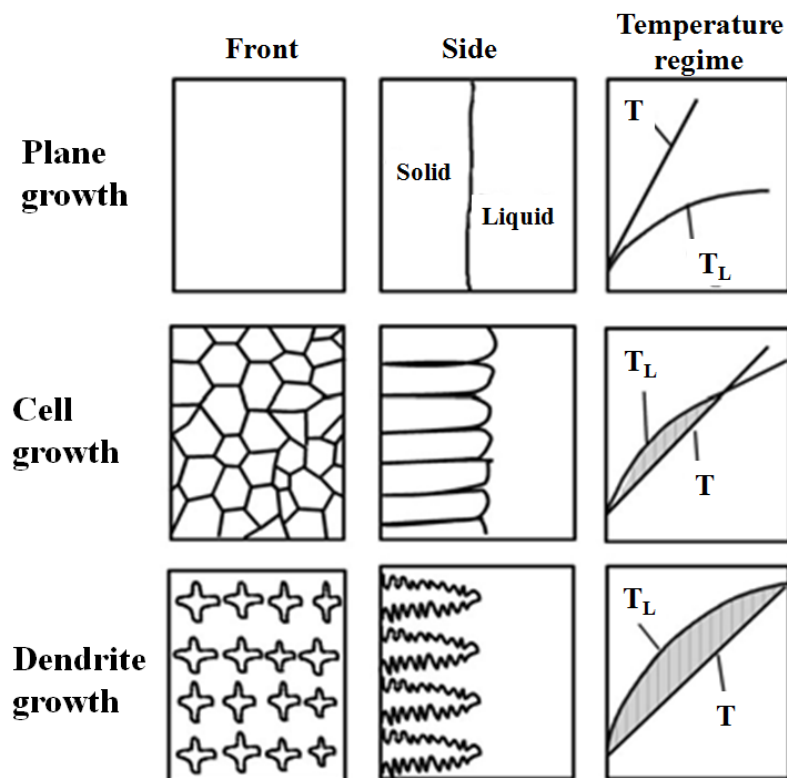


Fig. 3-9 Transition in Growth Morphology [32]

When, however, growth rate is increased, crystallographic effects begin to exert an influence and the cell-growth direction deviates toward the preferred crystallographic growth direction. As growth rate increases still further, the cross structure first becomes more apparent. That is secondary dendrite arms become observable.

According to the explanation of the perturbations on the solid liquid/interface, it can be said that with any solid/liquid interface of area, A , is associated an excess (interface) energy which is required for its creation. Therefore, heterogeneous systems or parts of systems which possess a high A/v ration will be in a state of higher energy and therefore unstable with respect to a system of lower A/v ratio.

The relative stability can be expressed by the equilibrium temperature between both phases (melting point). The change in melting point due to this curvature effect, often called the curvature or Gibbs-Thomson undercooling, is given by:

$$\Delta T_r = \Gamma \kappa \quad (3-13)$$

The curvature, k , and the Gibbs-Thomson coefficient, Γ , are here defined so that a positive undercooling (decrease in equilibrium melting point) is associated with a portion of solid/liquid interface which is convex towards the liquid phase. The curvature can be expressed as

$$\kappa = \frac{dA}{dv} = \frac{1}{r_1} + \frac{1}{r_2} \quad (3-14)$$

where r_1 and r_2 are the principal radii of curvature. The Gibbs-Thomson coefficient is given by:

$$\Gamma = \frac{\sigma}{\Delta s_f} \quad (3-15)$$

where Δs_f is entropy of melting and σ is S/L interface energy.

Solidification morphologies are determined by the interplay of two effects acting at the solid/liquid interface. There are the diffusion of solute (heat), which tends to minimise the

scale of the morphology (maximise curvature) and capillarity effects which tend to maximise the scale.

Solidification is a discontinuous phase transformation, which will not occur at any arbitrarily small undercooling. The reason for this arises from the large curvature associated with a crystal of atomic dimensions. This curvature markedly lowers the equilibrium temperature so that, the smaller the crystal, the lower is its melting point. The equilibrium melting point of the system is thus lowered by an amount, ΔT_r . The critical condition for nucleation is derived by summing the interface and volume terms for the Gibbs free energy:

$$\Delta G = \Delta G_i + \Delta G_v = \sigma A + \Delta g v \quad (3-16)$$

where σ is the solid/liquid interface energy and Δg is the Gibbs free energy difference between the liquid and solid per unit volume. Again assuming a spherical form (minimum A/v ratio) for the nucleus,

$$\Delta G = \sigma 4\pi r^2 + \frac{\Delta g 4\pi r^3}{3} \quad (3-17)$$

3.3.3. Primary and secondary dendrite arm spacing

The point of which the cellular structure becomes dendritic is a matter of terminology. One group of authors prefer to describe it as dendritic only when secondary branches can be discerned [54]. Some of authors think that the structure as dendritic when it is growing in or near its crystallographic orientation [57-60]. Another point of terminology of dendritic structure is more important: the difference between a dendrite and dendrite arm [51, 53].

The central portion of the structure which is growing in approximately the heat flow direction is termed a primary dendrite arm; the rods like protrusions perpendicular to the primary dendrite arms are the secondary dendrite arms. Qualitatively, secondary arms form because the approximately paraboloidal interface of the cell tip becomes unstable.

The development of perturbations at the constitutionally undercooled solid/liquid interface is only a transient phenomenon. The tips of the perturbations can readily reject solute while the depressed parts of the interface accumulate solute and advance much more slowly. The initial wavelength is too small for further rapid growth to occur, and the final result is the formation

of a cellular structure. Also, the spacing between the cells is not constant. The initial cellular morphology can adjust itself to give a more optimum growth form via the cessation of growth of some cells in order to decrease their number or by the division of cells in order to increase the number present. Furthermore, the larger centre cell have slightly perturbed surfaces and this suggests that, in the intercellular liquid, some driving force remains for further morphological change which might possibly lead to dendrite formation. When the driving force due to the temperature gradient difference is large, i.e. large constitutional undercooling, dendrites form instead of the cells. Cells are usually ellipsoid-like crystals which grow anti-parallel to the heat flux direction. They grow under conditions which are close to the limit of constitutional undercooling of the corresponding planar interface. On the other hand, dendrites are crystalline forms which grow far from the limit of stability of the plane front and adopt an orientation which is as close as possible to the heat flux direction or opposite to it, but follow one of the preferred growth axes. Equiaxed dendrites grow along all of the available preferred directions when the heat extraction is isotropic.

The growth rate, as well as the dendrite morphology or spacing, are all largely dependent upon the behaviour of the tip region (see Fig. 3-10).

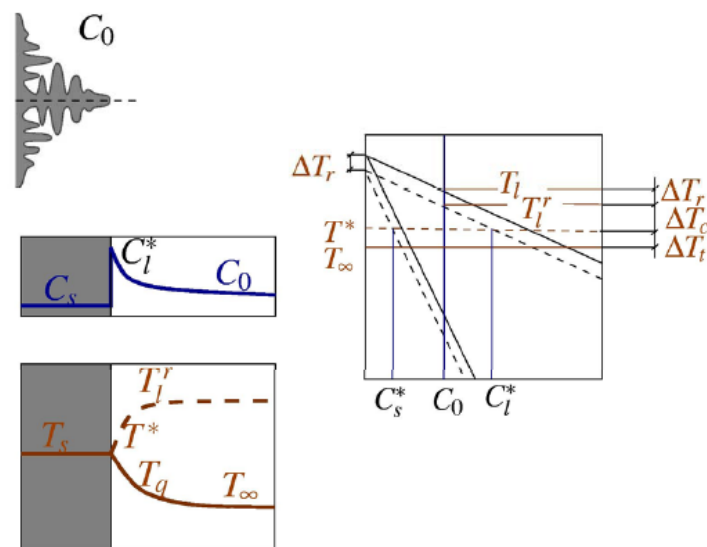


Fig. 3-10 Growth of the tip of dendrites

During the growth of the tip, either heat (in the case of pure metals) or heat and solute (in alloys) are rejected. The temperature and concentration at the tip of dendrite are denoted as T^* and C_l^* . These diffusion processes are driven by gradients in the liquid, and the latter are in

turn due to differences in temperature (ΔT_t) and concentration (ΔT_c) ahead of the growing crystal. After adding the temperature difference at the solid/liquid interface, caused by the curvature of the tip (ΔT_r), the coupling condition can be written:

$$\Delta T = \Delta T_c + \Delta T_t + \Delta T_r \quad (3-18)$$

In this equation, the possibility of kinetic undercooling has been neglected. This is a reasonable assumption in the case of materials, such as metals, which exhibit a low entropy of melting. This supersaturation (or the related undercooling, ΔT) represents the driving force for the diffusion of solute at the dendrite tip in an alloy. With increasing supersaturation, the growth rate of the new phase (the solid) will increase.

The actual dendrite morphology is, of course, much more complex than the simple platelike (or cylindrical) morphology used for calculation involving solid diffusion. Moreover, solute is not uniformly distributed in interdendritic areas but tends to be somewhat more concentrated between primary arms than between secondary. An example of dendritic morphology of solidification where can be distinguished primary ($DAS=\lambda_1$), secondary ($SDAS=\lambda_2$) and tertiary (λ_3) dendrit arm spacing is given in Fig. 3-11.

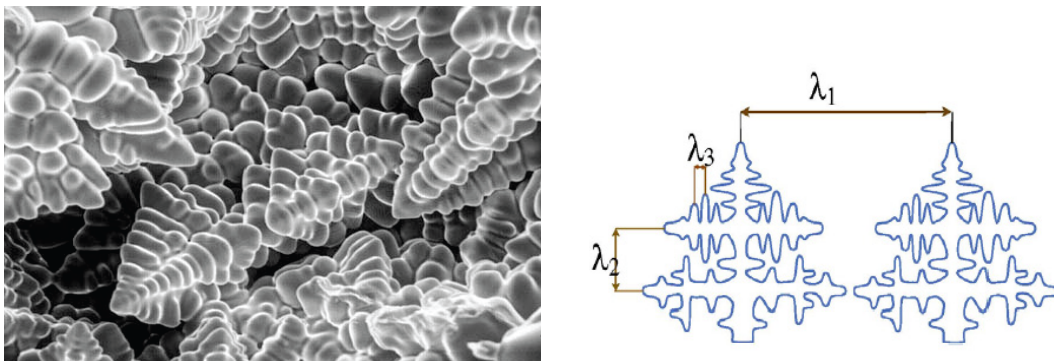


Fig. 3-11 Dendritic structure [64]

A convenient and widely used measured of the effects of solidification conditions on dendrite structure is dendrite arm spacing, i.e. the spacing between primary, secondary or higher – order branches. Generally, the spacing measured is the perpendicular distances between branches (Fig. 3-11). However, especially on more poorly defined structures, the random linear interception method has been employed. This mechanism of spacing adjustment is similar to that by which cells adjust their spacing. The driving force is the constitutional

undercooling in the region between the two primary dendrite arms. Apparently the dendrite is able to branch sufficiently to reduce this undercooling to a very low value. It has been previously mentioned that primary dendrite arm spacing depends on the product of thermal gradient and growth rate (Eq. 3-1), and results which have been reported correlate full with this parameter. Secondary dendrite arm spacing also depends directly on cooling rate or solidification time (Eq. 3-2) both columnar and equiaxed.

The effect of solidification time as leading parameter that determines the SDAS in aluminum alloy have been extensively investigated in the literature [49, 53, 55, 62-65]. Besides the solidification time, one of the most important casting process control parameters is the chemical composition of the melt.

Few years ago a group authors from Singapore [66] and China [67] published few papers about the effect of master alloys containing Ti and/or B on the grain size and dendrite arm spacing of AlSi8Cu2 and AlSi6MgCu aluminium alloys. Banghong Hu and HangLi [66] investigated the effect of additions of master alloys on the size of SDAS add into the AlSi8Cu2 (226S alloy according to DIN specification) alloy cast in a permanent mould. In their experimental work [66] the Ti addition contents were 0.11, 0.13, 0.15 and 0.17 wt %. The Ti:B ratios studied were 1:6, 1:4, 1:2, 1:1, 2:1, 4:1 and 6:1 at a selected Ti addition level. A commercial German Al-alloy, DIN226S was chosen for this study. Three types of master alloys were evaluated: binary Al-Ti (10 wt % Ti), and/or Al-B (5 wt% B) alloys and ternary Al-Ti-B alloys. The alloy was melt into graphite crucible. The die used for producing specimen was made of H13 steel and was pre-heated to 300 °C before casting. It was indicated that the optimum levels of Ti and/or B additions for the grain size refinement and the SDAS refinement is different. The grain size decreases rapidly with increase in Ti addition into the melt up to 0.13 wt %. Addition of Ti above 0.13 wt% does not affect the grain size significantly. Addition of 0.11 wt% Ti contributes significantly to SDAS reduction. Lina Yu, et.al [67], investigated the refinement efficiency of two different grain refiners AlTi5C0.25 and AlTi5B1 on the SDAS in the A356 alloy. They also found that the size of SDAS decreased by adding AlTiC grain refiner. Comparing the mechanical properties of A356 alloy before and after addition of AlTiC and AlTiB grain refiners, it was found that ultimate tensile strength and elongation have higher value in the presence of AlTiC grain refiner.

A.M. Samuel et al. [68] examined the effect of alloy composition and solidification conditions on changes in the dendritic and eutectic structures in Al-Si alloys containing strontium. A series of alloys Al-7%Si, Al-12%Si were selected, to cover a variety of alloy freezing ranges. In this paper it was shown that introduction of Sr to these alloys further decreases the eutectic

temperature, with a corresponding increase in the volume fraction of the primary α -Al phase. The primary dendrite solidification pattern changes from parallel rows to a branched form, producing an equiaxed type of structure and hence shorter primary dendrite lengths. The authors have explained that the length of the secondary dendrite arms is controlled by the rejection of solute atoms in front of the growing dendrites during solidification. According to that, the higher the alloying content in the alloy, the smaller the dendrite cell size. The solidification of α -aluminum primary phase leads to an increase in the silicon concentration in the remaining liquid. At the eutectic temperature, the primary Al-Si eutectic will start to precipitate consuming the residual melt between dendrite arms. Formation of a new Al-Si phase increases further concentration of residual elements leading to the formation of new phases. Recently, the group of authors [86] have studied the influence of process parameters such as: chemical composition, cooling rate, mold temperature and pouring temperature on the size of SDAS of as-cast aluminum cylinder heads. The influence of chemical composition has been analysed using three aluminum alloys AlSi7Mg0.3, AlSi9Cu1Mg0.3 and AlSi7Cu3Mg0.3. They found that various content of silicon and copper have significant effect on the size of SDAS even at high cooling rate. However, the papers did not cover the full range of silicon and copper contents that could be interesting for producers of as-cast aluminum parts. It was also reported that increase of pouring temperature and mold temperature lead to the increase of SDAS.

3.3.4. Solidification features of Al-Si-Cu alloys-Dendrite Coherency

The solidification of cast Al-Si alloys starts at liquid temperature with precipitation of a primary aluminum α -phase. Further decrease in solidification temperature is followed by additional growth of primary phase that solidifies in the form of dendrite. Short period of time they will grow freely without touching each other. In the dendritic solidification of alloys, the solute redistributes due to the difference in solubility between the liquid and solid phases. The solute rejected from the solid-liquid interface develops a region in the liquid in which the actual temperature is lower than the liquidus temperature and leads to constitutional undercooling [55-64].

Major and minor metallurgical reactions, that are thermodynamically strong enough in terms of latent heat evolution are manifested on the cooling curve by inflection points and slope change. Upon completion of the solidification process, the test sample structure and its properties can be quantified from these reactions [69-73].

Characteristic temperatures for the AlSi7Cu4 alloy are depicted on the cooling curve and its time derivative (Figure 3-13 and Table 3-3). Some of these characteristic points can be used to determine microstructure properties of the casting alloy such as: grain size, dendrite arm spacing, dendrite coherency point and morphology of Al-Si eutectic.

A cooling curve and its time derivative can also be used for the determination of fraction solid [74, 75]. The shape of the cooling curve is a result of the heat lost to the surroundings by the cooling test sample and the heat evolved in the cup during the phase transformation. The amount of heat evolved from a solidifying test sample can be calculated as the integrated area between the first derivative curve and the zero line. The amount of heat is proportional to the fraction solid.

Table 3-3 - List of characteristic temperatures with corresponding symbols [74]

Point	Description	Symbol
1.	α - Al - dendrite nucleation (liquidus) temperature	$T_{\text{NUC}}^{\alpha, \text{DEN}}$
2.	α - Al - dendrite under cooling temperature	$T_{\text{MIN}}^{\alpha, \text{DEN}}$
3.	α - Al - dendrite growth (recalescence) temperature	$T_{\text{G}}^{\alpha, \text{DEN}}$
4.	α - Al - dendrite coherency point	$T_{\text{COH}}^{\alpha, \text{DEN}}$
5.	Al - Si eutectic nucleation temperature	$T_{\text{E,NUC}}^{\text{Al-Si}}$
6.	Al - Si eutectic minimum temperature	$T_{\text{E,MIN}}^{\text{Al-Si}}$
7.	Al - Si eutectic growth temperature	$T_{\text{E,G}}^{\text{Al-Si}}$
8.	Copper rich eutectic nucleation temperature	$T_{\text{E,NUC}}^{\text{Cu}}$
9.	Copper rich eutectic minimum temperature	$T_{\text{E,MIN}}^{\text{Cu}}$
10.	Copper rich eutectic growth temperature	$T_{\text{E,G}}^{\text{Cu}}$
11.	End of solidification process (solidus temperature)	T_{END}

Bäckerud and co-workers developed a two-thermocouple thermal analysis method to monitor the solidification process of alloys [34, 52, 75]. One thermocouple is located at the center (T_c) and another close to the inner wall (T_w) of a crucible.

More detailed solidification process characteristic can be achieved using the first derivative of the obtained cooling curve plotted against the time. The first derivative cooling curve indicates characteristic temperatures such as precipitation of primary phase, primary eutectic and secondary eutectic reaction as well as other reaction present in the aluminium alloys. The

derivative at each point of the curve represents the rate of cooling of the metal in the thermal analysis test cup. An increase of the derivative means that some latent heat has been released which slows down the cooling rate and indicates on the formation of a new phase in the system. During the solidification of the test samples, the thermally weak events can not be easily detected on the cooling curves. In order to get more details about some points on the cooling curves, the second or even the third derivatives plotted versus time are sometimes used.

According to Bäckerud's method, the dendrite coherency point (DCP) is determined by identifying the point of minimum temperature difference at the $(T_w - T_c)$ curve. When the primary dendrites first impinge each other, the secondary and higher order branches will start to grow/expand. The temperature, time, and solid fraction at this point are called coherency temperature, time, and solid fraction, respectively. At this stage, the morphology of the mushy zone can be envisaged as an interconnected skeleton throughout the solidifying volume and this moment represents the transition from mass to interdendritic feeding (Fig. 3-12). The assumption that the DCP occurs at this minimum is based on the theory that the establishment of dendritic network will result in a substantial change in the heat transfer between the wall and the central region of the test sample.

Dendrite coherency was postulated to correspond to discontinuous increase in thermal conductivity of the mushy material. Chai and co-workers subsequently developed a mechanical or rheological technique with a paddle stirrer to identify the coherency point by changes in the mechanical strength of the mushy material [76]. The mechanical method is based on the fact that the shear strength of the solidifying melt only begins to develop at DCP. This is usually measured by monitoring the torque required to rotate a paddle or disc in the melt at a constant rate. At the DCP the required torque rapidly escalates, and the point at which this deviation is measurable is taken as the DCP.

The group of Mexican authors has been recently developed the third method to determine the DCP, which is based on the measurements of the thermal diffusivity [77]. A series of samples of an AlSiCu alloy cast with and without the addition of modifying and refining elements was used in that work.

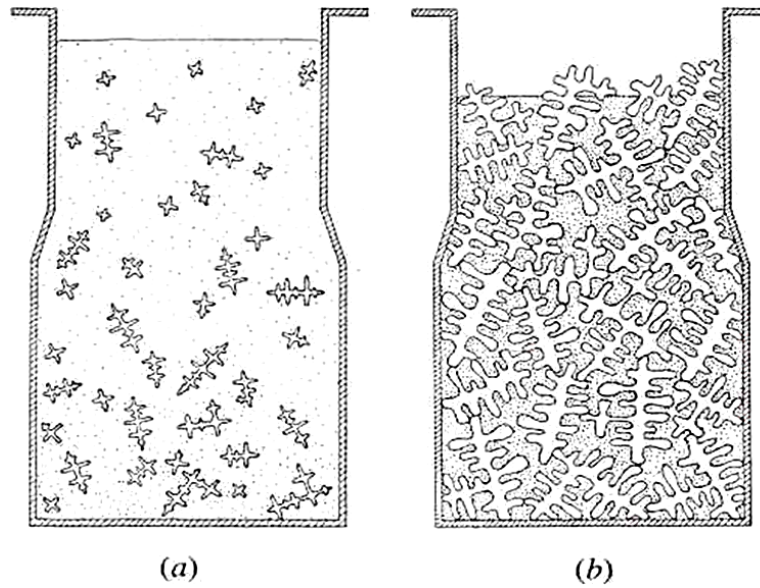


Fig. 3-12 Feeding of mushy zone during the solidification (a) mass; (b) interdendritic feeding

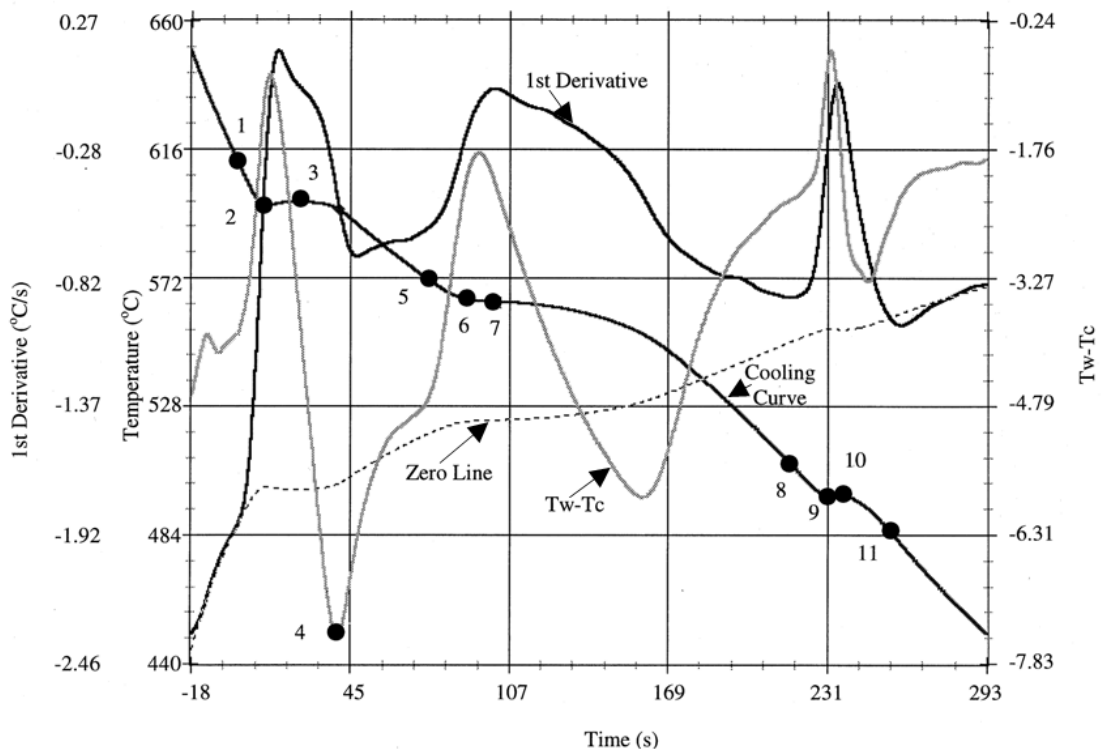


Fig. 3-13 Cooling Curve Time Derivative and Base Line Obtained by Thermal Analysis of AlSi7Cu4 alloy (unrefined and unmodified) [74]

Spencer *et al.* [78] observed that melt stirring during solidification postponed the coherency and noted that the resultant microstructure contained small rounded dendrites.

The coherency fraction solid and temperature are considered to mark the transition from mass to interdendritic feeding, to compensate for shrinkage in casting processes. After coherency, the restriction imposed on liquid flow, and the development of contractionally induced stresses in the continuous solid network, can result in common casting defects such as macrosegregation, hot tearing, shrinkage and gas porosity. Several authors have suggested that the coherency point may be an important indicator of alloy castability [79-81]. Therefore, a lot of importance must be attached to complete understanding of the solidification behaviour at the DCP and the factors affecting the DCP.

Recently a single thermocouple technique has been developed by Djurdjevic et al. [82]. The DCP is defined as the minimum point of the 2nd derivative curve of temperature vs. time of one centrally located thermocouple. It is obvious that all compared methods of analysis yield similar results and can be used indistinctly to evaluate coherency.

The solidification conditions, chemical compositions of alloy and addition of grain refiners are major factors that have significant impact on the dendrite coherency temperature. Independent from applied techniques, it has been verified that faster cooling rate and increase in solute concentration postponed the coherency point to the lower temperature [74, 84]. L. Arnberg et al. [75, 79] already analyzed the impact of grain refiner (Ti) on dendrite coherency in Al – Cu 4 wt % alloy. They found that any increase in the Ti content up to 0.22 wt.% by two different cooling rates (0.5 and 1.0 °C/s) increase significantly the fraction solid at dendrite coherency temperature for almost 20%. According to the authors, an increase in the Ti concentration decreases the dendritic growth rate greatly and the volume fraction of grain increases very slowly, decreasing the temperature interval from dendrite coherency temperature to eutectic silicon temperature.

Comparing different alloy systems, Veldman et al. [83] found that the greater the liquidus slope correspond to the higher the coherency point. Recently Veldman et al. [85] analyzed the impact of various contents of Si and Cu on the DCP. In their experiments silicon was varied from 1 to 10.3 wt %; copper from 0 to 4.4 % while the content of Mg and Fe were kept constant. Total of ten Al alloys have been investigated. They found using both, thermal analysis (for two cooling rates, 0.7°C/s and 2.7°C/s) and rheological techniques that fraction solid at DCP decrease as a function of increasing Si content. According to their investigation copper does not have a significant effect on the fraction solid at coherency.

Although dendrite coherency has long been of interest, still there is a lack of knowledge about impact of some particular alloying elements on this feature in the system of Al-Si-Cu

alloys, which are of crucial importance for automotive industry. The lack of literature data is more related to the impact of other major and minor alloying elements.

S. Gowri and co-workers [86] investigated the effect of different alloying elements on the solidification characteristics of Al-Si-Cu-Mg-Fe alloy at two cooling rates (0.4 °C /s and 10 °C /s using the thermal analysis method. They varied the content of copper, iron, magnesium, zinc and manganese in the range of 3.22 - 4.09 wt %, 1.01 - 1.70 wt%, 0.06 - 0.50 wt %, 1.69 - 3.00 wt%, and 0.16 - 0.46 wt% respectively. They showed that the liquidus and eutectic temperatures are increased as the amount of iron is increased. They found that the increase in manganese increases both the melting point and the eutectic temperature by 4 °C at the higher cooling rate. The authors have also reported that the increase in magnesium up to 0.30 wt% did not affect the solidification. The eutectic temperature changed approximately 1 °C for each 0.10 wt of added magnesium.

In the paper of J. Cho et al [87] the influence of different copper content in three different Al-Si alloys was observed. They have shown also that increasing copper decreases the melting point of alloy considerably as well as the eutectic temperature. The phase formation temperature of Al₂Cu, however, is increased.

In the paper of S.S. Sreeja Kumari et. al. [88] it was shown using thermal analysis that Mn (0.4%) addition to Al-7Si-0.3Mg-0.8Fe alloy changes the morphology of platelet iron phase to script form leading to significant improvement in tensile properties. However, there is no significant improvement in impact strength. Be (0.2%) changes the platelet morphology of iron phase to Chinese script form, which are seen only inside the α - Al in slow cooling (sand cast), and both in the interdendritic as well as inside the α -Al in fast cooling (permanent mould casting) condition. This morphological change is responsible for the significant improvement in both the tensile and impact properties. Addition of Be, Ca and Sr to Mn added Al-7Si-0.3Mg-0.8Fe alloy improves the impact strength significantly. This is due to the modification of the eutectic Si from acicular to fibrous form and refinement of the platelet α -phases. On the other hand, combined additions of Be + Mn, Ca +Mn and Sr +Mn lead to a reduction in the impact strength compared to individual additions of Be, Ca and Sr. The best combination of both tensile and impact properties have been obtained in the combined additions of Be + Mn, Ca +Mn and Sr +Mn to Al-7Si-0.3Mg-0.8Fe alloy. A trace amount of Be (0.005%) addition to Ca and Sr leads to superior tensile properties compared to Ca and Sr additions alone.

3.3.5. Modelling of microstructure parameters

Numerous solidification studies have been reported with a view to characterizing the microstructural parameters such as primary dendrite arm spacing (λ_1), secondary dendrite arm spacing (λ_2), dendrite tip radius (r) and mush zone depth (d') as a function temperature gradient (G) and growth rate (V) ahead of the microscopic solidification front [89-94].

A literature survey shows that several theoretical studies and theoretical models [95-101] have been used to examine the influence of solidification parameters (G , V) on microstructure parameters (λ_1 , λ_2 , r and d). According to these results an increase in the solidification parameters results in a decrease in microstructure parameters.

Hunt allowed for the interaction of the diffusion fields between neighboring cells. The relationship between λ_1 and solidification parameters (G , V , C_0) for a spherical dendritic front with the growth condition for dendrites is determined by the minimum undercooling. Another theoretical model to characterize λ_1 as function of G , V and C_0 was developed by Kurz and Fisher. They assumed that the shape of the cell or dendrite can be approximated as ellipsoids and using the marginal stability criterion for an isolated dendrite or cell, they simplified their results for the low velocity and for the high velocity. Another theoretical model to characterize λ_1 as function of G , V , C_0 was developed by Trivedi [85]. Trivedi modified the Hunt model by inserting marginal stability criterion.

Hunt and Lu [103, 104] investigated the cellular/dendritic array growth by using a numerical model. They presented analytic expressions that fitted with the numerical results. The Okamoto Kishitake model [105] is a simplified method of correlating primary dendrite spacing with solidification parameters. To develop such a model, Okamoto and Kishitake assumed the secondary dendrite arms to be plates that become thicker as the solidification goes on.

C.T. Rios and R. Caram [106] carried out directional growth experiments with the alloy Al-Si8.5-Cu2.5. They investigated directional solidification parameters. The results obtained were compared with results furnished by the models of Hunt, Okamoto Kishitake, Kurz-Fisher, Trivedi and Hunt-Lu. That study shows that an increase in the growth rate produces a decrease in the dendrite spacings. Also, a variation in the thermal gradient at solid/liquid interface deeply affects the primary dendrite spacings. At low growth rate, the effect of temperature gradient on the primary spacing is not very considerable. If the growth rate increases, the influence of temperature gradient becomes more significant. As temperature gradient is decreased, there is a tendency to increase the primary dendrite spacings. At low

temperature gradient values, the primary spacings are less sensitive to the growth rate variation. The comparison between experimental results and theoretical results furnished by the five mentioned theoretical models reveals that the Kurz -Fisher and Hunt Lu models allow one to predict efficiently the primary dendrite spacing as a function of directional solidification parameters.

4. Experimental part

The experimental part of this work can be divided into three subparts. As a first, the preliminary examinations related to AlSi7Cu3 cylinder heads cast using the tilt pouring die casting process. The microstructure observation on the real casting with relatively complex geometry as in the cylinder heads has been conducted in order to estimate the SDAS in the thermally and mechanically stressed area such as combustion chamber surface. Since the SDAS value of cylinder head in the mentioned area has to meet very strict industrial demands there is a need for comprehensive knowledge about the solidification phenomena as well the parameters influencing on the solidification behavior of Al-Si-Cu hypoeutectic alloys. For that reason in the second part of the experimental study, the impact of casting parameters such as pouring temperature, mold temperature and cooling conditions on the SDAS of the basic alloy has been examined. The third part of experimental study has been basically focused on the examination of chemical composition variations on the solidification behavior of Al-Si-Cu alloy where the special attention has been paid on the changes of SDAS and DCP.

4.1. Design of laboratory experiments

In designing automotive parts, it is important to have an intimate knowledge of how alloy solidifies at different cross sections of the cast part and how this influences mechanical properties. This knowledge enables the designer to ensure that a casting will achieve the desired properties for its intended application.

The microstructural constituents present in AlSi7Cu3 (A319) alloy are primary aluminum phase, typically complex multiphases comprising eutectic (acicular) Si, as well as numerous intermetallic phases. These microstructural characteristics, manifested variously in the grain size, secondary dendrite arm spacing, type, shape and structure of constituent phases and the porosity distribution, together influence the resulting properties, often in an interactive manner.

However, before discussion about the relationship between the microstructural features and mechanical properties of alloy, the crucial question regarding the parameters influencing the microstructure features should be taken firstly into account. The main problematic of this

study is focused on the relationships between the casting parameter and chemical composition of the solidification features as SDAS and DCP of AlSiCu alloy.

The effect of mold temperature and cooling conditions on the SDAS of the basic alloy was carried out at the permanent metal mold particularly designed to ensure the changes of the mold temperature as well cooling conditions during the solidification process. The effect of pouring temperature and chemical composition variations on the SDAS was investigated using the laboratory ceramic crucible where the mass of sample amounts 100 ± 10 g. The technique of thermal analysis-computer aided cooling curves in conjunction with metallographic analysis was applied in order to investigate the solidification characteristics of alloys, namely characteristic temperatures/times and the microstructural evolution of Al-Si-Cu alloys.

Design of the laboratory experiments is made in such way to determine the relationship between the different factors affecting the solidification path and features of Al-Si7-Cu3 alloys which are here defined as the outputs of the solidification process with special emphasis on the primary solidification reaction concerning the growth of secondary dendrite arms or other words the changes of the value of SDAS.

Experimental design involved designing a set of experiments in which some relevant factors were varied systematically. The results of these experiments were analyzed in order to identify optimal conditions, the factors that most influence the results and those details such as the existence of interactions and synergies between factors.

In this work it was considered as the independent variables (the parameters that were changed) such as variation of chemical composition of the Al-Si7-Cu3 alloy, pouring temperature and mold temperature. Variation of chemical composition includes the changes of the major and minor alloying elements (Si, Cu, Mg, Ti, Zn, Sr) contents. The value of secondary dendrite arm spacing (SDAS) was referred as the paramountly dependent variable or output of the process. Beside the SDAS, the change of the DCP point was also analyzed as a function of chemical composition. The other characteristic points of the solidification curve were taken as the subordinate outputs and they also were considered in this work because of their importance for the complete solidification process.

The schematic view of experimental design can be seen in Fig. 4-1.

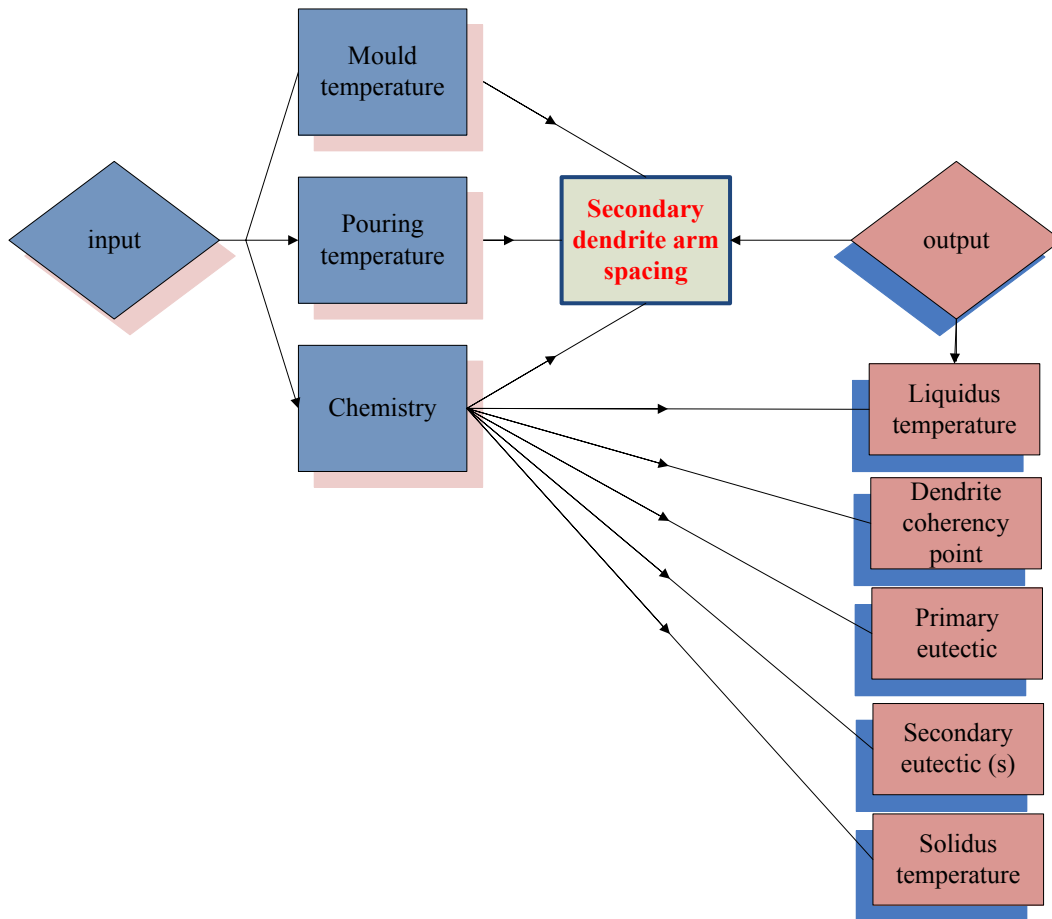


Fig. 4-1 Design of laboratory experiments

4.2. Experimental procedure

4.2.1. Material

Automotive cast A319 alloys have been increasingly used in the manufacture of cylinder heads due to a combination of good fluidity properties and mechanical strength.

Considering the importance of A319 alloy in automotive industry, especially for casting the cylinder heads, this alloy has been chosen as the basic alloy in this work. The table 4-1 shows standard chemical composition of A319 alloy.

In the industrial experiments and experiments performed to estimate the effect of pouring temperature and mold temperature, the chemical composition was held in the range according to the standard specification. As the alloy composition is not strictly defined while the content

of chemical elements is given in some concentration range, such concentration changes regarding to Si, Cu, Mg, Ti, Zn and Sr were varied more or less in agreement with the alloy specification defined by standard.

Table 4-1 Standard chemical composition of the basic alloy AlSi7Cu3

Si	Fe	Cu	Mn	Mg	Cr	Ni	Zn	Pb	Sn	Ti	Sr	rest
wt %												
6.0-8.0	<0.5	2.8-3.8	<0.4	0.05-0.5	<0.05	<0.25	<0.4	<0.10	<0.10	<0.3	0.007-0.015	Al

4.2.2. Industrial tests-tilt pouring die casting process

Industrial experiments related to casting of cylinder head were carried out using the method of gravity die casting with the tilt pouring of melt. According to the tilt pouring concept (Fig. 4-2), the melt is filled into a transverse runner disposed on the longitudinal side of a casting mold by top casting characterized by that the casting mould (1) first is tilted at an angle of 45° to 70° on its longitudinal axis (5), then the filling of the melt into the transverse runner (2) starts until approx. one fifth of the melt required for the casting is filled in the transverse runner (2) without the melt already flowing into the mould cavity (6), and afterwards while continuously filling more melt into the transverse runner (2) the casting mold (1) is pivoted from the tilted position into vertical direction in such a way that the melt flows into the mold cavity (6) from the transverse runner (2) along a casting mold wall.

The mold (1) is then tilted back to a vertical position, whilst the transverse channel (2) continuously to be filled with the molten alloy (4) and the latter flow along a side wall of the mold into the mold cavity (6) via outlets (3), as is the case in conventional tilt pouring process. The filling of the molten melt and the tilting back to the mold (1) are coordinated in such a way that the mold (1) reaches its vertical position once the mold cavity has been (6) filled to the level of the feeder attachment.

In order to estimate the relationship between the SDAS in the combustion chamber surface and the cooling rate, the experiments of in situ thermal analysis of AlSi7Cu3 cylinder heads produced by the tilt pouring gravity die casting process were conducted.

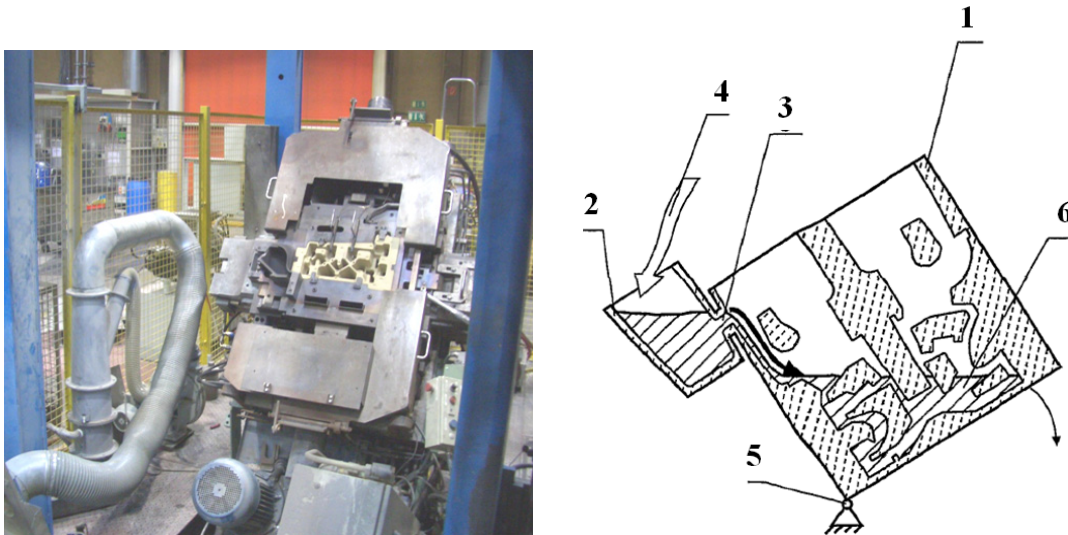


Fig. 4-2 Tilt Pouring Gravity Die Casting Process

The preparation of thermocouples on the sand core before the pouring process is demonstrated in the Fig. 4-3. The thermocouples have been fixed to the sand cores in such way that the distance of the tip of thermocouples was 4 mm from the combustion chamber surface of cylinder heads. At the same distance from the surface, five thermocouples were positioned in each cylinder of cylinder head as it was depicted in Figure 4-4.



Fig. 4-3 In situ thermal analysis on the real casting of AlSi7Cu3 alloy

The temperature of the melt measured in crucible before each pouring process was about 720 °C. The water flow through the cooling channels was kept constant at 8 l/h during the solidification process for all cylinder heads examined in this work.

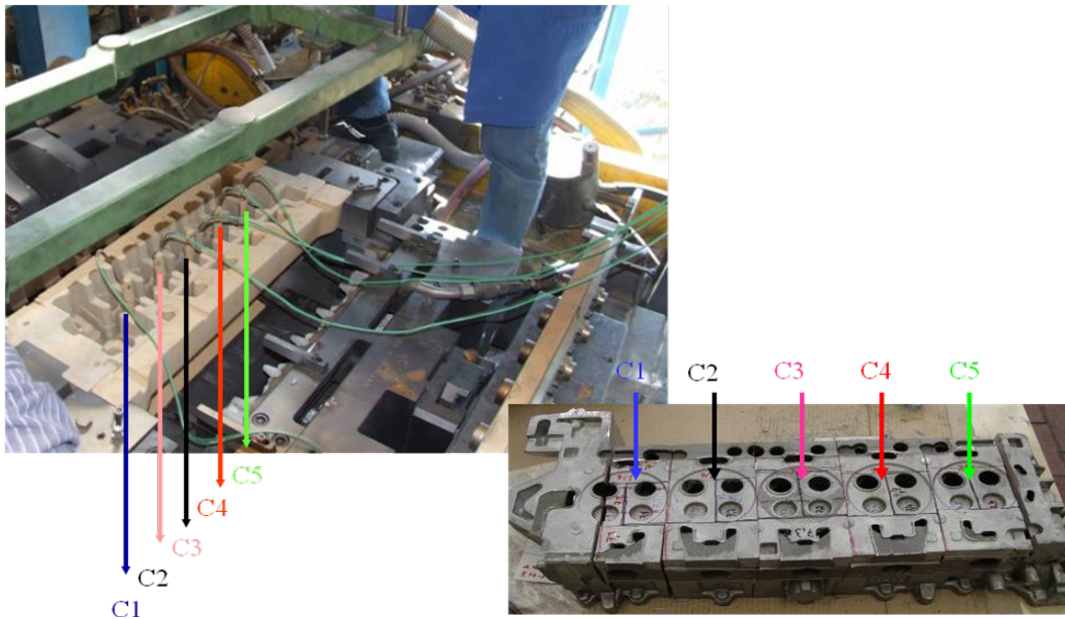


Fig. 4-4 Positions of thermocouples in cylinder head

Under the mentioned conditions, in situ thermal analysis has been performed in order to achieve the information about the cooling rate measured by five thermocouples. The SDAS was measured quite close to the tips of all five thermocouples. The metallographic sampling for one cross section of the cylinder head is presented in Fig. 4-5.

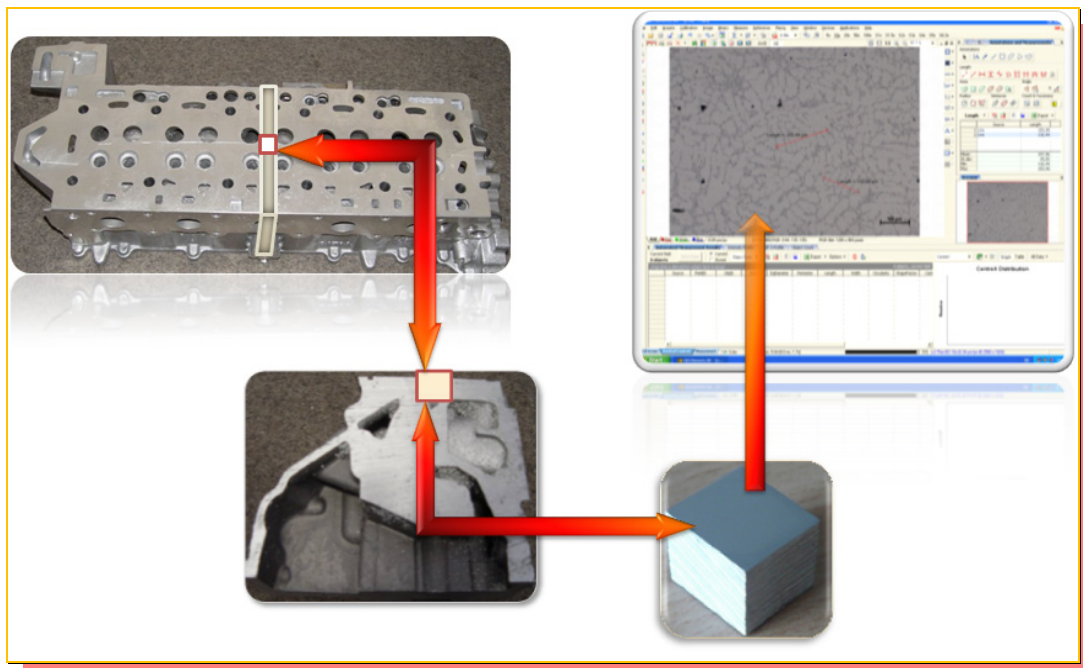


Fig. 4-5 Sampling and measurement of SDAS in AlSi7Cu3 cylinder head

4.2.3. Laboratory test in permanent metal mold

The AlSi7Cu3 alloy used in these experimental studies has been supplied in the unmodified form. The chemical composition of the alloy was determined using the Optical Emission Spectroscopy (OES) showing the following composition (in wt.%): 7.74 Si, 0.25 Fe, 3.493 Cu, 0.176 Mn, 0.175 Mg, 0.0104 Cr, 0.0288 Ni, 0.130 Zn, 0.020 Pb, 0.003 Sn, 0.115 Ti, 0.0012 Sr and 88.77 Al.

The alloy was remelted in the laboratory furnace (the maximum capacity of 10 kg) and held at $745^{\circ}\text{C} \pm 5^{\circ}\text{C}$. Before pouring the melt was degassed for 15 min by passing dry argon. Refiner and modifier were not used for the melt treatment. The casting temperature was kept constant at 720°C .

In order to estimate the effect of mold temperature and cooling conditions on the SDAS one set of experiments was performed using the permanent metal mold made of hot work tool steel X40CrMoV51 (H13). Design of the permanent metal mold is shown in Fig. 4-6.

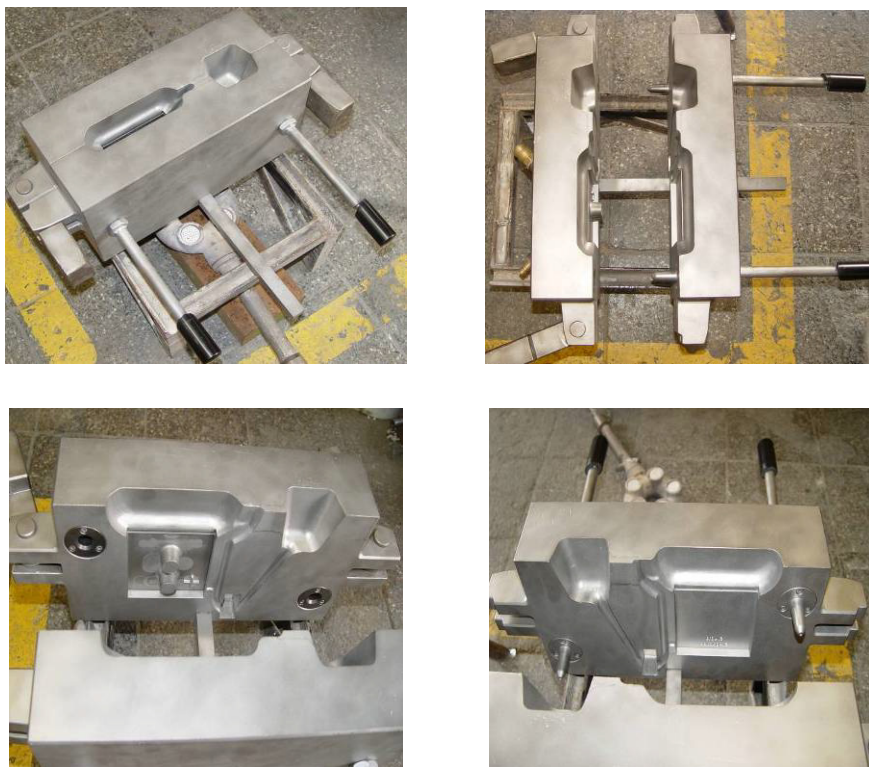


Fig. 4-6 Design of permanent metal mold

Before the pouring of the melt, the mold was pre-heated up to three different temperatures, i.e.: 350, 300 and 250 °C using the laboratory burner. In order to ensure the proper cooling conditions “internal” cooling technique using water as a cooling medium has been used. Basically, the cooling conditions were changed for each mold temperature, including the cooling with and without water flowing through the cooling channel incorporated into the one side of the mold (Fig. 4-7).

Before the pouring of molten metal, cavity surfaces were coated with a thin layer of heat resistant material such as sodium-silicate. A ceramic filter was placed in slag trap of mold before the casting. The molten metal was fed directly into the mold under gravity.

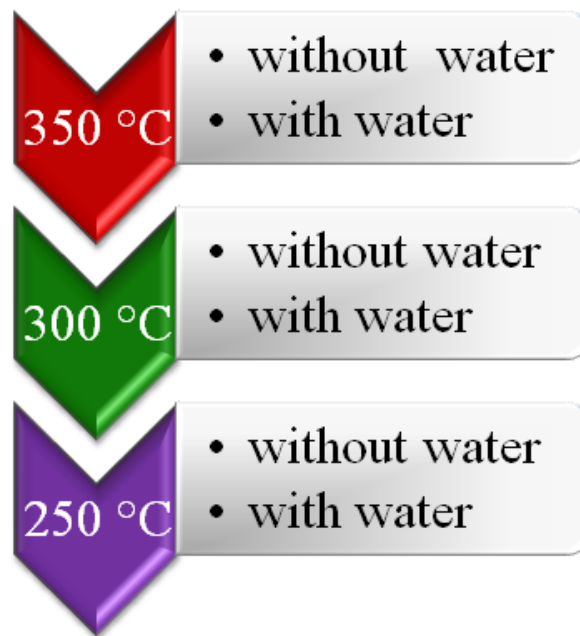


Fig. 4-7 Experimental conditions

The temperature variations during the solidification process of the melt were controlled by placing two thermocouples in mould cavity, (1) and (2) as it can be seen in Fig 4-8. Due to the control of pre-heating of the mold or other words the mold temperature one thermocouple (3) was inserted in the outer wall of the left mold die. The distance between the thermocouples positioned in the mold cavity was 5 cm and the tips of both thermocouples were positioned at 2 cm from the bottom of casting (see Fig. 4-8 right). The temperature of water before the casting process was constant, i.e. 12 °C.

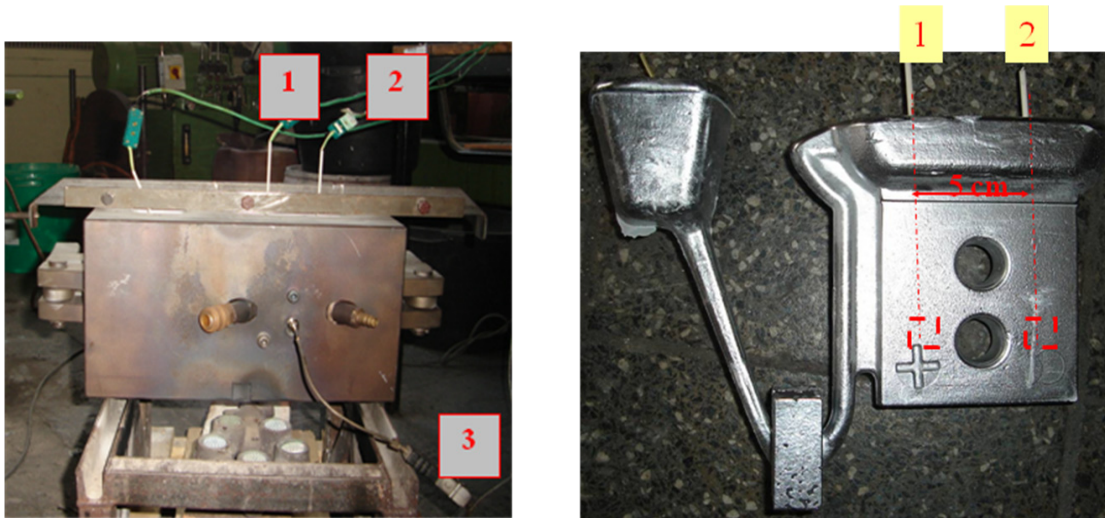


Fig. 4-8 Position of thermocouples in mold cavity and in casting

The analysis of the cooling curves was supplemented by metallographic analysis. Samples for metallographic examination were sectioned from the obtained castings (corresponding to each experimental condition) and taken from the positions where the tip of thermocouple 1 was positioned. Samples were prepared by standard grinding and polishing procedures. NIKON Epiphot 200 light optical microscope has been used for the microstructure observation. The linear interception method was utilized to measure the SDAS which was determined as a ratio of length segment to the number of arms. The image analyzer software, NIS Elements 2.10 was utilized to estimate the size of SDAS. The final size of the SDAS has been obtained as an average value of at least 10 measurements.

The solidification process of AlSi7Cu3 alloys in the permanent metal mold was also simulated by WinCast Finite Element Software taking into account all experimental parameters (experimental conditions, as well as physical properties of alloy and mold geometry). Mathematical model used for the calculation of SDAS was based on the equation (3-2). By substituting an alloy-specific value of C (in this work the value of C was 1.4) into the previous equation, the magnitude of SDAS can be easily calculated for each volume that comprises the casting model.

In order to estimate the sensitivity of mathematical model on changes in mold temperatures and cooling conditions, the experimental values of SDAS corresponding to the position of the tip of thermocouple 1 were compared with the calculated values of SDAS resulting from the simulation process which corresponds to the same position as in the real casting.

4.2.4. Laboratory test in ceramic crucible

As it was denoted previously, the effect of pouring temperature on SDAS as well the effect of chemical composition of the alloy on SDAS and other solidification features were evaluated performing the experiments in the ceramic crucible.

The pouring temperature of AlSi7Cu3 melt, the pouring temperature has been varied in the range of 650-750 °C. The same casting parameters like filling rate, total casting time (kept constant at 5 s), melt composition and quantity were adopted. The chemical composition of alloy was the same as it was during the experiments in permanent metal mold (all in wt.%): 7.74 Si, 0.25 Fe, 3.493 Cu, 0.176 Mn, 0.175 Mg, 0.0104 Cr, 0.0288 Ni, 0.130 Zn, 0.020 Pb, 0.003 Sn, 0.115 Ti, 0.0012 Sr and 87.77 Al. For each value of the pouring temperature three trials were carried out and the SDAS values has been determined for all three probes and finally expressed as an average value of three trials.

The alloying elements investigated in this study are silicon, copper, zinc, magnesium, titanium and strontium. The content of the major and minor alloying elements has been varied more or less within the specification limit of the basic alloy.

Previously prepared melt of each targeted alloy was first charged in the ceramic crucible, loaded in an electric resistance furnace and then melted. During all experiments the melt temperature in the furnace was kept constant at $745^{\circ}\text{C} \pm 5^{\circ}\text{C}$. After melting all samples were left to solidify under the same conditions. The sample mass was $100\text{g} \pm 2\text{g}$.

The alloys containing different Si and Cu wt% used in the experiments were synthetically designed to cover the Si level corresponding to the upper and lower limit of the standard basic alloy and the copper level ranged from 1–4 wt.%. All other elements were kept approximately constant. The synthetic Al-Six-Cux alloys containing different Si and Cu content were melted in electric resistance furnace. The melts were first degassed in order to obtain the lowest possible hydrogen level in the liquid alloys and after that were covered with a protective nitrogen gas atmosphere to prevent hydrogen and oxygen contamination. No grain refining agents were added to melts.

The AlSi7Cu3 alloy was remelted in electric resistance furnace at 750 °C. The melt was degassed for 15 min by argon. A few minutes before pouring in the ceramic mold, different Ti content was added in the form of master alloy Al-5Ti-1B and then stirred to ensure the uniform distribution of the refiner in the melt. The aimed content of titanium was 0.08-0.14 wt%.

In order to examine the effect of Zn and Mg, initially the basic AlSi7Cu3 alloy was remelted in the electric resistance laboratory furnace. The melt was degassed passing dry argon. The both metals, Zn and Mg were added in the pure form in the concentration range 0.73-3.0 wt% and 0.2-3.0 wt% respectively. The modifiers and refiners were not used for melt treatment. The effect of strontium addition was examined using the same basic alloy AlSi7Cu3 alloys where the strontium content was varied between 1 and 210 ppm. The melt was practically modified through the addition of master alloy (AlSr10). An incubation time of 20 minutes was allowed after the strontium addition prior to collecting the thermal analysis test sample.

The chemical composition of all prepared sample of Al-Si-Cu alloy containing varied content of chemical elements was determined using Optical Emission Spectroscopy (OES).

There were three trials for each content of chemical elements. All experimental values are expressed as an average value of three measurements including as well the chemical composition.

The solidification process has been studied by thermal analysis technique - computer aided cooling curves supplemented with the subsequent quantitative and qualitative metallographic analysis of the solid samples. One short description of the experimental methods and techniques used in this work is given in the following text.

4.3. Experimental methods and techniques

4.3.1. Thermal analysis

First of all, it is necessary to underline that thermal analysis actually consists of several different measurement techniques such as:

- Differential Thermal Analysis (DTA),
- Differential Scanning Calorimetry (DSC),
- Computer Aided Cooling Curve Analysis (CA-CCA).

In this study the method of computer aided cooling curve analysis has been used to observe the solidification process of AlSi7Cu3 alloys.

The cooling curve method is useful for commercial applications for a number of reasons: it is simple, inexpensive and provides consistent results. This technique is particularly useful for drawing fundamental relationships between cooling curve characteristics and melts, i.e. test samples.

In the previous chapter it was given a state-of-the-art of computer aided cooling curve analysis, concerning the identification of the major and minor metallurgical reaction as well as determination of solidification features such as denoted in the Table 3- 4. It was also given a short description of the method developed by Bäckerüd and co-workers that was generally used in this work.

The Bäckerüd's method with two thermocouples has been especially used to examine the solidification process in the ceramic mold. In this case, the cooling curves were recorded by placing two thermocouples (K type), one in the centre (T_c) and one close to the wall (T_w) of and the data acquired using the proper acquisition system. The temperature difference curve T_w-T_c versus time has been used to the determined the DCP.

The temperature was measured in the range of 750 - 450 °C. The thermal analysis (TA) samples were cut into two halves. One half of TA sample was used to determine the chemical composition and another one to estimate the SDAS close to the tip of the central thermocouple.

The obtained cooling curves and its first derivatives were used to determined characteristic point appearing on cooling curve as well to calculate the cooling rate and/or solidification time. The cooling rate was calculated as the ratio of the temperature difference between the the liquidus and solidus temperature and corresponding times. The time between the liquidus and solidus point is denoted here as the total solidification time.

Speaking about the effect of chemical composition of the alloy on the SDAS and other solidification features, this effect may not be especially neglected in the case of DCP point. As the results of this PhD thesis reveal, the DCP point shifts to the lower levels when the content of the Si, Cu, Mg, Ti and Zn increase. The results indicate that such changes of chemical composition were more emphasised in the case of the DCP then the eutectic point which additionally guides us to the concluding remarks, that means the time between the DCP point and eutectic point becomes shorter as the content of Si, Cu, Mg, Ti and Zn increases. Taking into account the definition of the DCP point, it is proposed in this work to consider a novel parameter detected by cooling curves analysis which actually matches well with the growth rate of secondary dendrite arms. The time interval between the DCP point and the Al-

Si eutectic nucleation temperature is denoted as $\Delta\tau^*$. In this study, the SDAS value has been correlated with total solidification time, t_f and novel parameter, $\Delta\tau^*$.

Many researchers have experimentally studied the effect of the total solidification time on the SDAS and verified the relationship between the t_f and SDAS defined by (3-2). In this study, the model regarding the correlation SDAS - t_f as well SDAS- $\Delta\tau^*$ are developed.

A representative cooling curve of the basic alloy, AlSi7Cu3 and its first derivate illustrate the characteristic points determined in this study (Fig. 4-9).

The computer aided cooling curves can be used to determine the AlSi eutectic morphology before and after the addition of modifiers. The net effect of the additions of modifiers on the cooling curve of Al-Si alloys is the depression of the nucleation and growth temperatures of the main eutectic reaction. The depression of ΔT_E has been correlated with the degree of Al-Si eutectic modification. The larger the magnitude of ΔT_E the higher the level of modification.

$$\Delta T_{E,G}^{Al-Si} = T_{E,G, UNMODIFIED}^{Al-Si} - T_{E, G, MODIFIED}^{Al-Si} \quad (4-1)$$

$\Delta T_{E,G}^{Al-Si}$ - Depression of the Al-Si eutectic growth temperature, represents the temperature difference between the unmodified and modified Al-Si eutectic temperature.

$T_{E,G, UNMODIFIED}^{Al-Si}$ - Al Si eutectic unmodified temperature is the maximum temperature that is achieved during the recalescence of the melt from the nucleation temperature without any addition of modifiers.

$T_{E, G, MODIFIED}^{Al-Si}$ - AlSi eutectic modified growth temperature is the maximum temperature after addition of modifiers, usually A one-ten per cent Sr master alloy, that is achieved during nucleation temperature.

The term “modification” describes the condition of refinement of the silicon particles. This parameter has been determined in the experiments where the content of strontium was varied.

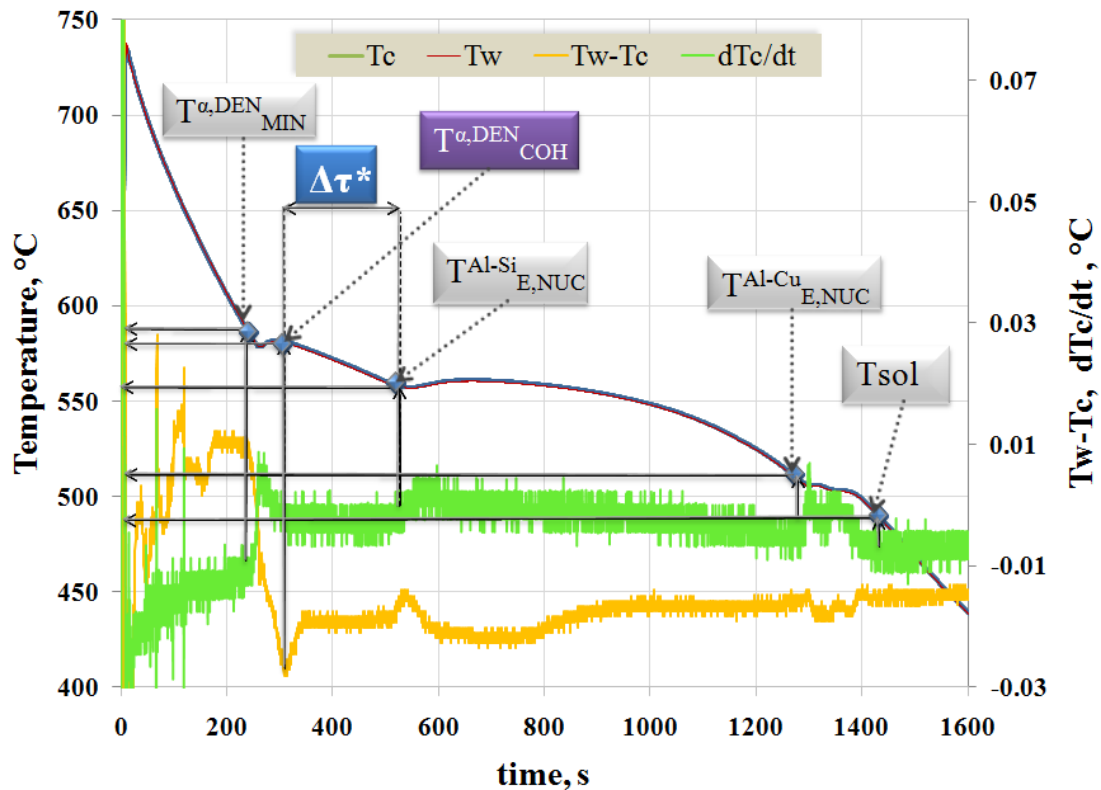


Fig. 4-9 Representative points on the cooling curve of the AlSi7Cu3 alloy

4.3.2. Chemical analysis

Chemical composition variations in the basic Al-Si-Cu alloy concerning changes of major and minor alloying elements content has been monitored and measured by optical emission spectroscopy (OES) technique.

This method capable for rapidly analyzing compositions of metals, is adopted for the analysis of various kinds of alloys in which the content of an element in a test sample to be analyzed is determined in accordance with a calibration curve showing the correlation between the spectral intensity ratio (absolute radiation power of an element / absolute radiation power of the base metal) and the concentration of the element in the standard sample.

In optical emission spectrometry, since the spectral intensity ratio of a sample to be analyzed is incorporated into a previously prepared calibration curve and the content of the element in the sample is determined from this curve, the precision of the analysis for the sample and its accuracy depends on the accuracy of the previously prepared calibration curve and the

accuracy of the daily drift correction in the calibration curve (fluctuation of the spectral intensity ratio caused by the analyzing device). Accordingly, a standard sample of homogeneous and known element content is necessary for an accurate analysis. In addition, as the standard sample used for such optical emission spectrometry, a disc-like ingot of 40 to 60 mm diameter and 5 to 10 mm thickness prepared by casting a molten metal into a die is used as a standard sample after determining a standard composition value thereof by chemical analysis. Upon optical emission spectrometry, the surface of this standard sample is machined into a smooth surface and then a calibration curve is drawn based on the spectral intensity ratio caused by sparking predetermined positions in the surface.

The chemical analysis of the resulting samples was performed according to Standard Test Method for Optical Emission Spectrometric Analysis of Aluminum and Aluminum Alloys by the Argon Atmosphere, Point-to-Plane, Unipolar Self-Initiating Capacitor Discharge.

The elements covered in the scope of this method are listed as the following: Ag, Al, As, B, Bi, C, Ca, Ce, Co, Cr, Cu, Fe, Mg, Mn, Mo, N, Nb, Ni, P, Pb, S, Sb, Si, Sn, Te, Ti, V, W, Zn, Zr. The concentration ranges given in the above scope were established through cooperative testing (ILS) of selected reference materials. The range shown for each element does not demonstrate the actual usable analytical range for that element. The usable analytical range may be extended higher or lower based on individual instrument capability, spectral characteristics of the specific element wavelength being used and the availability of appropriate reference materials.

The optical emission spectrometer was used for analysis of solid samples with minimal diameter 12 mm and minimal thickness 0.5 mm. with incorporated argon flushed spark stand and high performance spark source is designed for accurate quantitative analysis of low and high alloyed alloys, analysis up to 32 elements. In this equipment the detection limit amounts $>0.0002\%$.

Samples were taken from the solid TA samples that were previously cut into two halves. One half has been used for the chemical analysis and another half for metallographical analysis. The sample was surface cleaned by milling machine without cutting fluid.

4.3.3. Metallographic analysis

4.3.3.1. Light optical microscopy (LOM) and Image analysis

The sample preparation

The metallographic samples were prepared using standard metallographic procedure that includes cutting, mounting, grinding and polishing. The metallographic samples taken from real casting-cylinder heads were small cubic samples (1.5 x 1.5 x 1.5 cm) and because of their dimension, it was necessary to mount them inside a polymer block. For that purpose cold mounting method has been used where two components mixture, polymer powder and liquid binder were prepared (2 portion of polymer powder in proportion to 1 portion of liquid binder). The sample was placed into the plastic cylinder mold and the mixture poured in and allowed to set. Cold mounting takes about 40 minutes to complete. The conical TA samples solidified in the ceramic mold were not mounted.

After that grinding has been done using rotating discs covered with silicon carbide paper in the presence of water. The application of light pressure at the centre of the sample provided grinding of sample without the formation of grinding edges and planes. There are a number of grades of paper, with 180, 320, 600, 1000, grains of silicon carbide per square mm. After the final grinding operation on 1000 paper, the samples were washed in water followed by alcohol and dry it before moving to the polishers. The polishers consist of rotating discs covered with soft cloth impregnated with diamond particles (3 and 1 micron size) and an oily lubricant. The polishing begun with the 3 micron grade and continued until the grinding scratches have been completely removed till the sample surface becomes mirror like reflective.

Determination of SDAS

Microstructural changes were examined and quantified using light optical microscope NIKON Epiphot 200 in conjunction with the image analyser software NisElements Br 2.0 The linear interception method was applied to measure the secondary dendrite arm spacing (SDAS). Based on the linear interception method, the SDAS was determined as a ratio of length segment to the number of arms (See Fig 4-10).

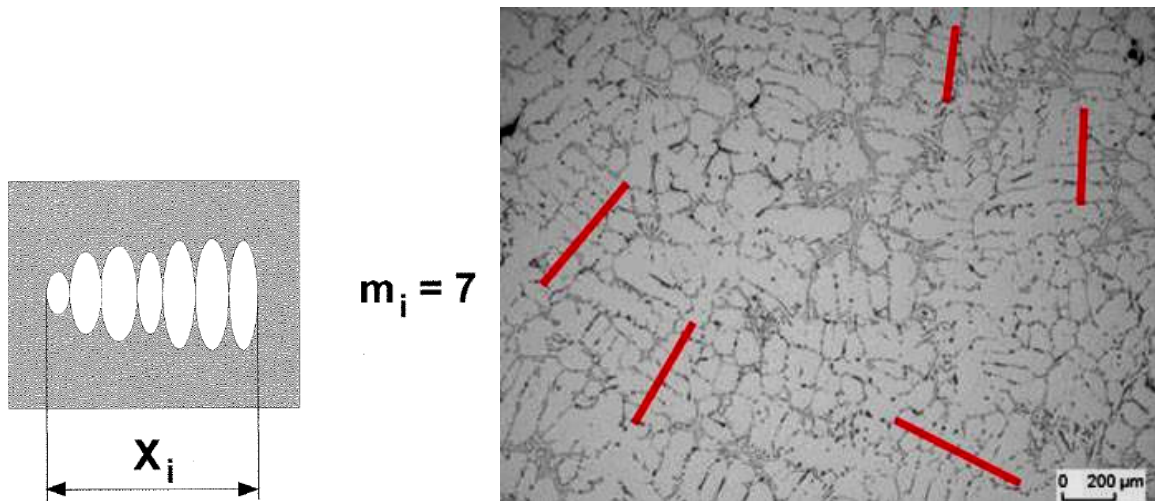


Fig. 4-10 Linear interception method

It is necessary to emphasize that metallographic sample from cylinder head was sectioned to the area of combustion chamber surface where the measurements of SDAS has been done at the distance of 3 mm from the surface and the SDAS in laboratory specimens cast in the permanent metal mold and the ceramic mold has been determined in the area close to the tip of the central thermocouple.

According to the previously mentioned procedure, SDAS measurement has been performed using only dendrites which possess minimal 5 dendrite arms. In order to determine the average value of SDAS in one sample, it was necessary to carry out minimal 10 measurements or in other words to choose 10 different primary dendrites containing more than 5 secondary arms. As a criterion for the right choice of the dendrites is deviation of median of average values and average value of SDAS and variance of average value. The value of deviation would be maximal $0.5 \mu\text{m}$ and the value of variance minimal $9 \mu\text{m}^2$.

The terms relevant for the evaluation of SDAS are denoted in Table 4-2.

Determination of Cu Phases in AlSiCu samples

The samples with dimensions (20mm x 20mm) and varying Sr content were analysed in order to estimate the total area fraction of Cu phase (seen mainly as fine pockets of (Al+Al₂Cu) eutectic and the blocky Al₂Cu phase). For that purpose a semi-automatic image analysis operation sequence in image analyser software was designed, which allowed one to

keep the human operator influence at a minimum. In each sample, 150-200 objects were identified in the frame with the area of $42.3 \times 10^3 \mu\text{m}^2$ using magnification of 100X. The percentage area of Cu phase was measured in each field. From these readings, the average area fraction of Cu phase was determined for each content of strontium.

Table 4-2 Terms relevant for evaluation of SDAS

Determination of SDAS in as-cast samples	
minimal number of measurements	$n \geq 10$
index of the measured dendrites	$i = \{1, 2, \dots, n\}$
minimal number of dendrites arms	$m_i \geq 5$
the length of i-te dendrites	x_i
the average value of <i>i</i> dendrites	$\overline{x_{SDAS\ i}} = \frac{x_i}{m_i}$
the average value of all measurements of SDAS	$\overline{x} = \frac{1}{n} \cdot \sum_{i=1}^n \overline{x_{SDAS\ i}} = \frac{1}{n} \cdot \sum_{i=1}^n \frac{x_i}{m_i}$
estimated variance of average value of SDAS	$s_{\overline{x_{SDAS}}}^2 = \frac{1}{n-1} \cdot \sum_{i=1}^n (\overline{x_{SDAS\ i}} - \overline{x_{SDAS}})^2 \geq 9 \mu\text{m}^2$
Median of average value of SDAS	$\overline{x_{SDAS}} = \begin{cases} \overline{x_{SDAS(k/2)}}, & k/2 \notin IN \\ \frac{\overline{x_{SDAS(k/2)}} + \overline{x_{SDAS(k/2+1)}}}{2}, & k/2 \in IN \end{cases}$
With $\overline{x_{SDAS}} - \overline{x_{SDAS}} \leq 0.5 \mu\text{m}$	

4.3.3.2. Scanning electron microscopy-Energy Dispersive X-ray (SEM-EDX) analysis

Additionally Scanning Electron Microscopy (SEM) observation, combined with an energy dispersive X-ray analyzer (EDX) was performed to identify the morphology and stoichiometry of the present intermetallic phases with special emphasis of the Cu enriched phases in the basic AlSiCu alloy. For this purpose SEM-EDX model Joel JSM 5410 was used (Fig 4-11).



Fig. 4-11 Scanning Electron Microscope JEOL JSM 5410

The main features/technical data of the JEOL JSM 5410 model used in this work are as follows:

Electron gun: Tungsten-Filament

Accelerating Voltage: 0.5 - 30 kV

Resolution: 4 nm bei 30 kV (the resolution used in this work was 20 kV)

Magnification: 15 x...200 000 x

SE-Detector (Secondary Electron)

BE-Detector (Backscatter Electron), Compo-, Topo-Mode

EDX-Detector EDAX

Multi-element X-ray mapping and line scans

Five-angular plots

Image Analyser Software: Edax Genius

4.3.4. Sub- μ Computer Tomography (Sub- μ CT)

In conventional radiography, X-rays pass through the investigated object and the transmitted intensity is recorded as a two-dimensional image. The attenuation of the x-ray by interacting with the material is the fundamental parameter and the actual measured value of this method. If the sample is imaged several times in different orientations, three-dimensional volume information on the sample structure can be obtained by using computer algorithms. The result is a volume image where the single elements (voxel) represent the local absorption respectively the attenuation coefficients. So the density allocation is seen but not colour or reflection variations.

“Tomos” is the Greek word for “cut” or “section” and “graphy” the word for “writing something”, so that tomography describes a technique for digitally cutting an object using X-rays to reveal its interior details. A computer tomography image is typically built on slices, like slices of bread. This analogy is suitable because just as a slice of bread has a thickness, a computer tomography slice corresponds to a certain thickness of the object being scanned. Therefore whereas a typical digital image is composed of pixels (picture elements), a computer tomography image is composed of voxels (volume elements). Principle of the computer tomography is shown in Fig. 4-12

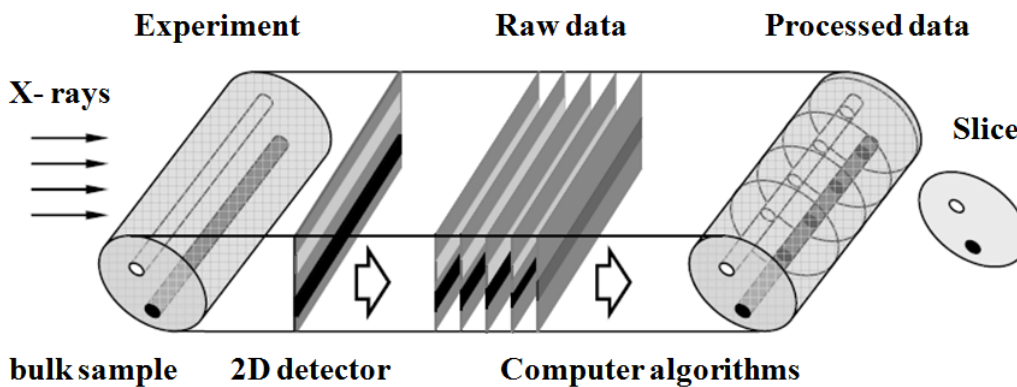


Fig. 4-12 Principle of computer tomography (CT)

In order to get 3-D overview of the microstructure in the basic AlSiCu alloy and 3-D distribution of phases present in the structure, the Sub- μ Computer Tomography method has been applied and the analysis were carried out at Fraunhofer Entwicklungszentrum für

Röntgentechnik (EZRT), Fürth. The Sub- μ Computer Tomography Equipment is shown on Fig. 4-13.

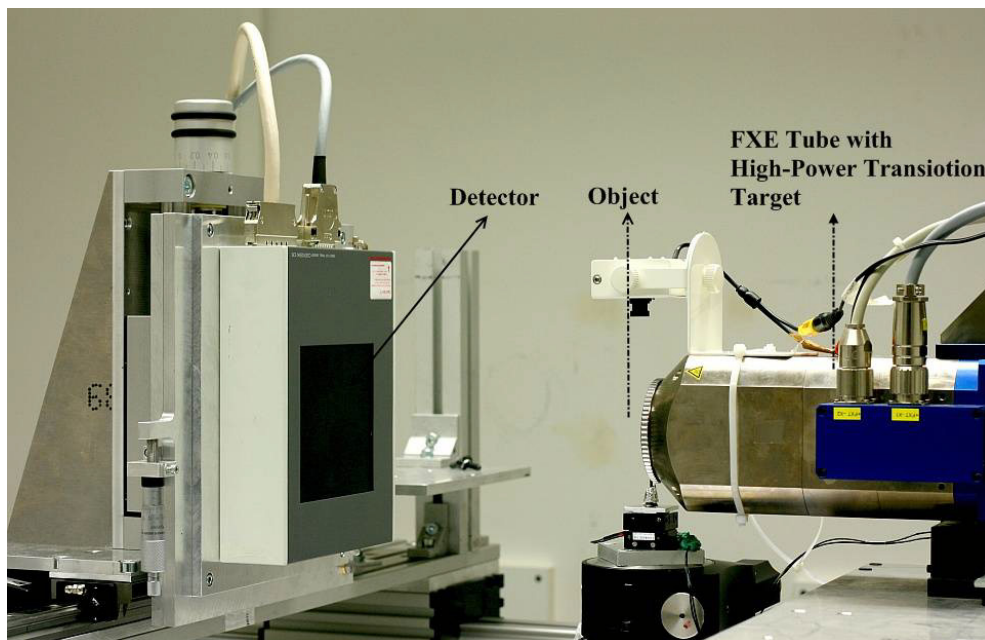


Fig. 4-13 Sub- μ CT -System at the Institute Fraunhofer EZRT, Fürth

For CT measurements an X-ray tube with a minimal focal spot size of $2\ \mu\text{m}$, the finefocus FXT 160 has been used. The tube had a transmission target with $6\ \mu\text{m}$ of tungsten on a $350\ \mu\text{m}$ diamond layer and could be operated between $20\ \text{kV}$ and $160\ \text{kV}$ with a maximum target power of $15\ \text{W}$.

The projections were taken with the indirect converting CsI scintillation detectors Hamamatsu C9311DK (1024×1024 pixels, $100\ \mu\text{m}$ pixel pitch) and Perkin Elmer RID 512 (512×512 pixels, $400\ \mu\text{m}$ pixel pitch) and a direct converting semiconductor detector Ajat DIC 100TL (1024×252 pixels, $100\ \mu\text{m}$ pixel pitch) respectively.

The manipulation system for source and detector consists of a translation axis from Physics Instruments. For positioning the specimen in x and y direction and rotating it with a wobble under $15\ \mu\text{rad}$, a Micos setup was used. The whole setup was mounted on an air cushioned table for uncoupling from unintentional vibrations. Furthermore the measurement cabin was air conditioned to avoid deformations caused by temperature variation.

The maximum achievable resolution of a CT- System is basically limited by the size and stability of the focal spot. Other factors are the accuracy and stability of the manipulation system and the material and size of the test object, which determines the contrast.

The voxel size of the reconstructed 3D-volume data set is predetermined by the magnification given by the geometrical setup during the CT (Fig 4-14).

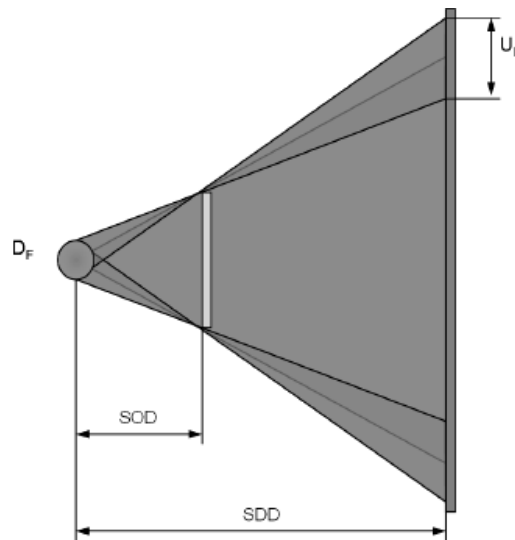


Fig. 4-14 Edge blurring by limited focal spot size

The limitation of the useful magnification is given by the focal spot size, the pixel size and distance of the detector limited by the intensity of the X-ray tube. Maximum useful magnification is given if blurring from the focal spot diameter UF is of the pixel size of the detector.

The imaged aberration size depends on the geometrical magnification M described by the quotient of projected structure size to real structure size or:

$$M = \frac{\text{Source - Detector - Distance (SDD)}}{\text{Source - Object - Distance (SOD)}} \quad (4-1)$$

The application of Digital Detector Arrays (DDA) with pixel sizes of over 100 microns requires an increase of the applied magnification. The evaluation method is based on the projection of an object with a well known diameter to determine the magnification.

The detector and object manipulator were positioned in the beam path and aligned with the proprietary developed multi sphere alignment tool (MuSAT). The tool takes 36 images of a rotating sample and can calculate the tilt, skew and rotation angles of the detector by a fit on the projection data.

Before every CT the object rotation axis was roughly adjusted using a fine wire and rotating it on different positions. From this procedure also the geometrical resolution was evaluated and provided to the algorithm of reconstruction.

4.3.5. Simulation method

The possibility to simulate the microstructure characteristics and mechanical properties of the aluminium cast components with a wide variety of shapes and complexity enable the engineers to use the property variation obtained in Al-castings and thereby be able to make good progress in e.g. weight optimization issues. The mechanical properties of cast aluminium alloys are very sensitive to composition, casting process, which encounters mold filling and solidification behaviour, and post-processing such as thermal treatment. The coarseness of the microstructure and the type of intermetallic compounds that are formed and precipitate during solidification are fundamental to the material behaviour.

The simulation of the casting processes and the resulting microstructure and mechanical properties permits a reduction of experimental testing and providing good solution of process and material selections, thereby making the design and development process more cost efficient.

This contribution will illustrate the facilities and opportunities that cast simulation of solidification behaviour and the resulting microstructure in terms of Secondary Dendrite Arm Spacing, SDAS of the selected chemical composition and a component may deliver.

The SDAS is described as a function of local solidification time, depicting the fineness of the microstructure constituents where t_f is the total solidification time, and C and n are constants which are related to the material.

On the other side, a computer simulation of the whole process is a convenient way of design of mold and analysing the effect of various parameters. For that reason, it is useful to simulate the SDAS values in the whole volume of casting obtained in the metal mold. The Simtec/WinCast simulation Software based on the Finite Element Method, made by German company, RWP, is used in this work (Fig. 4-15). The experimental and calculated values of SDAS in the samples solidified in the permanent metal mold have been compared.

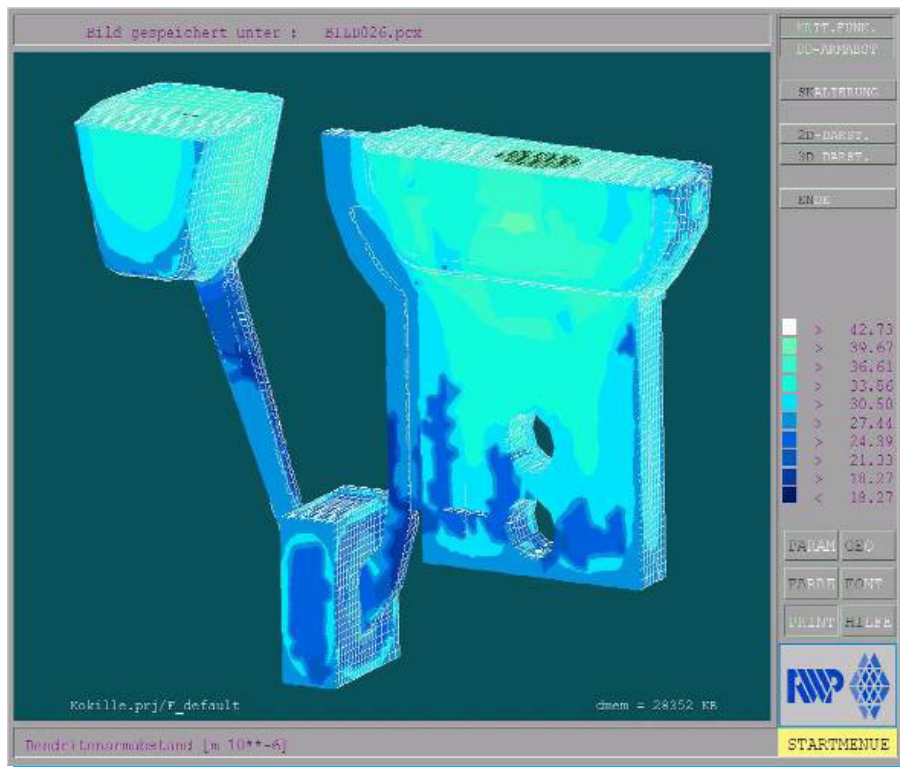


Fig. 4-15 The simulation of solidification process of AlSi7Cu3 alloy in the permanent metal mold using Simtec/WinCast software

Comparing the calculated and experimental values of SDAS, the mathematical model used incorporated in the simulation software has been finally evaluated.

5. Results and discussions

5.1. Microstructure characterization of the basic AlSi7Cu3 alloy-LOM, SEM-EDX and CT results

Results of chemical analysis of the basic alloy sample taken from the cylinder head indicated that actual chemical composition was in good agreement with the standard chemical composition (see Table 4-2 in Chapter 4.). The actual chemical composition of AlSi7Cu3 sample was as following: 7.41 wt% Si, 0.36 wt% Fe, 3.06 wt% Cu, 0.32 wt% Mn, 0.26 wt% Mg, 0.041 wt% Cr, 0.016 wt% Ni, 0.0198 wt% Zn, 0.0278 wt% Pb, 0.0075 wt% Sn, 0.145 wt% Ti, 0.11 wt % Sr, 88.30 wt% Al.

Microstructural characterization was performed using light optical microscopy (LOM), scanning electron microscopy with energy dispersive x-ray spectroscopy (SEM-EDS) and sub- μm computer tomography (sub- μm CT). The sampling procedure has been already described in the chapter 4.

In Fig. 5-1 the microstructure of the basic alloy is shown under the magnification 50 X and in smaller segment under higher magnification, 200 X.

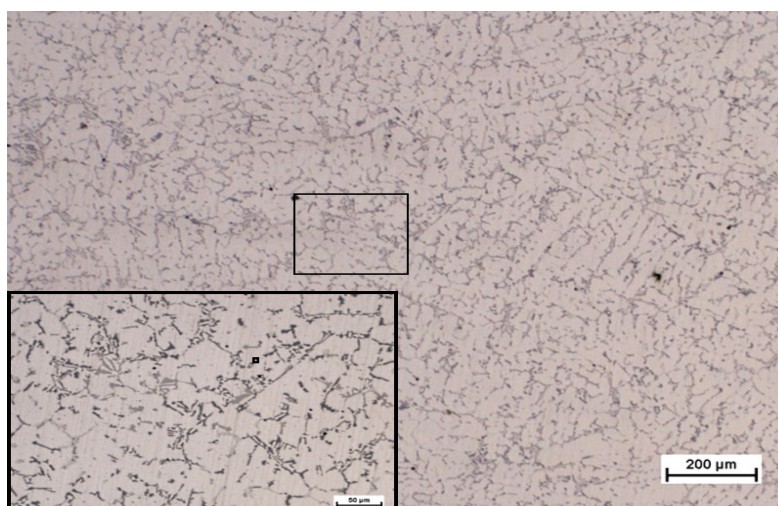


Fig. 5-1 Light optical microphotograph of the basic alloy, AlSi7Cu3

It is noticeable in Fig. 5-1, that microstructure of AlSi7Cu3 alloy sample consisted of the α -aluminum primary phase in the dendritic form, while the interdendritic space was filled by the primary Al-Si eutectic phase and the intermetallic phases. Phase identification is often non-trivial in multicomponent Al-Si casting alloys due to the many complex intermetallic phases that form.

The morphology of the phases in AlSi7Cu3 sample were examined using SEM. Chemical composition of the intermetallics was made by EDS attached to the SEM. The obtained SEM microphotograph including the fields of analysed phases can be seen in Fig. 5-2.

According to the Bäckerüd [34] the solidification reactions and the phases that can be expected in the basic AlSi7Cu3 alloy are denoted in the Table 5-1.

Table 5-1 Reaction during the solidification of AlSi7Cu3 alloy [34]

Rection Nr.	Reactions	Reaction temperature, °C
1.	Development of dendritic network	580-610
2.	$L \rightarrow Al + Al_{15}Mn_2Si_2$	590
3.	$L \rightarrow Al + Al_5FeSi + Al_{15}Mn_2Si_2$	590
4.	$L \rightarrow Al + Si + Al_5FeSi$	575
5.	$L \rightarrow Al + Mg_2Si + Al_8Mg_3FeSi_6$	540
6.	$L \rightarrow Al + Al_2Cu + Si + Al_5FeSi$	525
7.	$L \rightarrow Al + Al_2Cu + Si + Al_5Mg_8Cu_2Si_6$	505-507

The SEM-EDS analysis of AlSi7Cu3 sample revealed besides the trivial phases (primary α -dendrite and Al-Si eutectic) few intermetallic compounds were located in the interdendritic area.

The EDS spectrum of the phases marked in Fig. 5-2 indicated that AlSi7Cu3 alloy contained also the Cu - bearing, Fe- and Mn- bearing phases as well, low melting phase of Pb.

Fig. 5-3 represents EDS Spectrum of the field ‘‘0’’. According to the chemical composition of the spectrum (96 wt% Al, 0.96 wt% Si and 2.84 wt% Cu), the phase field ‘‘0’’ corresponded to the primary α -aluminum phase.

The EDS Spectrum of the field ‘‘1’’ is given in Fig. 5-4. The chemical composition of the spectrum related to the field ‘‘1’’ included: 57.77 wt % Al, 0.68 wt% Si, 0.66 wt% Mn, 1.14 wt% Fe, 22.74 wt% Cu, 16.67 wt% C and 0.65 wt% O. In Fig. 5-4 high Al and Cu K alpha peaks are observed. The first Cu peak overlapped with the Fe peak and in addition one smaller

Fe as well Mn peaks were present. Based on the resulted EDS Spectrum and the morphology of the phase in the field “1”, the observed phase can be specified as Al-Al₂Cu minor eutectic.

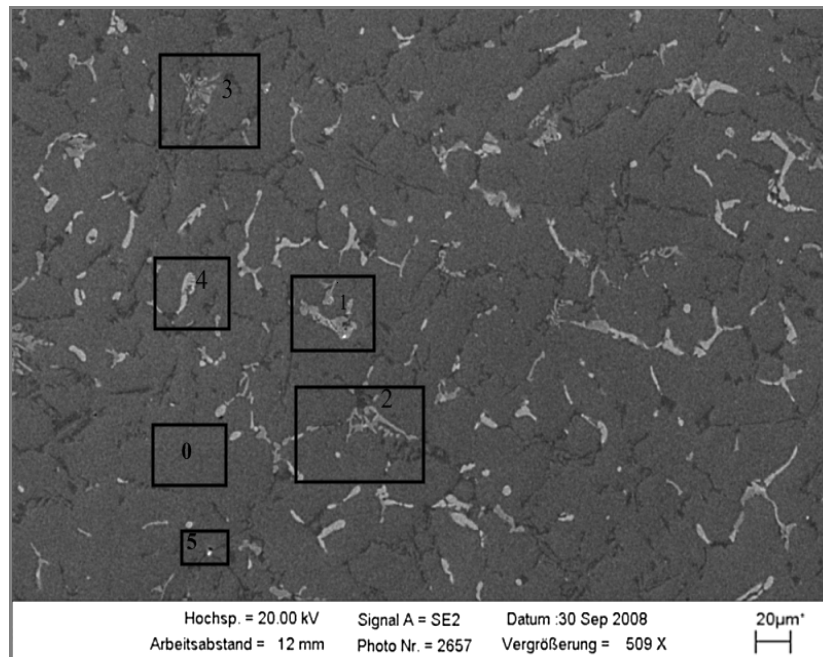


Fig. 5-2 SEM microphotograph of the basic AlSi7Cu3 alloy

As it was reported in the articles of Caceres and Dotty [108, 109], the “massive” or “blocky” Al₂Cu phase (containing approximately 40wt% Cu) formed together with β -Al₅FeSi platelets at approximately 525 °C. At approximately 507°C, a fine Al-Al₂Cu eutectic phase forms (containing approximately 24wt% Cu). If the melt contains more than 0.5wt% Mg, an ultra fine Al₅Mg₈Cu₂Si₆ eutectic phase also forms at this temperature. This phase grows from either of the two previously mentioned Al₂Cu phases. Some minor alloying elements present in this type of aluminum alloy are also able to change the morphology of the Cu enriched phases. It has been shown that an increase in the strontium content of the alloy increases the proportion of the blocky Al₂Cu and ultra fine Al₅Mg₈Cu₂Si₆ Cu phases versus the Al-Al₂Cu phase in the 3XX series of alloys [110].

In Al-Si-Cu alloys besides the intentional additions, transition metals such as Fe, Mn and Cr are always present. Even a small amount of these impurities causes the formation of a new phase component. The exact composition of the alloy and the casting condition will directly influence the selection and volume fraction of intermetallic phases. Fe-bearing constituent phases typically found in 3xxx series alloys include of α -Al₅FeSi. However Mn and Cr can

substitute for Fe and stabilize the formation of so-called Chinese script, π -Al₁₅(Fe,Mn)₃Si or α -Al₁₂(Fe,Cr)₃Si. In addition, experimental studies have demonstrated that the formation of the intermetallic compounds is influenced by the alloy composition. Fe-rich α -phase also identified by formula α -Al₈Fe₂Si was found to have a cubic structure and a compact morphology e.g. polyhedron [107, 111].

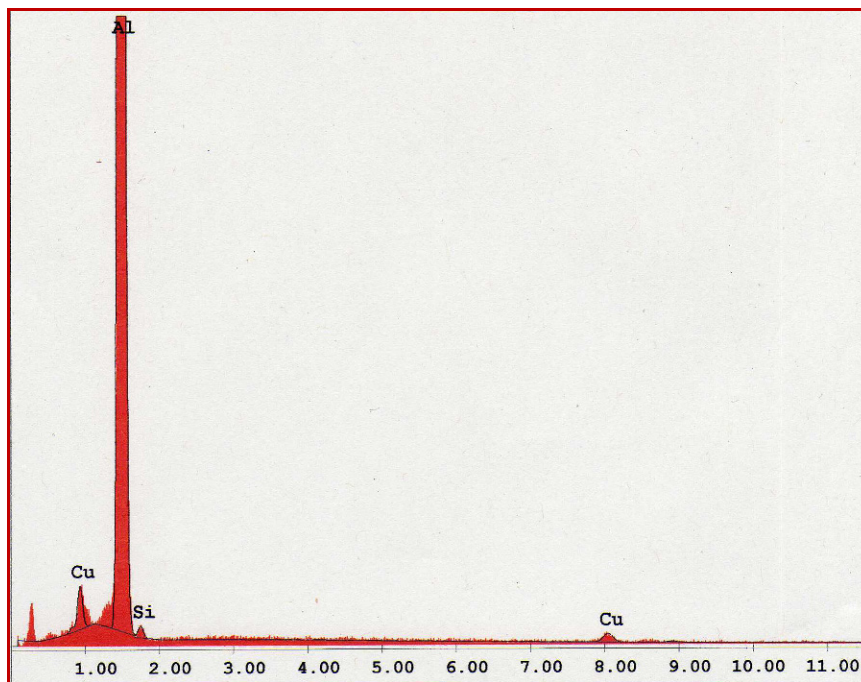


Fig.5-3 EDS Spectrum of the phase field ‘0’ in the basic alloy

Based on the literature data and the spectrum chemistry and the morphology of the shown phases, it was assumed that the field ‘1’ contained the Al-Al₂Cu phase together with the blocky α -Al₈Fe₂Si.

In Fig. 5-5 the EDS spectrum related to the field ‘2’ is shown. The chemical composition of the spectrum (61.22 wt% Al, 22.59 wt% Si, 4.23 wt% Mn, 7.08 wt% Fe, 3.26 wt% Cu, 20.99 wt% C and 0.64 wt% O) and the morphology of the intermetallic phase in the field ‘2’ outlined so-called Chinese script or π -Al₁₅(Fe,Mn)₃Si intermetallic phase.

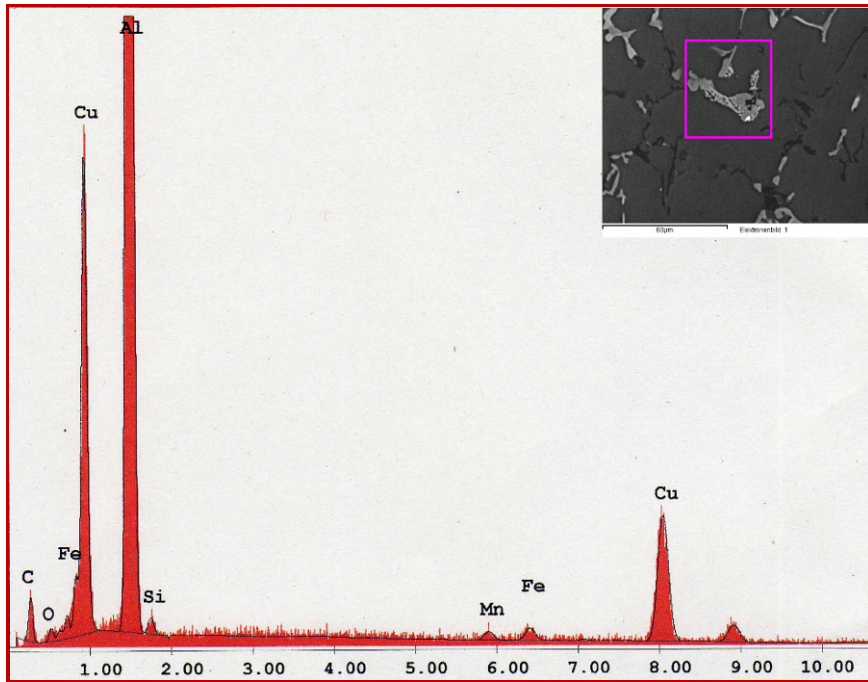


Fig. 5-4 SEM Photograph and EDS Spectrum of the phase field ‘1’ in the basic alloy

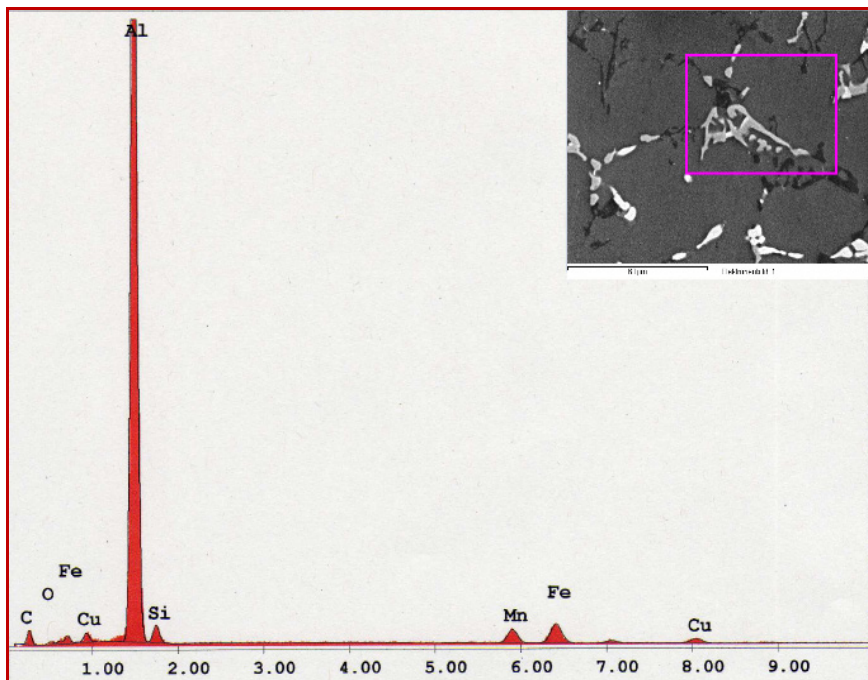


Fig. 5-5 SEM photograph and EDS Spectrum of the phase field ‘2’ in the basic alloy

In the Fig. 5-6 it can be observed the SEM microphotograph and EDS spectrum of the field ‘3’. The morphology of the shown phase seemed similar to the morphology of the previous

Fe- and Mn- bearing (Chinese script) phase. Otherwise, the EDS spectrum of the field ‘‘3’’ contained beside the high peaks of Fe and Mn one small peak of Cr. As it was reported previously [111], Mn and Cr can substitute for Fe and stabilize the formation of so-called Chinese script, π - $\text{Al}_{15}(\text{Fe},\text{Mn})_3\text{Si}$ where the Mn is in part substituted for Cr, therefore the stoichiometry of the phase could be written also as α - $\text{Al}_{15}(\text{Fe}, \text{Cr})_3\text{Si}$.

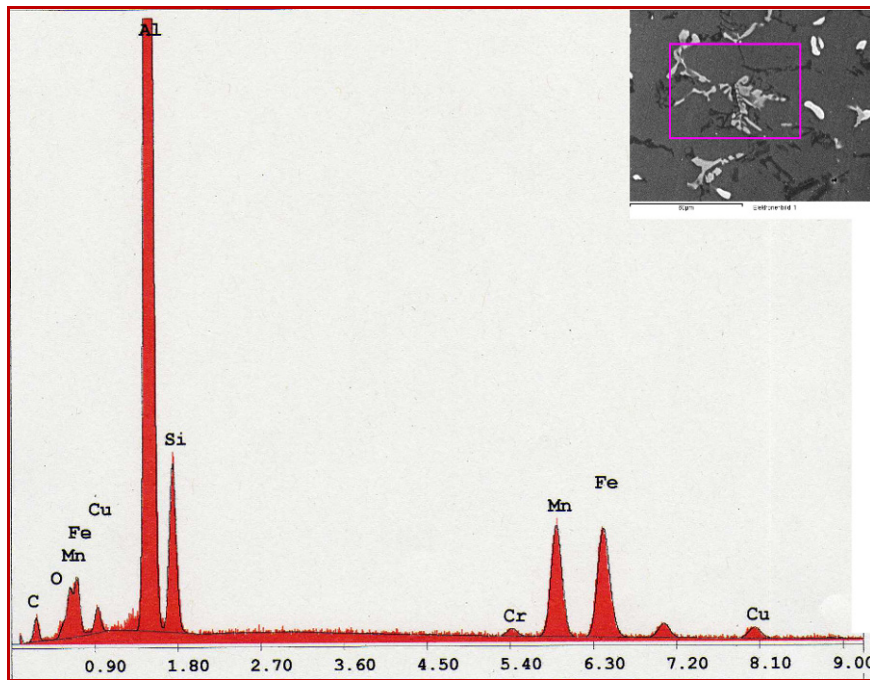


Fig. 5-6 SEM photograph and EDS Spectrum of the phase field ‘‘3’’ in the basic alloy

In Fig. 5-7 it can be observed the spectrum containing two Cu peaks (one high and one lower) and one high peak of Al. The quantitative analysis of this spectrum (44.4 wt% Al, 0.58 wt% Si, 41.45 wt% Cu, 12.74 wt% C and 0.74 wt% O) and the phase morphology pointed out the presence of Al_2Cu phase in the field ‘‘4’’.

The SEM microphotograph and spectrum of the field ‘‘5’’ related to the brightest inclusion observed in the microstructure of the basic alloy is given in Fig. 5-8. This bright inclusion was noticed in the whole sample showing a more or less homogenous distribution. It was also noticed that this bright inclusions precipitated within the light grey network of Al_2Cu .

Based on the chemical composition of the spectrum (42.52 wt% Al, 0.27 wt% Si, 17.85 wt% Cu, 0.19 wt% Fe, 0.17 wt% Mn, 21.81 w% Pb, 16.21 wt% C, 0.48 wt% O) where two Pb peaks were present, the brightest inclusion was identified as Pb inclusion. The slight peaks of Mn, Fe, C, O present in all spectrums were considered in this case as impurities peaks.

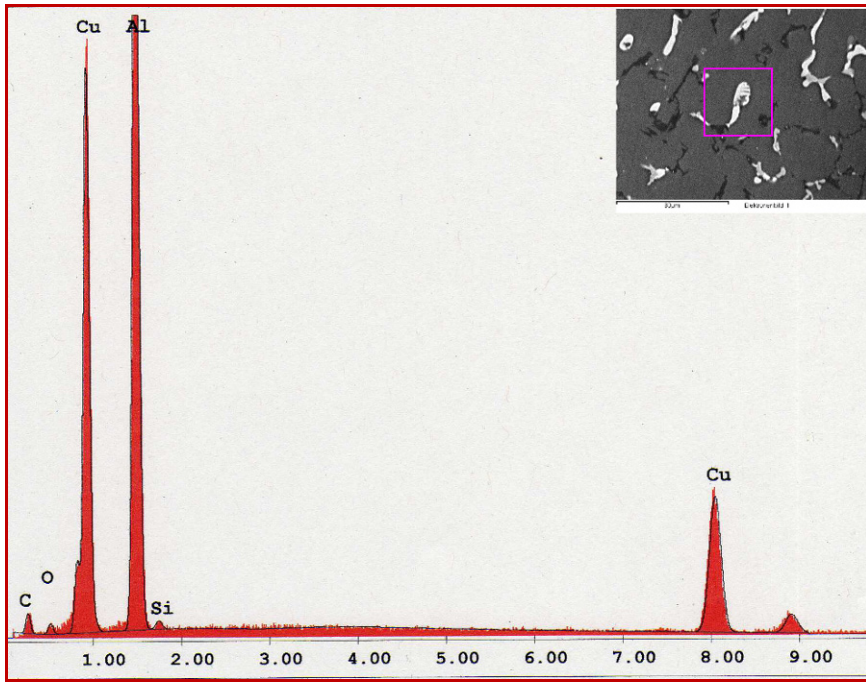


Fig. 5-7 SEM photograph and EDS Spectrum of the phase field '4' in the basic alloy

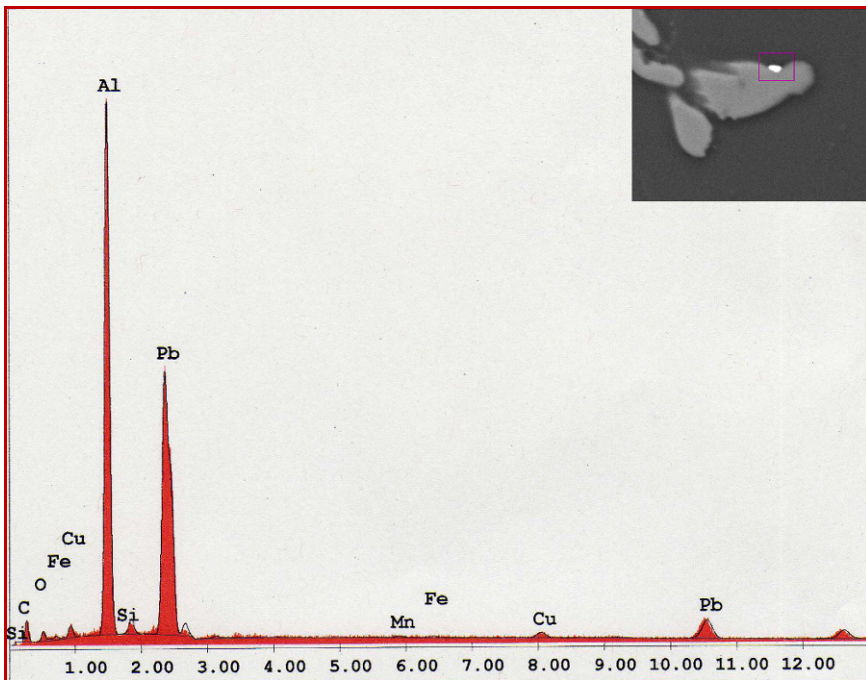


Fig. 5- 8 SEM photograph and EDS Spectrum of the phase field '5' in the basic alloy

Characterization of the sample Al-Si-Cu using the Sub- μ CT method

The method of Sub- μ CT was an attempt to observe 3D the microstructure of the basic AlSi7Cu3 alloy. The sample for the Sub- μ CT analysis has been taken from the central part of the sample which previously was analysed by the LOM and SEM-EDS methods. In that way the surface analysed under LOM and SEM has been as well as observed using CT method and it was specified as ‘0’ slice. The Fig. 5-9 illustrates the CT sample, which was significantly smaller than the samples for LOM and SEM analysis, with the diameter of 1.5 mm and the length about 10 mm. In the Fig. 5-9 beside the CT sample, a 3D rendition and 2D reconstruction of the ‘0’ slice representing the surface of CT sample can be seen.

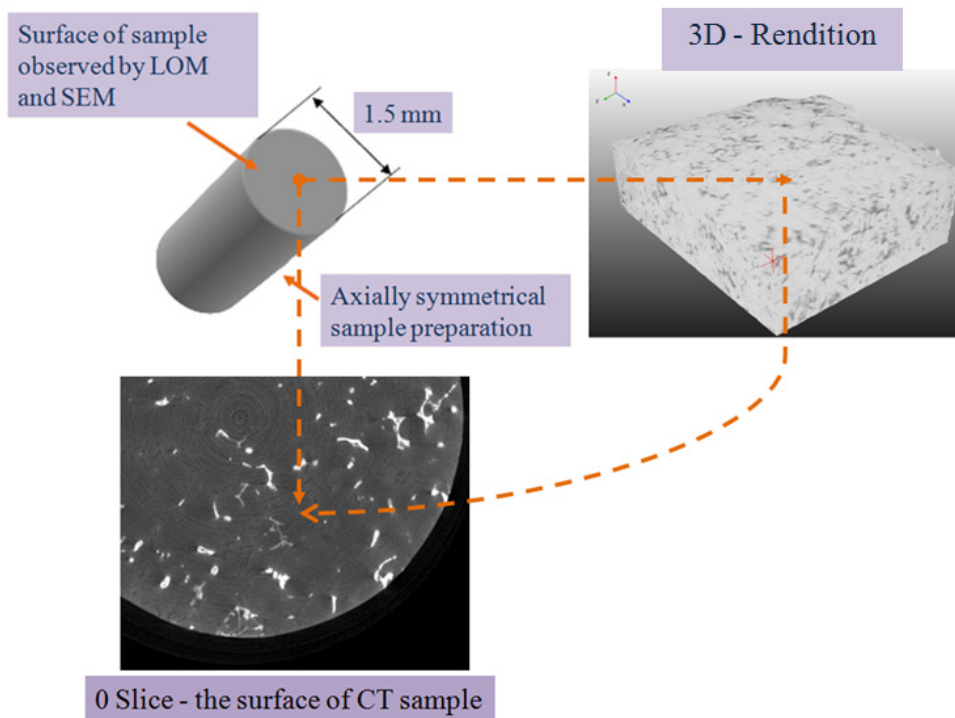


Fig. 5-9 CT sample and 3D Rendition with the 2D Reconstruction of the Slice ‘0’

The 2D Reconstruction of the surface ‘0’ slice demonstrates the microstructure that can be compared with the SEM results of the same sample. In other words, some phases identified by SEM analysis can be also detected by Sub- μ CT method. However, the reproduction of CT results was affected by the difference of material specific adsorption coefficient and spatial- and contrast resolution of the phases present in the sample. The adsorption coefficient difference of the main alloying elements of AlSi7Cu3 alloy is demonstrated in Fig.5-10.

The Fig 5-10 reveals that slight but sufficient difference between the adsorption coefficients of Cu and Fe existed to distinguish the Fe- and Cu-bearing phases not only based on the phase form but also the phase contrast. On the other side, minor difference between the Al and Si adsorption coefficients disabled to make a difference between the aluminum matrix and eutectic Si regarding the lower resolution achieved by CT method.

Up to now, the distinction between materials of only slightly different absorption coefficient is an unsolved problem for submicron CT method. Nevertheless, the CT method provides the information of the spatial distribution of the structure entities present in material. Taking into account disadvantages of the submicron CT method it should be underlined that the CT method is rather a supplementary than main characterization method of the Al-Si alloys.

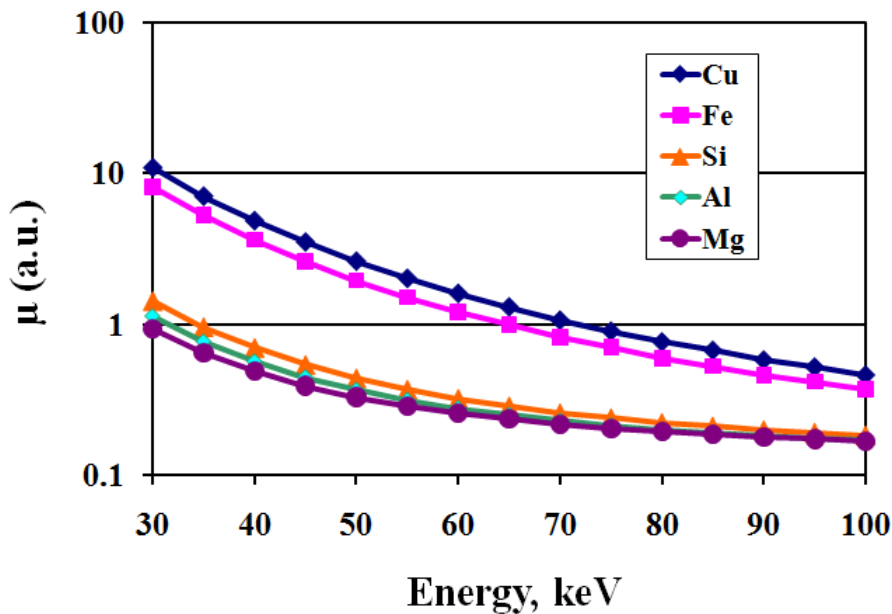


Fig. 5-10 Absorption coefficients of the main alloying elements in AlSi7Cu3 alloys

5.2. Results of tilt pouring die casting process

5.2.1. Computer aided cooling curves in cylinder head

The results of preliminary experiments of in-situ thermal analysis on the AlSi7Cu3 cylinder head casted by the tilt pouring gravity die casting process can be seen in Fig. 5-11. The procedure of in-situ thermal analysis has been already described in the previous chapter.

The cooling curves recorded in five cylinders showed different solidification rates. As it can be noticed maximal cooling rate (2.76 °C/s) was found in the fifth cylinder, while the cooling rates detected in other cylinders seemed more similar to each other showing lower values of cooling rate. Such result concerning the difference between the cooling rates in the cylinders might be considered as a consequence of the casting process nature. The computer aided cooling curves analysis was complemented with the microstructure analysis of the area close to the tip of thermocouples due to the estimation of the SDAS values in these characteristic positions.

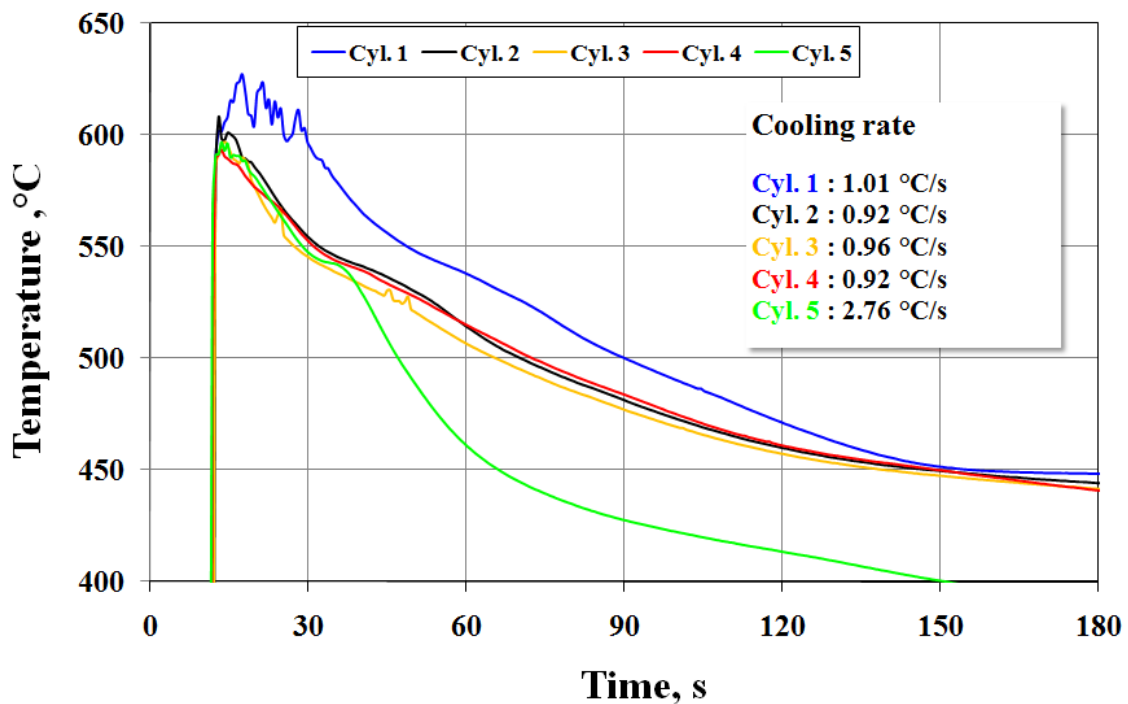


Fig. 5-11 Computer aided cooling curves recorded in cylinder head

5.2.2. Secondary dendrite arm spacing cylinder head

The metallographic sampling procedure and the measurements of SDAS in the metallographic samples taken from the characteristic positions of AlSi7Cu3 cylinder head has been described in the previous chapter of this work. The SDAS has been measured at the distance of 4, 6, 9 and 15 mm from the combustion chamber surface. The measurements of SDAS at 4 mm from the combustion chamber surface have been mandatory performed, because that position was predefined by customers where demand on the SDAS less than 20 μm must be fulfilled. As it can be seen in Fig. 5-12, the SDAS value less than 20 μm could be found only in the fifth

cylinder where the cooling rate was the highest (2.76 °C/s) while, the SDAS values in other cylinders were a bit higher comparing to demand.

Generally, it was expected that SDAS increased with the depth because of the delay in solidification in comparison to the surface. Similar results were reported in the work of Zhang et al [65] who determined also the SDAS values at different distances from combustion chamber surface (from 2- 37 mm) but only in one cylinder. At the distance from 4 to 15 mm form the combustion chamber surface, the SDAS values were changed from 22 to 30 μm . It is worth to mention, in the work of Zhang, the SDAS values estimated only in one cylinder did not provide the information about the casting process nature as well the distribution of SDAS in the whole combustion chamber area.

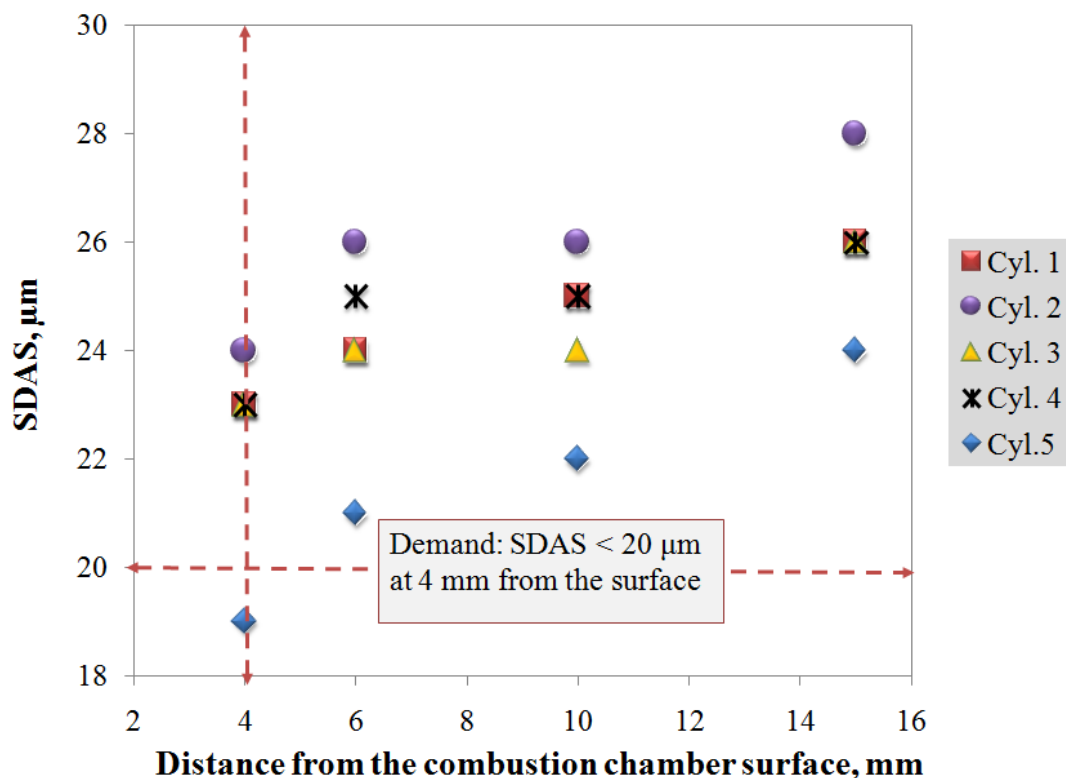


Fig. 5-12 SDAS values in the combustion chamber area of AlSi7Cu3 cylinder head

5.3. Results of laboratory tests in permanent metal mold

5.3.1. The effect of mold temperature and cooling conditions on the SDAS of AlSi7Cu3 alloy

Based on the cooling curves recorded at various mold temperatures and cooling conditions (with and without water cooling of the mold wall) during the solidification of AlSi7Cu3 alloy in the permanent metal mold, the solidification time has been determined. The solidification time, t_f was defined as the time interval between liquidus and solidus temperature. These temperatures were obtained from the first derivatives of the cooling curves. The metallographic samples were taken from the area close to the tip of the first thermocouple where the SDAS was measured at 4 mm from the casting surface (see Fig. 4.8). The recorded cooling curves related to the second thermocouple didn't contain the whole solidification range because the melt was more undercooled showing not the liquidus temperature on the cooling curves detected by the second thermocouples. According to that the metallographic sample was not taken from the area close to the second thermocouple.

The experimental values of SDAS measured close to the tip of the first thermocouple were compared with the calculated SDAS values obtained by simulation of solidification process of AlSi7Cu3 alloys in the permanent metal mold.

Solidification time, the corresponding experimental values of SDAS and the calculated values of SDAS for all experimental conditions are presented in Table 5-2.

Table 5-2 Variation of solidification time and SDAS with respect to mold temperature and cooling conditions

Sample	t_f , s	SDAS(exp), μm	SDAS(calc), μm	ΔSDAS , μm
350NW_1	51.7	25.2	29.0	3.8
350WW_1	43.2	22.2	27.3	5.1
300NW_1	36.8	21.2	25.9	4.7
300WW_1	28	21.4	23.7	2.3
250NW_1	9.8	19.9	16.7	3.2
250WW_1	8.3	19.4	15.8	3.6

*NW = no water cooling; WW = with water cooling

SDAS(exp) = experimental values of SDAS; SDAS(calc) = calculated values of SDAS

ΔSDAS = SDAS(calc) - SDAS(exp), absolute difference of exp. and calc. values

The reduction of mold temperature enabled the decrease of SDAS value. However, it can be noticed that lower values of SDAS were achieved in the presence of water cooling of the mold wall. The effect of mold temperature with and without water cooling on SDAS of AlSi7Cu3 alloy is illustrated in the Fig. 5-13.

The maximum value of SDAS (25.2 μm) was reached in the case of mold temperature of 350 $^{\circ}\text{C}$ without water cooling where solidification time was 51.7 s. The minimal value of SDAS (19.4 μm) was related to the mold temperature of 250 $^{\circ}\text{C}$ with water cooling and solidification time of 8.3 s. It can be added, that without water cooling the change of the mold temperature from 350 to 250 $^{\circ}\text{C}$ led to reduction of SDAS of 5.3 μm . In the presence of water cooling the same decrease of mold temperature provided the reduction of SDAS of 2.8 μm , which indicated that water cooling of the mold diminished the effect of mold temperature on the SDAS although the resulted SDAS values were lowered.

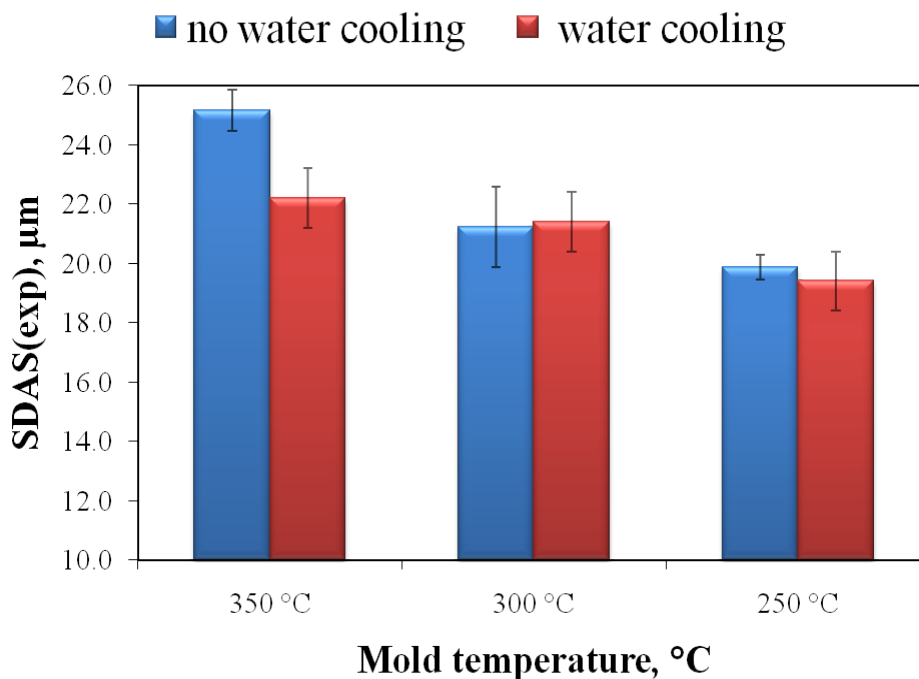


Fig. 5- 13 Variation of SDAS as a function of mold temperature and cooling conditions

The similar trend regarding the SDAS versus mold temperature has been found in the work of B. Zhang et. al [65]. They examined the effect of mold temperature on the SDAS values in the area of combustion chambers surface of Hyundai cylinder head, made of AlSi7Mg0.3. The pouring temperature was kept constant at 720 $^{\circ}\text{C}$. It was found that SDAS value was reduced from 28 μm to about 22 μm as the temperature decreased from 250 $^{\circ}\text{C}$ to about 50 $^{\circ}\text{C}$.

In this study, the solidification process of AlSi7Cu3 alloy under varying mold temperature and cooling condition has been further simulated using a commercial software package WinCast. The predicted solidification time has been then converted to SDAS value via simple empirical relationships between the two that were built into popular codes. In this way, a continuous map of SDAS through the whole casting volume was established according to the correlation between SDAS and t_f described basically by Eq. (3-3). The value of coarsening parameter M was 1.4, while the value of exponent n was $1/3$. The value of coarsening parameter used for simulation in this study should be slightly modified in order to achieve the higher agreement with the experimental data for AlSi7Cu3 alloy.

Fig. 5-14 and Fig. 5-15 present the simulation results and the appropriate microphotographs of AlSi7Cu3 alloy regarding all tested mold temperatures without and in the presence of water cooling of the mold, respectively.

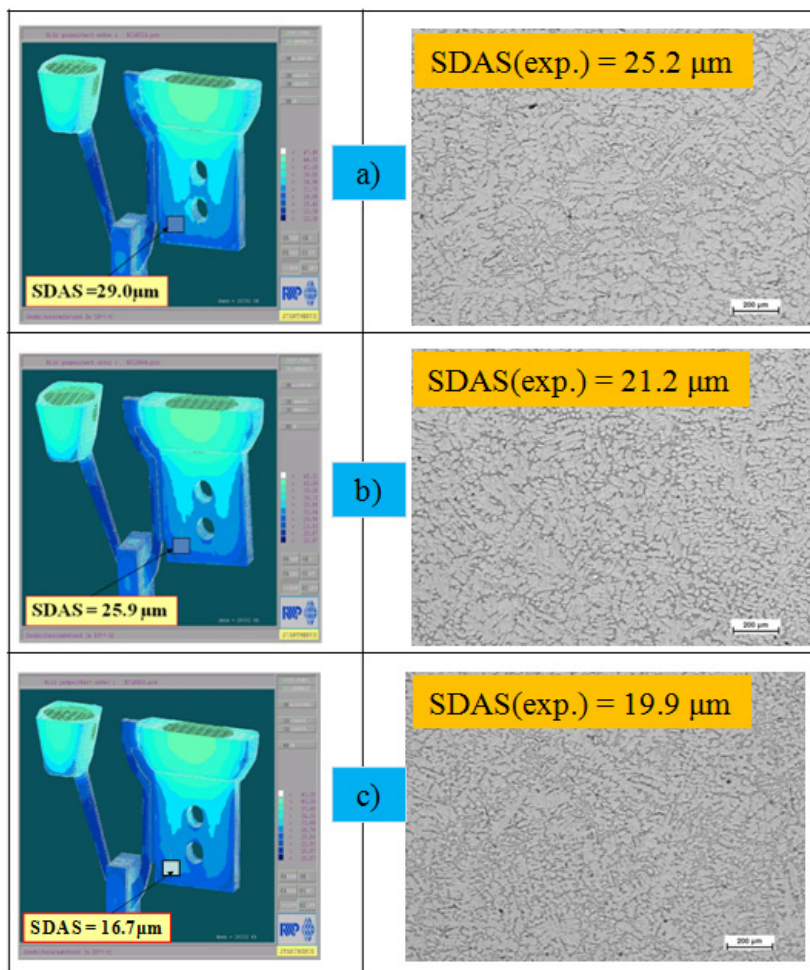


Fig. 5-14 Simulation results and the appropriate microphotograph of AlSi7Cu3 alloys for mold temperatures: a) 350 °C, b) 300 °C and c) 250 °C without water cooling of mold

Comparison between the experimental and simulation results of SDAS is shown in Fig. 5-16. Based on the data regarding the absolute difference between experimental and simulated values of SDAS, Δ SDAS (see Table 5-2) and the graphical interpretation shown in Fig. 5-16 it can be outlined that calculated values of SDAS were higher than experimental values particularly for higher mold temperature (300 and 350 °C). For the lower mold temperature (250 °C) the calculated values of SDAS were lower than experimental.

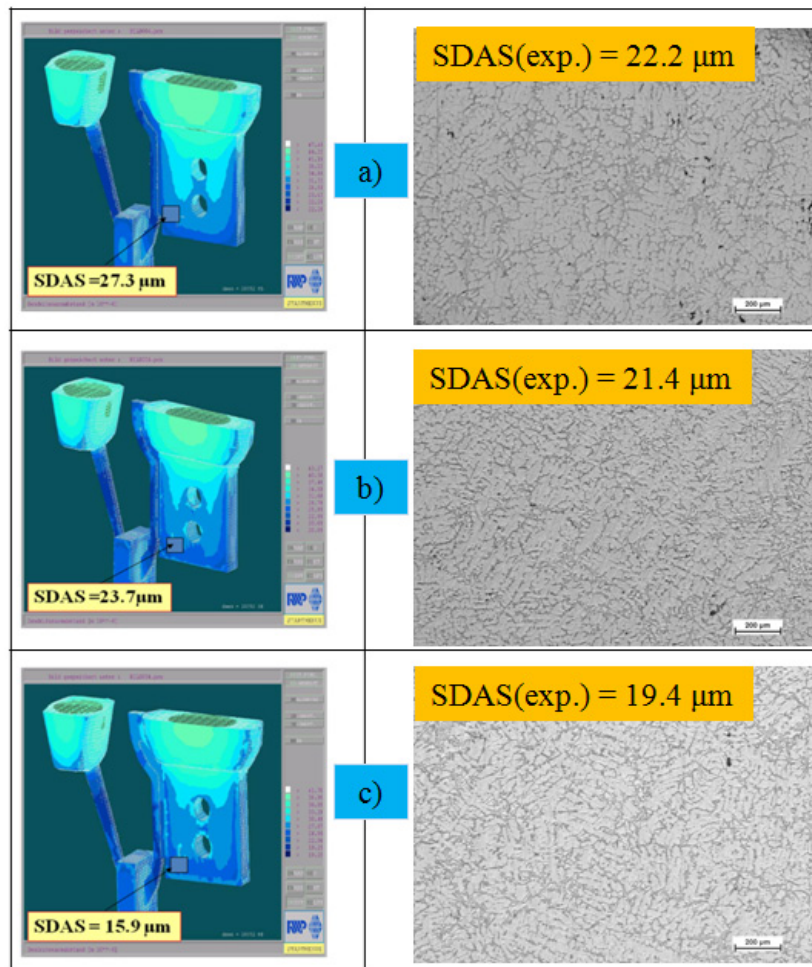


Fig. 5-15 Simulation results and the appropriate microphotograph of AlSi7Cu3 alloys for mold temperatures: a) 350 °C, b) 300 °C and c) 250 °C with water cooling of mold

This could be interpreted in terms of sensitivity of the mathematical model to the mold temperature and cooling conditions variation. As the solidification models could adequately predict SDAS, choices made in setting boundary conditions might affect the quality of the

results. As it was explained by B. McClory et al [112] much of the experimental scatter can be attributed to uncertainty in individual SDAS measurements – considerable uncertainty exists in all quantitative metallography. Small variances may have been caused by errors in matching mesh nodes with measurement locations.

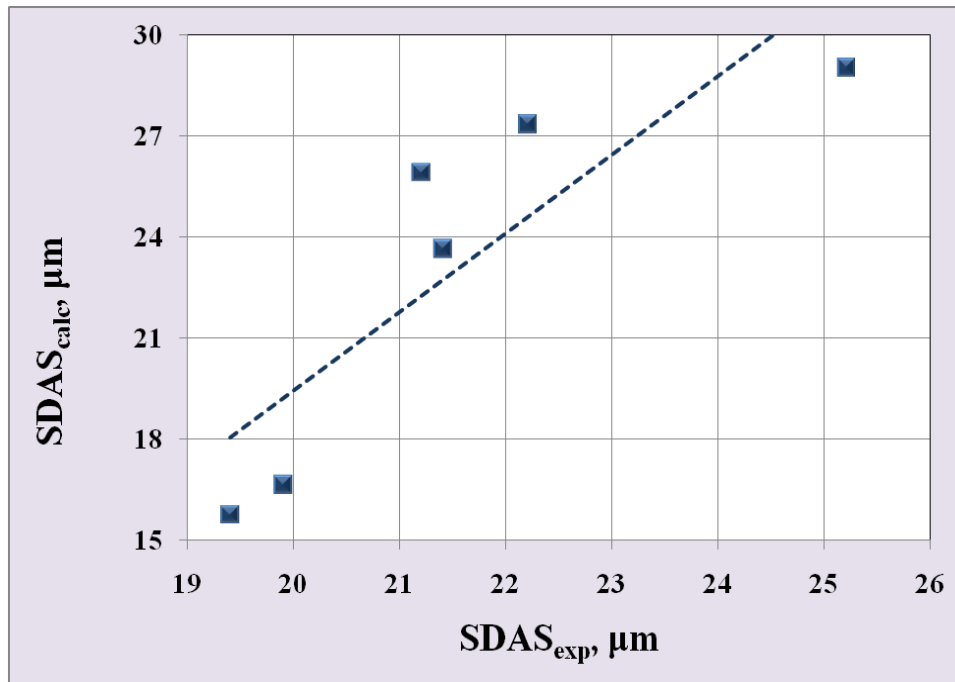


Fig.5-16 Experimental SDAS values versus calculated SDAS values of AlSi7Cu3 alloy solidified in the permanent metal mold

5.4. Results of laboratory tests in ceramic mold - Effect of pouring temperature on SDAS

The second important casting parameter, which effect on the SDAS values of AlSi7Cu3 alloy has been examined among the other was pouring temperature. Dependence of SDAS and the pouring temperature in AlSi7Cu3 alloy including the microphotographs suitable to maximum and minimum examined pouring temperatures are presented in Fig. 5-17. Decrease of the pouring temperature from 750 °C up to 650 °C leads to the decrease of the SDAS about 6 μm. Correlation between the obtained values of the SDAS and the pouring temperature can be described using linear equation (5-1), with relatively high correlation coefficient ($R^2=0.90$).

$$SDAS = 0.07(T_{pour}) + 8.5 \mu\text{m} \quad R^2 = 0.9 \quad (5-1)$$

In order to study the effect of pouring temperature on castings properties, A. Srinivasan et al. has prepared AlSi7Mg0.3 low pressure and gravity castings made for three different pouring temperatures like 720, 740 and 760 °C [113]. It was reported that pouring temperature greatly affects the mechanical properties and microstructure of the low pressure and the gravity cast alloy. Higher pouring temperature led to coarsening of the structure, increased the porosity level and reduced the strength and ductility of alloys. It was also found for the low pressure AlSi7Mg0.3 samples that decrease of the pouring temperature from 760 to 720 °C enabled the decrease of SDAS from 80 to 40 μm.

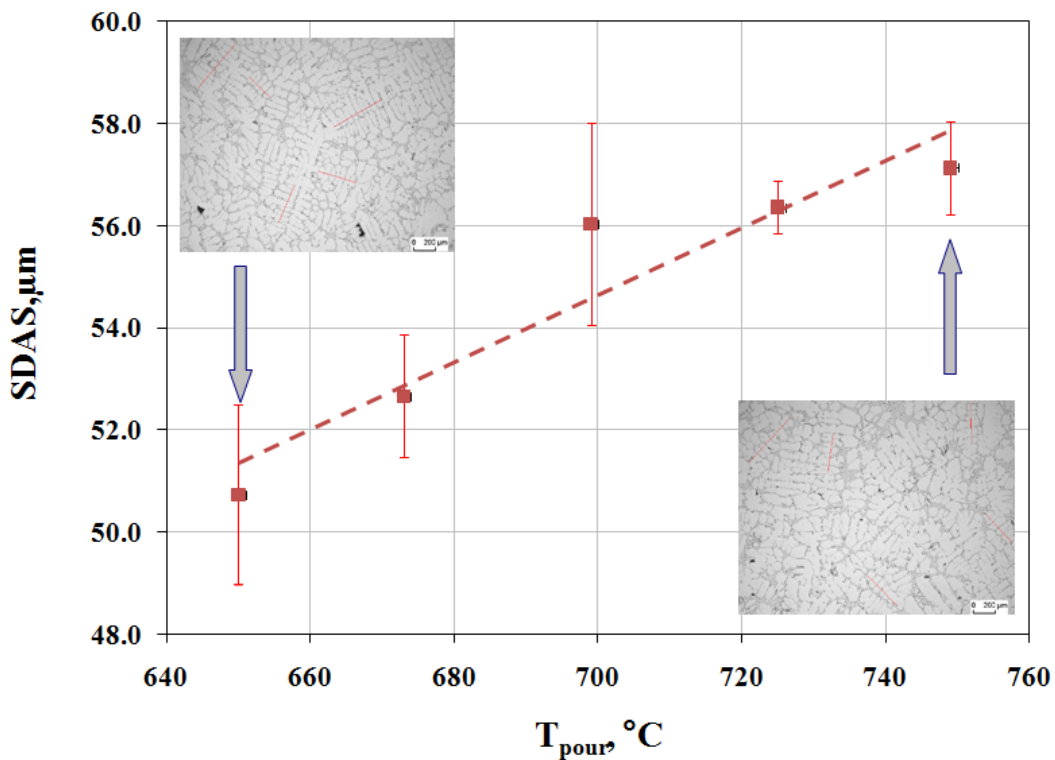


Fig. 5-17 The effect of pouring temperature on SDAS in AlSi7Cu3 alloy

In the work of B. Zhang et al. [65] it was also attempted to reduce pouring temperature, in a range permitted by AlSi7Cu3 alloy specification in order to guarantee the casting quality. The results have shown that the reduction of SDAS was more effective when the pouring temperature was decreased than the decrease of local mold temperature. As the results of Zhang et. al indicated, on reduction of SDAS the decrease of pouring temperature by 20°C

had the same effect as decreasing the mold temperature of 200 °C. Decrease of the pouring temperature from 720 to 690 °C resulted in the lowering the SDAS from 26 to 20 μm.

Although the pouring temperature in this study was varied in the range of 750 to 650 °C and the solidification process took place at the ceramic mold, the same reduction of SDAS in AlSi7Cu3 alloy (about 6 μm) was achieved as in the cited literature.

Such effect of pouring temperature on SDAS might be explained as the following. At higher pouring temperatures the melt superheat could destroy the potential nuclei and reduce the cell numbers. Hence only fewer nuclei are available for the growth, which results in larger grains. Also, more heat has to be removed before the melt starts to solidify and this changes the solidification rate.

5.5. Results of laboratory tests in ceramic crucible- the effect of chemical composition on solidification feature of Al-Si-Cu alloy

Notwithstanding the effect of the cooling rate and/or solidification time governed by the casting processes (sand, permanent mold, die casting etc.) on the solidification features, the parameter such as chemical composition should be also taken into consideration. This fact is very important especially when it is necessary to improve the casting quality but to alter the casting technology as well the casting parameters (pouring temperature, melt treatment, mold temperature, cooling conditions etc.) is not time feasible or acceptable solution by reason of the complex casting geometry. As a matter of fact, the chemical composition variation of the basic alloy might not be neglected in this event.

As it was reported in literature [1, 2, 3, 7, 8, 10], the Al-Si-Cu hypoeutectic alloys commonly used for the cylinder heads casting, contains Si and Cu as major alloying elements. Other alloying elements present relatively in considerable amounts are magnesium, zinc, chromium and manganese and these are considered the minor alloying elements.

The impurities and the alloying elements partly go into solid solution in the matrix and partly form intermetallic compounds during the solidification of the metal. The form and distribution of the phases is controlled by the concentration of the main alloying elements and impurities present. Composition variation within the specification can have a significant effect on the microstructure and, hence, the mechanical properties. Also, the solidification sequence is influenced to a considerable extent by the interaction of the alloying elements like silicon, manganese, copper, zinc and magnesium.

Unfortunately, studies of this nature are not available in literature. The only published work of this type is that of Bäckerud *et al.* [34]. They studied the solidification behaviour of about twelve 380-type alloys, collected from various sources, to elucidate the influence of certain alloying elements on the microstructural development as a part of their research on solidification characteristics of aluminum foundry alloys. The solidification behaviour and structure have been discussed by them for each of the alloys separately. Their results, however, do not compare or conclude the effect of varying the alloying elements, starting with the same base alloy.

One of the aims of this study was to estimate the effect of individual alloying elements on the solidification behaviour and microstructure feature such as SDAS in AlSi7Cu3 hypoeutectic alloy where the variations of chemical composition were ranged within the specification limit of the basic alloy as well secondary alloys containing higher Mg and Zn content.

The alloying elements investigated were silicon, copper, titanium, zinc, magnesium and strontium at the cooling rate of 0.2 ± 0.05 °C/s. This relatively low cooling rate was used in order to provide the dominance of the chemical composition and in that way to clarify the effect of alloying elements variations on the solidification features of Al-Si-Cu alloy.

The experimental procedure related to the effect of chemistry of solidification features of Al-Si-Cu basic alloy has been described in the Chapter 4. As it follows, the focus will be on the results regarding the impact of Si, Cu, Mg, Zn, Ti and Sr on the microstructure feature, SDAS and solidification features such as $T^{\alpha,den}_{nuc}$, $T^{\alpha,den}_{coh}$, $T^{Al-Si}_{E, nuc}$, $T^{Al-Cu}_{E, nuc}$, T_{sol} as function of chemical composition.

5.5.1. The effect of silicon and copper

In order to examine the effect of Si and Cu, six Al-Si-Cu alloys were synthetic produced by melting the charge of Al-7wt% Si and Al-9wt% Si alloys and by adding 1, 2 and 4 wt% Cu to cover the range of Si corresponding to standard basic alloy, AlSi7Cu3 alloy. All other alloying elements were kept approximately constant. No grain refining agent and modifier were added to the melts. The chemical composition of the alloys where the content of Si and Cu were varied is given in Table 5-3.

Table 5-3 Average chemical composition of the synthetic Al-Si alloys containing different Si and Cu content

Si	Fe	Cu			Mn	Mg	Zn	Ti
wt%								
7	0.14	1	2	4	0.01	0.27	0.01	0.09
9								

In Fig. 5-18 the representative cooling curves of Al-Si7 and Al-Si9 alloys containing 1, 2 and 4 Cu wt% as well the corresponding microphotographs of the thermal analysis (TA) samples can be seen.

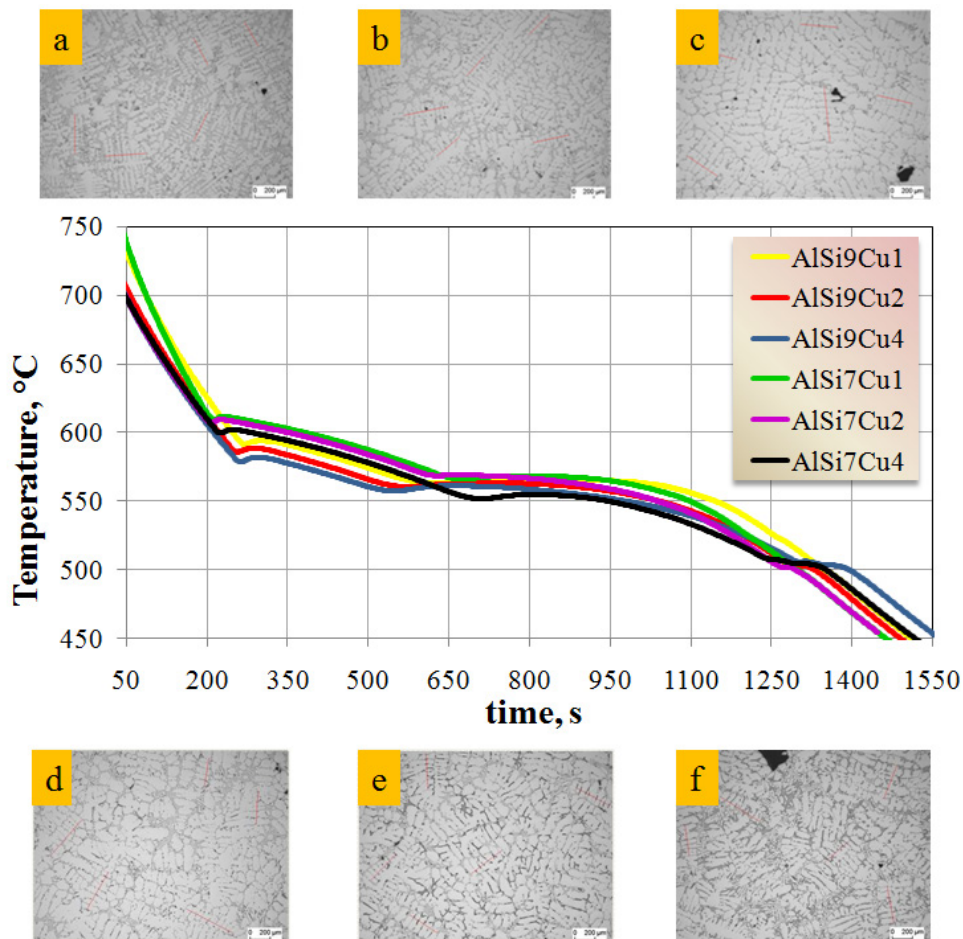


Fig. 5-18 Cooling curves and microphotographs of Al-Si7 and Al-Si9 alloys containing 1, 2 and 4 wt% Cu

a, b, c: Microphotographs of AlSi9 alloys containing 1, 2 and 4 wt% Cu
 d, e, f: Microphotographs of AlSi7 alloys containing 1, 2 and 4 wt% Cu

The microstructure analysis has been done on TA samples in the area close to the tip of thermocouples.

Based on the cooling curves of the six Al-Si-Cu alloys as well additional microstructure analysis the resulted reactions and corresponding temperatures are denoted in the Table 5-4.

It has been observed that the addition of copper in both Al-7Si and Al-Si9 alloys influenced on the reflection points detected on the shown cooling curves. Based on the first derivative of the cooling curves (that are not depicted here because of the visibility of the main details), the temperatures such as $T^{\alpha,den}_{nuc}$ (T_{liq}), $T^{\alpha,den}_{coh}$ (T_{DCP}), $T^{Al-Si}_{E, nuc}$ (T_{Al-Si}), $T^{Al-Cu}_{E, nuc}$ (T_{Al-Cu}), T_{sol} have been determined and one overview of the copper effect on these specific points in both AlSi alloys is presented in Figures (5-19) –(5-23) to be shown later.

Table 5-4 Characteristic reaction in Al-Si7 and Al-Si9 alloys containing different Cu contents

Alloys	Temperature, °C	Reactions
Al-Si7-Cu(1-4)	612.3 - 602.8	Precipitation of α -Al dendritic phase
	568.7 – 554.7	Al-Si eutectic reaction
	502.5 – 508.8	Al-Al ₂ Cu eutectic reaction
	486.8 - 488.9	End of solidification
Al-Si9-Cu(1-4)	595.5 - 581.8	Precipitation of α -Al dendritic phase
	566.4 – 558.0	Al-Si eutectic reaction
	502.3 – 507.3	Al-Al ₂ Cu eutectic reaction
	487.4 - 477.8	End of solidification

As it can be noticed in Fig. 5-19 there is significant effect of Cu addition on the $T^{\alpha,den}_{nuc}$ and $T^{\alpha,den}_{coh}$ point in both Al-Si7 and Al-Si9 alloys. It is obvious that $T^{\alpha,den}_{nuc}$ and $T^{\alpha,den}_{coh}$ point in Al-Si9 alloys are shifted to lower temperatures. That means Si leads to the reduction of $T^{\alpha,den}_{nuc}$ and $T^{\alpha,den}_{coh}$. The addition of Cu in the range of 1-4 wt% in Al-Si7 alloy reduces the $T^{\alpha,den}_{nuc}$ and $T^{\alpha,den}_{coh}$ temperatures of 10 and 15°C respectively. In comparison to Al-Si9 alloy the addition of the same Cu content decrease the $T^{\alpha,den}_{nuc}$ and $T^{\alpha,den}_{coh}$ temperatures of 12 and 8 °C, respectively.

In this case, it can be added that higher Si content in Al-Si alloys especially diminishes the effect of Cu on the $T^{\alpha,den}_{coh}$ temperature.

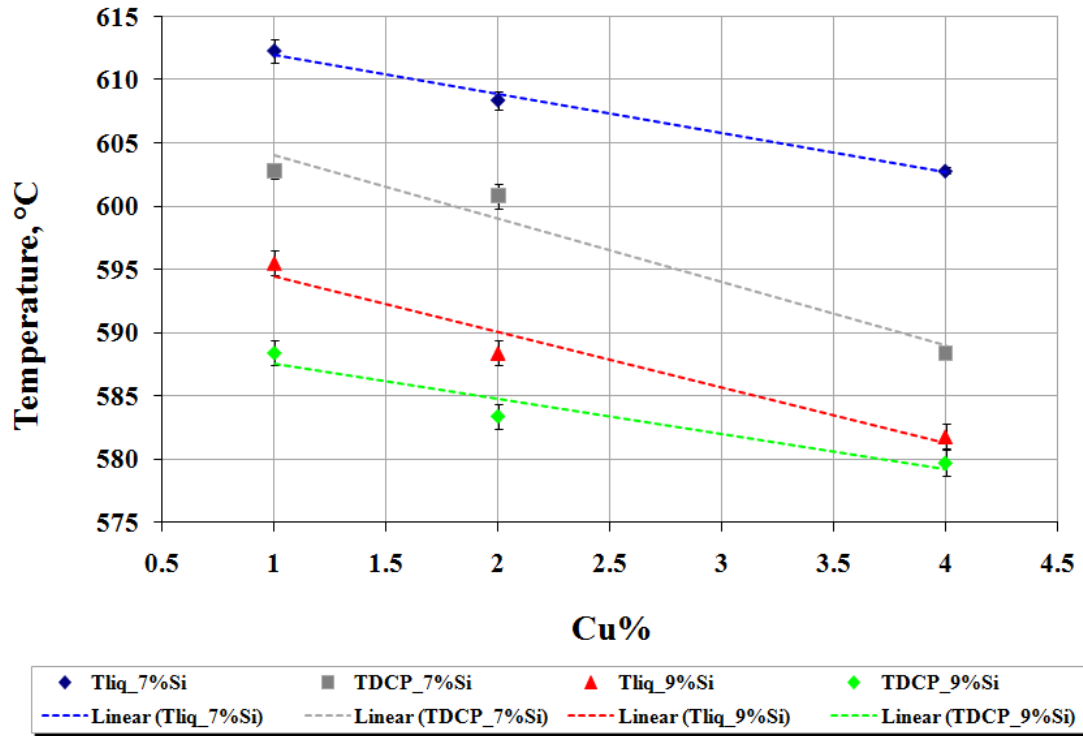


Fig. 5-19 Effect of different Cu contents on the $T_{nuc}^{\alpha,den}$ and $T_{coh}^{\alpha,den}$ temperatures in the Al-Si7 and Al-Si9 alloys

For the concentration range of Cu used in this study, the correlation between $T_{nuc}^{\alpha,den}$ and $T_{coh}^{\alpha,den}$ and Cu wt % in both Al-Si7 and Al-Si9 alloys can be described using the linear expressions with high regression coefficients:

$$T_{nuc}^{\alpha,den} (\text{Al-Si7}) = -3.10 \text{ Cu \%} + 615.1 \text{ }^{\circ}\text{C} \quad R^2 = 0.99 \quad (5-2)$$

$$T_{nuc}^{\alpha,den} (\text{Al-Si9}) = -5.0 \text{ Cu \%} + 609.0 \text{ }^{\circ}\text{C} \quad R^2 = 0.96 \quad (5-3)$$

$$T_{coh}^{\alpha,den} (\text{Al-Si7}) = -4.39 \text{ Cu \%} + 598.8 \text{ }^{\circ}\text{C} \quad R^2 = 0.96 \quad (5-4)$$

$$T_{coh}^{\alpha,den} (\text{Al-Si9}) = -2.78 \text{ Cu \%} + 590.3 \text{ }^{\circ}\text{C} \quad R^2 = 0.93 \quad (5-5)$$

The results regarding the effect of Si and Cu on the DCP point achieved in this study were compared with results of N.L. Veldman et al. [83] showing some agreement but also disagreement. The agreement concerns the effect of Si on the dendrite coherency point, where in both cases DCP point was highly dependent on silicon content. In the work of Veldman et

al. [83] the coherency fraction solid results showed a linear dependence on silicon content. They assumed that dendritic morphology provided a better correlation with coherency than grain size, or the ratio of grain size and growth rate. But on the other side, there was an opposite opinion regarding the effect of copper content on the DCP point in Al-Si-Cu alloys, where it was stated that the effect of silicon was dominant and the addition of 1 and 4 wt% copper had a negligible effect on dendritic morphology, grain size and dendrite coherency point. The results of this study related to the effect of Cu on the DCP point agreed very well with the results of Bäckerud et al [75]. Although in their work the average cooling rate during the solidification was slightly higher (0.6 °C/s) than in this study (0.2 °C/s), they obtained significant decrease of DCP temperature as the Cu content increases from 2.5 to 3.5 wt% in AlSi9Cu alloy that matched very well with results of this work.

The precipitation temperature of major (Al-Si) and minor (Al-Cu) eutectic reactions identified in all cooling curves are denoted in the Table 5-4, but the effect of Cu on the $T_{E, nuc}^{Al-Si}$ and $T_{E, nuc}^{Al-Cu}$ in both Al-Si alloys is depicted in Fig. 5-20.

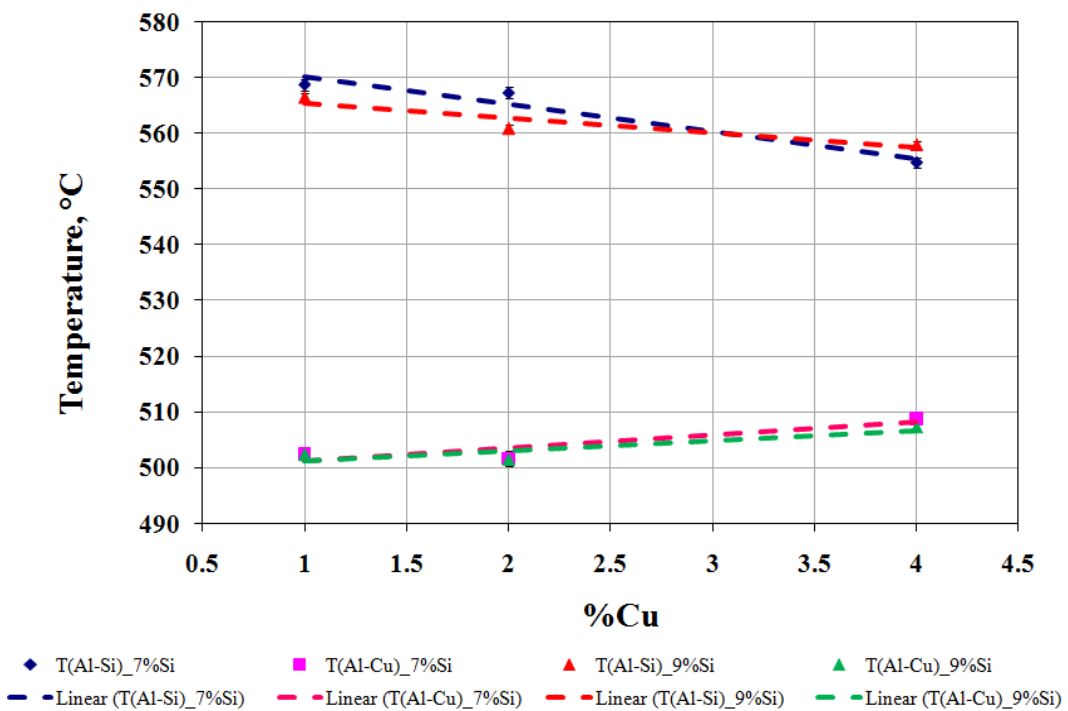


Fig. 5-20 Effect of Cu on $T_{E, nuc}^{Al-Si}$ and $T_{E, nuc}^{Al-Cu}$ eutectic temperatures in Al-Si7 and Al-Si9 alloys

It can be seen in Fig. 5-20 that increase of Cu in both Al-Si alloys led to reduction of $T_{E, nuc}^{Al-Si}$. In this case it could be added that, Si doesn't play significant role as in the case of primary reaction where one visible decrease of $T_{nuc}^{\alpha, den}$ and $T_{coh}^{\alpha, den}$ in Al-Si9 alloys were detected (See Fig. 5-19). There was a slight decrease of $T_{E, nuc}^{Al-Si}$ temperature as the Si content increased. However, such behaviour can be seen in the alloys containing lower Cu content (1 and 2 wt%). The opposite event could be found in the Al-Si alloys containing 4 wt% Cu.

On the other side, it had no effect of Si on the precipitation temperature of minor eutectic. However, the addition of Cu in both Al-Si7 and Al-Si9 alloys contributed to increase of $T_{E, nuc}^{Al-Cu}$ temperature. At the same time that means the Al-Cu eutectic particles will precipitate earlier as the Cu content is higher in Al-Si alloys. In addition to, the form of Cu-bearing phases in the Al-Si-Cu alloy depends on the presence of other alloying elements. As the chemical composition of the alloys (table 5-3) and the obtained cooling curves (Fig. 5-18) indicate, in this case the Cu exists in Al-Si-Cu alloys only in the form of blocky phase Al_2Cu and Al- Al_2Cu eutectic. It was noticed by microstructure observation that in the alloys containing 4 wt % Cu the blocky Al_2Cu phase was more present in both Al-Si alloys, but the appropriate peaks on the cooling curves was not easy to detect.

Based on the results obtained in this study, the correlation between the precipitation temperature of Al-Si and Al-Cu eutectic reactions and copper content can be described by the linear expressions in both Al-Si7 and Al-Si9 alloys as the following:

$$T_{E, nuc}^{Al-Si} (Al-Si7) = -4.89 \text{ Cu \%} + 575.0 \text{ }^\circ\text{C} \quad R^2 = 0.95 \quad (5-6)$$

$$T_{E, nuc}^{Al-Si} (Al-Si9) = -2.91 \text{ Cu \%} + 567.9 \text{ }^\circ\text{C} \quad R^2 = 0.87 \quad (5-7)$$

$$T_{E, nuc}^{Al-Cu} (Al-Si7) = 2.33 \text{ Cu \%} + 498.9 \text{ }^\circ\text{C} \quad R^2 = 0.82 \quad (5-8)$$

$$T_{E, nuc}^{Al-Cu} (Al-Si9) = 1.85 \text{ Cu \%} + 499.4 \text{ }^\circ\text{C} \quad R^2 = 0.80 \quad (5-9)$$

The solidus temperature determined in both AlSi7 and AlSi9 alloys has been varied with the addition of Cu. In Fig. 5-21 it is seen that addition of copper in the range of 1-4 wt% slightly reduced T_{sol} . On the other side, the addition of copper in AlSi9 alloy led to the significant reduction of T_{sol} , about 9 °C. The correlation between T_{sol} and Cu content in both

AlSi alloys is given by the equations (5-10) and (5-11) that both represents polynomial expression of the second degree.

The results regarding effect of Cu content on the microstructure features such as SDAS in both AlSi alloys are plotted in Fig 5-22. As it was expected lower values of SDAS were achieved in the AlSi9 showing the dominance of Si content on the SDAS. At the same time, it was noticed that increase of Cu content in both alloys enabled the refinement of SDAS. The similar trend can be found in the literature [86], but the results corresponded to narrower concentration range of copper.

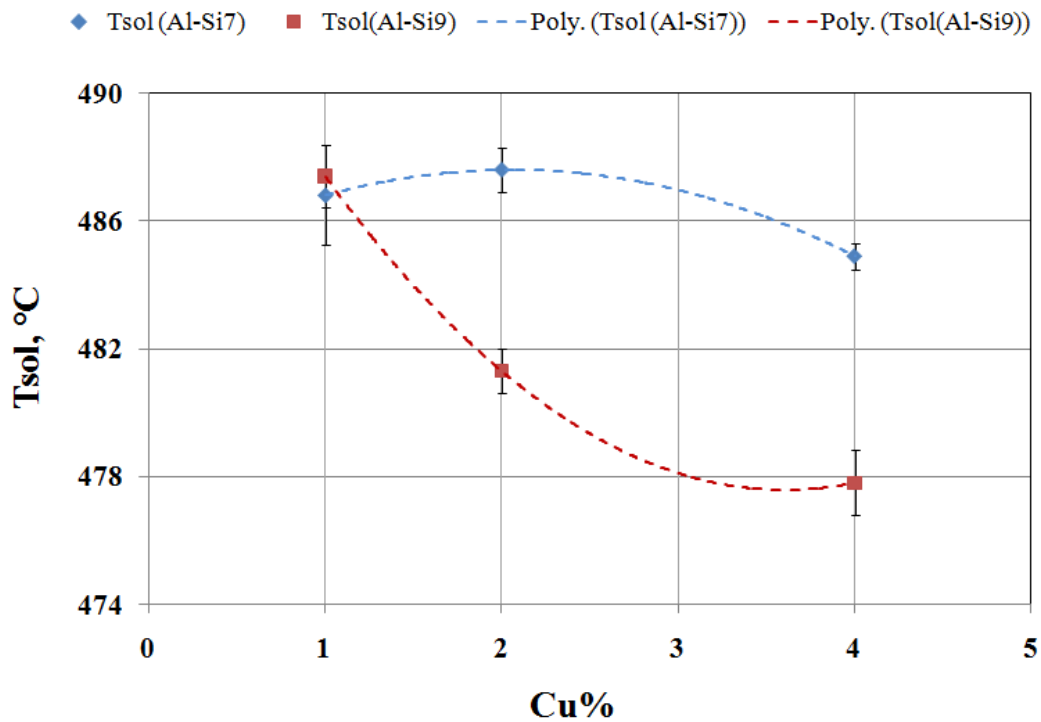


Fig. 5-21 Solidus temperatures of Al-Si7 and Al-Si9 alloys containing different Cu contents

$$T_{\text{sol}}(\text{AlSi7}) = 0.7 (\text{Cu}\%)^2 + 3.0 (\text{Cu}\%) + 484.6 \text{ } ^\circ\text{C} \quad R^2=0.99 \quad (5-10)$$

$$T_{\text{sol}}(\text{AlSi9}) = 1.5 (\text{Cu}\%)^2 - 10.5 (\text{Cu}\%) + 496.4 \text{ } ^\circ\text{C} \quad R^2=0.99 \quad (5-11)$$

The linear equations 5-12 and 5-13 describe the dependence of SDAS and Cu content in both AlSi7 and AlSi9 alloys, showing higher regression coefficient in the case the Al-Si alloy with higher Si content:

$$\text{SDAS (Al-Si7)} = - 1.1(\%Cu) - 57.0 \mu\text{m} \quad R^2=0.63 \quad (5-12)$$

$$\text{SDAS (Al-Si9)} = - 0.8 (\%Cu) + 49.2 \mu\text{m} \quad R^2=0.92 \quad (5-13)$$

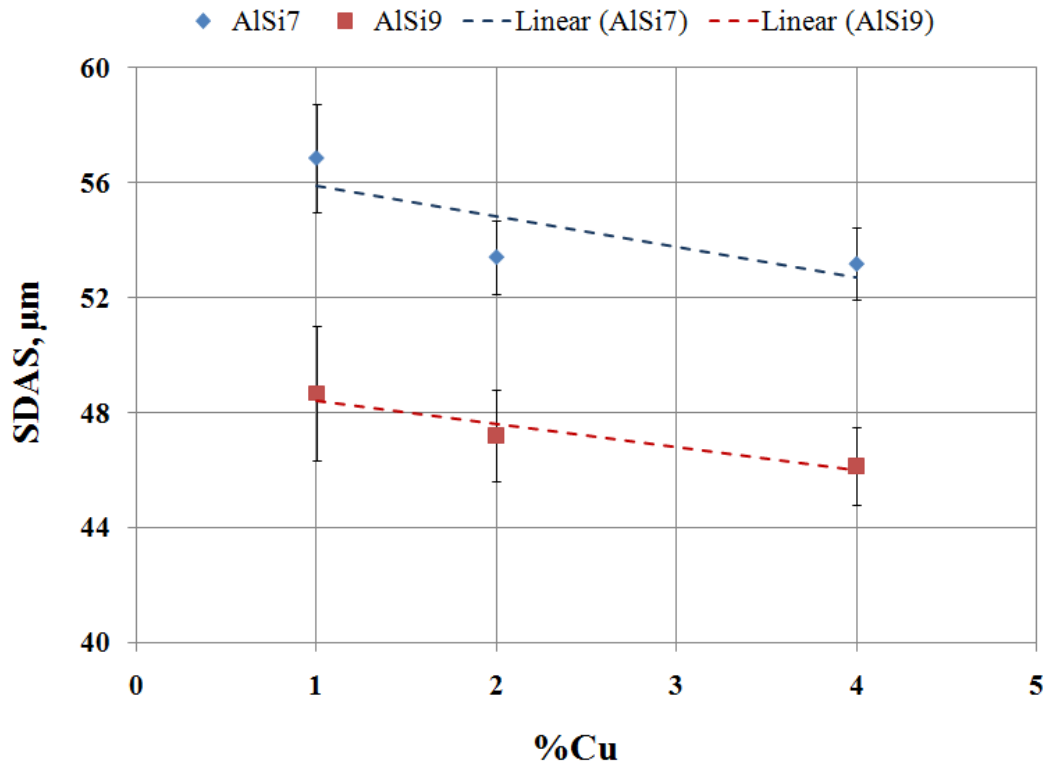


Fig. 5-22 Effect of Cu on the SDAS in Al-Si7 and Al-Si9 alloys

In the Fig. 5-23 the simultaneous impact of copper on the SDAS and the total solidification time (t_f) is plotted. As previously mentioned, copper affects the SDAS in Al-Si-Cu alloys. Regarding the total solidification time, some strong effect of copper was not detected in this study. The mathematical model commonly used in the literature [50, 51, 53, 55, 101] to described the correlation between the SDAS and t_f in Al-Si alloys has been verified. It was shown that there was no good agreement with the experimental values of SDAS and the calculated SDAS values (deviation of calculated values from experimental values was very high, beyond 20%, see Appendix, Table 1A). However, much better agreement has been found between the SDAS and the $\Delta\tau^*$ (time difference between the dendrite coherency point and Al-Si eutectic temperature) where the deviation of calculated values from experimental values range from 0.7 to 8.7 %.

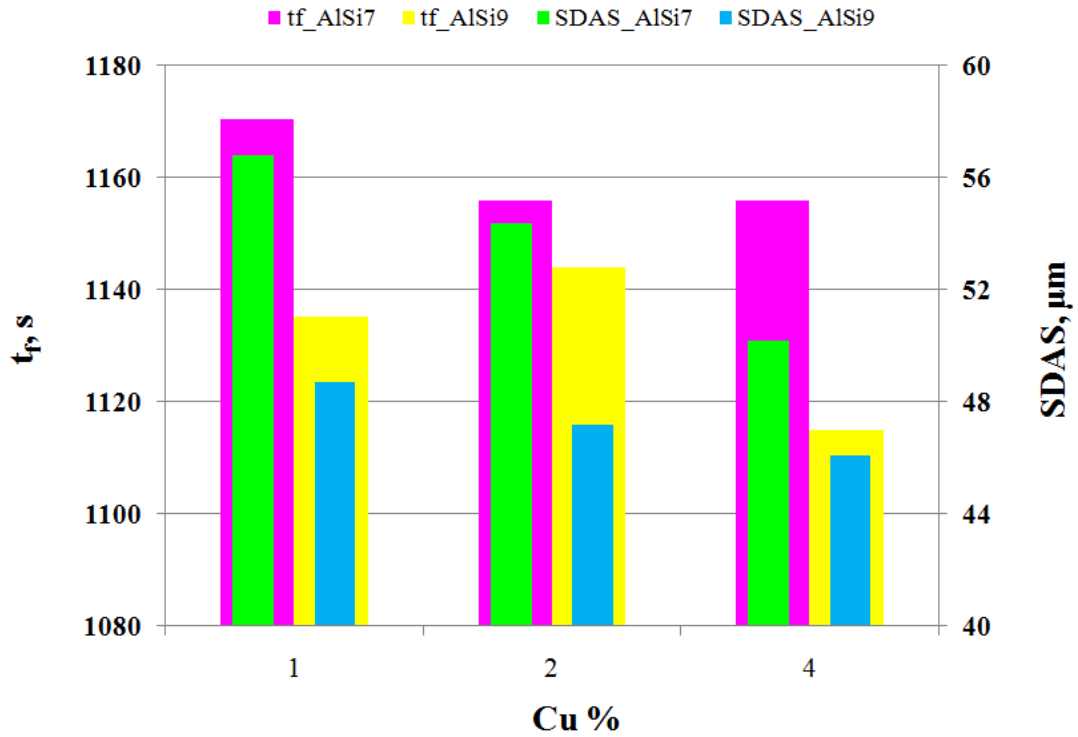


Fig. 5-23 Influence of Cu on t_f and SDAS in AlSi7 and AlSi9 alloys

Fig. 5-24 and 5-25 represent simultaneously SDAS and $\Delta\tau^*$ as a function of Cu content in AlSi7 and AlSi9 alloys respectively.

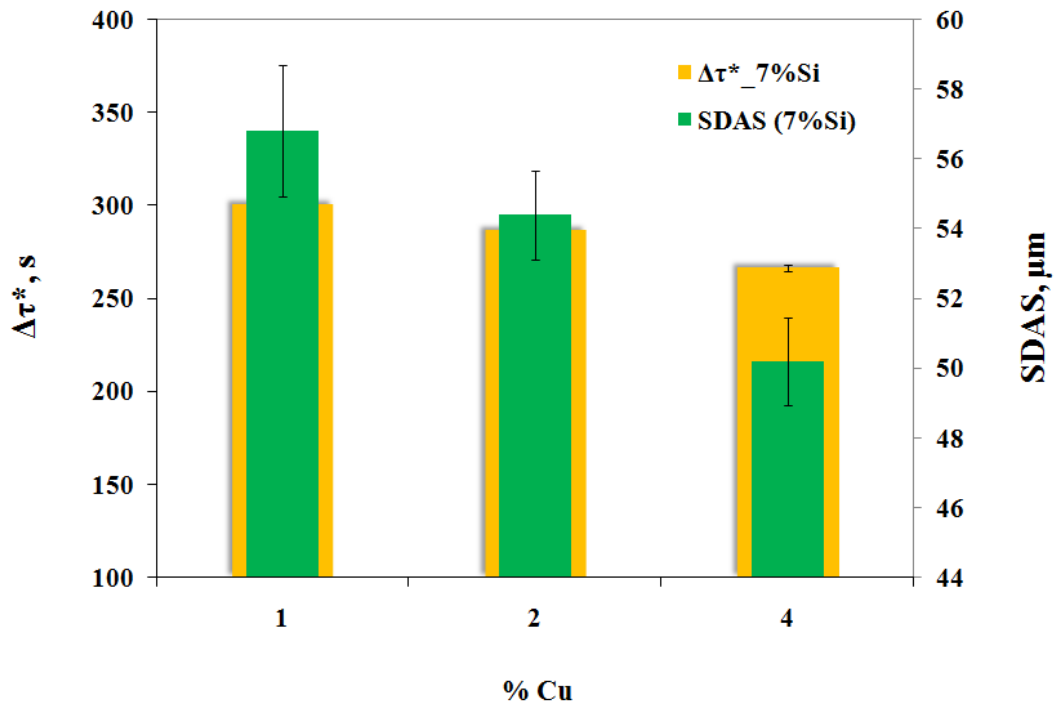


Fig. 5-24 Influence of Cu on $\Delta\tau^*$ and SDAS in AlSi7 alloy

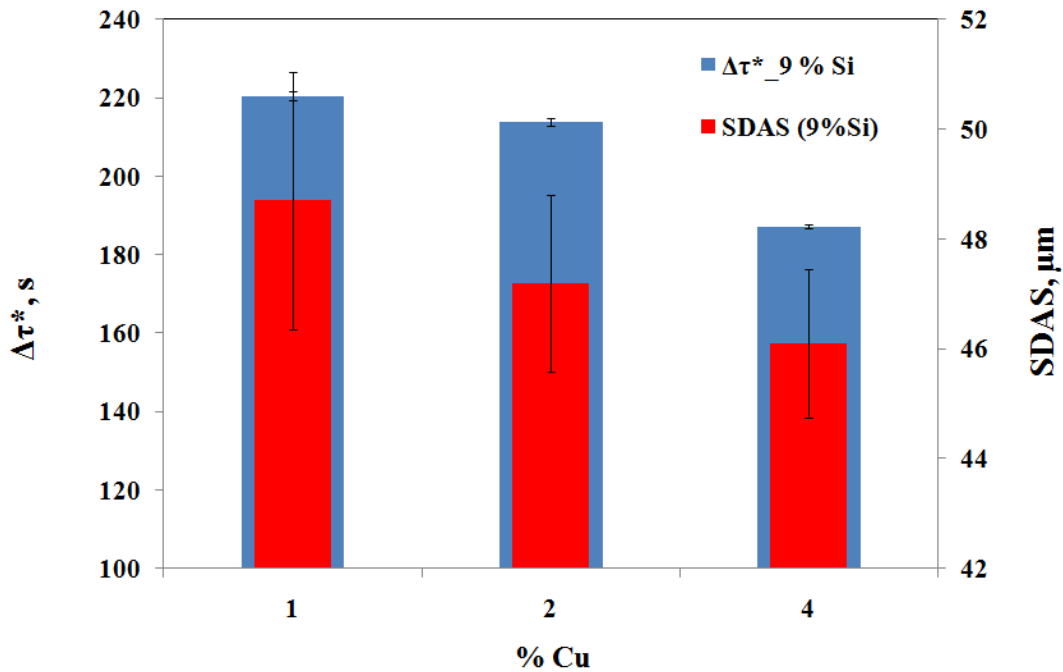


Fig. 5-25 Influence of Cu on $\Delta\tau^*$ and SDAS in AlSi9 alloy

Evidently, the addition of Cu in both alloys results in the simultaneously decrease of SDAS and shorten the parameter, $\Delta\tau^*$. Based on the obtained results, the parameter $\Delta\tau^*$ can be induced in the mathematical model in stead of t_f in order to determine the kinetic of the dendrite growth as a function of chemical composition.

5.5.2. The effect of titanium

The effect of increasing the amount of added grain refiner on grain size and morphology had been investigated over the last five decades. These studies have shown that to achieve a small grain structure it is necessary to provide numerous substrates in the melt that are activated at a low undercooling. It is also necessary to provide undercooling so that the nuclei can survive and form equiaxed crystals. Studies have shown that undercooling provided by the casting process through faster heat extraction rates also decreases the grain size [52, 55, 89, 98, 100]. The addition of grain refiners, usually master alloys containing potent nucleant particles, promotes formation of fine equiaxed grains by deliberately suppressing the growth of columnar and twin columnar grains. The finer equiaxed grain structure ensures uniform mechanical properties, reduced ingot cracking, improved feeding to eliminate shrinkage porosity.

It has been documented in two alloy systems, Pb–Sb [89] and Al–Si [98], that the grain size first decreases with increasing alloy concentration and then, after reaching a minimum, the grain size increases with further grain refinement additions. On the contrary, the groups of authors [66, 67] have shown that the addition of master alloys in A356 alloy provide the steady reduction of grain size showing no minimum. In the work [66], three different grain refiners, Al-Ti10, Al-B5 and Al-4Ti-B1 were used. The Ti content was ranged from 0.11 to 0.17 wt% and B was ranged from 0.01 to 0.07 wt%. Beside the effect of Ti and B on the grain size of AlSi9Cu3 alloy solidified into the permanent metal mold, the effect of Ti and B on the SDAS was investigated as well. As the Ti and B contents increase the grain size decreases. On the other side, a remarkable result has been achieved in the case of SDAS. Other words, Ti and B possess a threshold at 0.11 wt % at 0.01 wt% respectively reaching the minimal value of SDAS. In the work [67], the refinement efficiency of AlTi5C0.25 and AlTi5B1 in A365 alloy was examined. They especially emphasized the benefit of AlTi5C0.25 grain refiner providing obviously reduction of the grain size and SDAS.

Apart from these two papers, there is a lack of further literature data regarding effect of Ti on solidification features and SDAS in Al-Si alloys.

For that reason, the experimental study of this work included the examination of the different titanium content on the solidification features of AlSi7Cu3 alloy such as $T_{nuc}^{\alpha, den}$ (T_{liq}), $T_{coh}^{\alpha, den}$ (T_{DCP}), $T_{E, nuc}^{Al-Si}$ (T_{Al-Si}) $T_{E, nuc}^{Al-Cu}$ (T_{Al-Cu}), T_{sol} as well microstructure feature SDAS. Titanium was added to the melt in the form of Al-Ti5-B1 master alloy. Six different Ti contents used here ranged from 0.08 to 0.14 wt%. For each Ti content three trials have been carried out. All results are expressed as an average value including also the chemical composition of the alloys that is presented in Table 5-5.

The effect of different Ti contents was analysed using the cooling curves and its first derivative and the metallographic method. The cooling curves and microphotographs corresponding to the minimal, medium and maximal Ti contents are illustrated on Fig. 5-26.

As it was expected, Ti showed strongly influence on the primary solidification reaction, but on the contrary, there was no effect of Ti on the Al-Si and Al-Cu eutectic reactions in AlSi7Cu3 alloy. The characteristic reactions and suitable temperatures in AlSi7Cu3 alloy containing different Ti contents are listed in Table 5-6.

Table 5-5 Chemical composition of AlSi7Cu3 alloy containing different Ti contents

Alloy	Si	Fe	Cu	Mn	Mg	Zn	Ti
	wt %						
1A	8.74	0.25	3.49	0.18	0.18	0.10	0.08
2A	8.52	0.23	3.33	0.16	0.20	0.08	0.10
3A	8.58	0.97	3.30	1.46	0.20	0.08	0.11
4A	8.5	0.71	3.23	0.15	0.23	0.08	0.12
5A	8.75	0.24	3.62	0.16	0.20	0.08	0.13
6A	8.44	0.75	3.03	0.17	0.23	0.08	0.14

The effect of different Ti contents on $T^{\alpha,den}_{nuc}(T_{liq})$ and $T^{\alpha,den}_{coh}(T_{DCP})$ in AlSi7Cu3 alloy is presented in Fig. 5-27. The addition of Ti in Al-Si7-Cu3 alloy evidently reduced both temperatures about 8°C. The correlation between $T^{\alpha,den}_{nuc}$ and Ti content is presented by the polynomial equation of the second degree (Eq. 5-14), while the correlation between the $T^{\alpha,den}_{coh}$ and Ti content is described by linear equation (Eq. 5-15).

Table 5-6 Characteristic reaction in AlSi7Cu3 containing different Ti contents

Alloys	Temperature, °C	Reactions
AlSi7Cu3 + (0.08-0.14 %Ti)	596.7 - 589.4	Precipitation of α -Al dendritic phase
	567.7 \pm 1	Al-Si eutectic reaction
	506.4 \pm 1	Al-Al ₂ Cu eutectic reaction
	487 - 472	End of solidification

$$T^{\alpha,den}_{nuc}(AlSi7Cu3) = 4183.7 Ti^2 \% - 1042.7 Ti\% + 653.7 \text{ } ^\circ\text{C} \quad R^2 = 0.85 \quad (5-14)$$

$$T^{\alpha,den}_{coh}(AlSi7Cu3) = -164.5 Ti \% + 599.9 \text{ } ^\circ\text{C} \quad R^2 = 0.93 \quad (5-15)$$

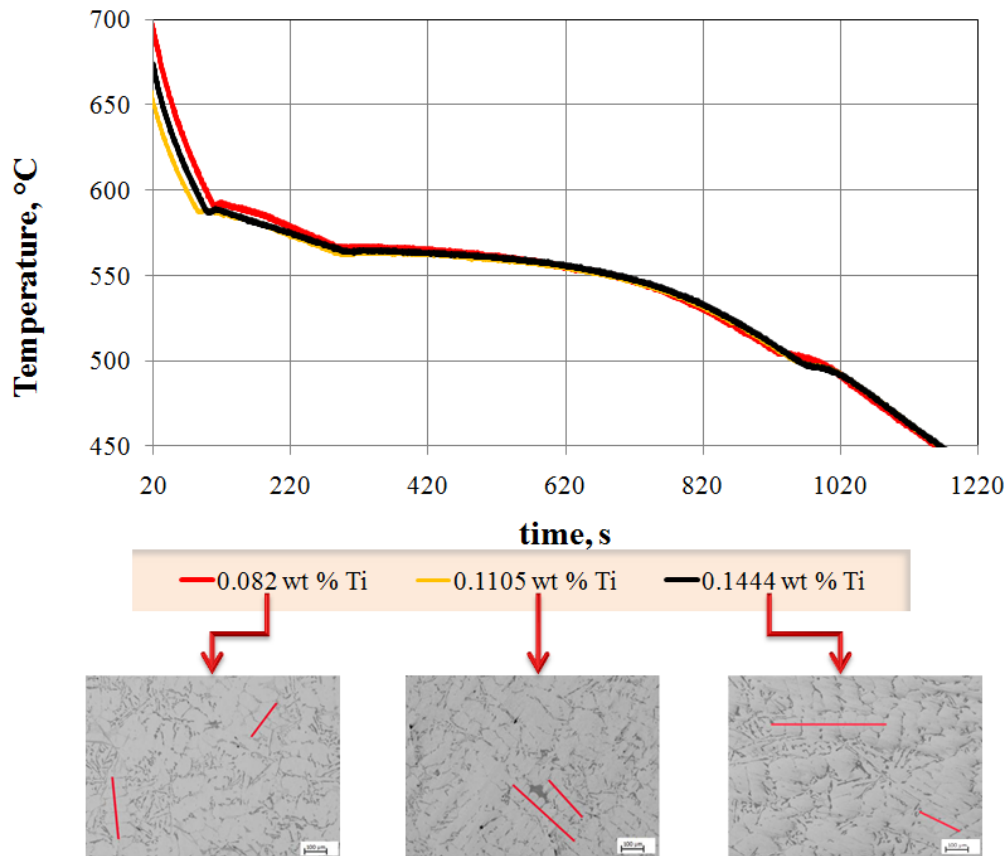


Fig. 5-26 Cooling curves and microphotographs of AlSi7Cu3 alloy containing different Ti contents

As it is seen in Fig. 5-26 all cooling curves overlap each other in the area of major and minor eutectic reactions therefore there is no correlation between $T_{E, nuc}^{Al-Si}$ and $T_{E, nuc}^{Al-Cu}$ (T_{Al-Cu}) and Ti content:

$$T_{E, nuc}^{Al-Si} (AlSi7Cu3) \neq f(Ti\%) \text{ } ^\circ C \quad (5-16)$$

$$T_{E, nuc}^{Al-Cu} (AlSi7Cu3) \neq f(Ti\%) \text{ } ^\circ C \quad (5-17)$$

The effect of Ti on $T_{E, nuc}^{Al-Si}$ and $T_{E, nuc}^{Al-Cu}$ are plotted in Fig. 5-28. In Fig. 5-29 it is shown dependence of T_{sol} on Ti content. From Fig. 5-29 it is clear that the addition of Ti in the range from 0.08 to 0.14 wt% results in reduction of T_{sol} about 15 °C. The dependence between T_{sol} and Ti content can be quite well described by linear equation:

$$T_{sol} (AlSi7Cu3) = -258.4 (Ti\%) + 509.2 \text{ } ^\circ C \quad R^2=0.96 \quad (5-18)$$

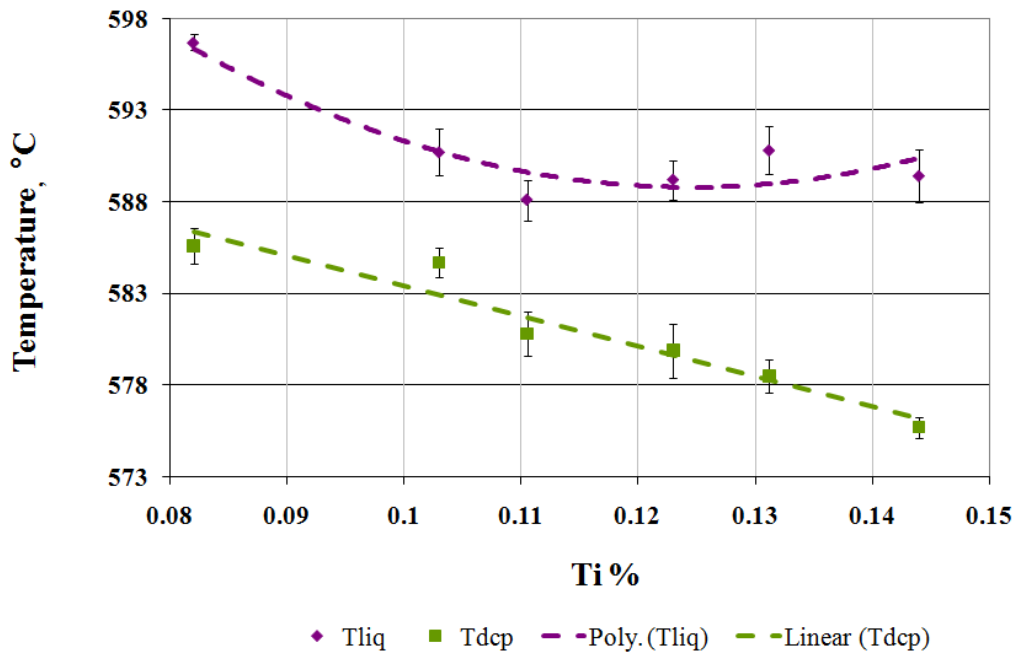


Fig. 5-27 Effect of Ti on $T^{\alpha,den}_{nuc}$ and $T^{\alpha,den}_{dcp}$ temperatures in AlSi7Cu3 alloy

The change of the SDAS with addition of Ti in AlSi7Cu3 alloy is depicted in Fig. 5-30. As it can be observed in Fig. 5-30, there is a remarkable reduction of the SDAS with addition of Ti in AlSi7Cu3 alloy. The increase of Ti content from 0.08 up to 0.14 wt % results the reduction of SDAS from 64 to 52 μm . Nonetheless, the SDAS reaches an optimal value of 51.5 μm when the Ti content was 0.12 wt%. Taking into account the presence of SDAS threshold at 0.12 wt% Ti, the optimal fitting has been relatively difficult to find. The maximal regression coefficient $R^2 = 0.77$ was reached for polynomial expression of the second degree:

$$\text{SDAS} = 1166.7 (\text{Ti \%})^2 - 500.2 (\text{Ti \%}) + 98.1 \quad R^2 = 0.77 \quad (5-19)$$

Some similar study about effect of Ti on the SDAS can be found in the work of B.Hu and H.Li [66]. They examined the effect of different grain refiners, Al-Ti, Al-B and Al-Ti-B on the grain size and SDAS in AlSi9Cu3 alloy. It should be underlined that the casting conditions were not the same as in this PhD work. Actually, for producing the specimen the steel die, made of H13 steel was used in the reference [66]. In that way the cooling down was significantly faster and the obtained values of SDAS were in the range of 20-35 μm but representing the same trend. In that case optimal SDAS value in AlSi9Cu3 alloy was reached with the addition of 0.11 wt% Ti (18 μm), while the grain size rapidly decreases as the

addition up to 0.13 wt% Ti, with addition of Ti above 0.13 wt% not further affecting the grain size.

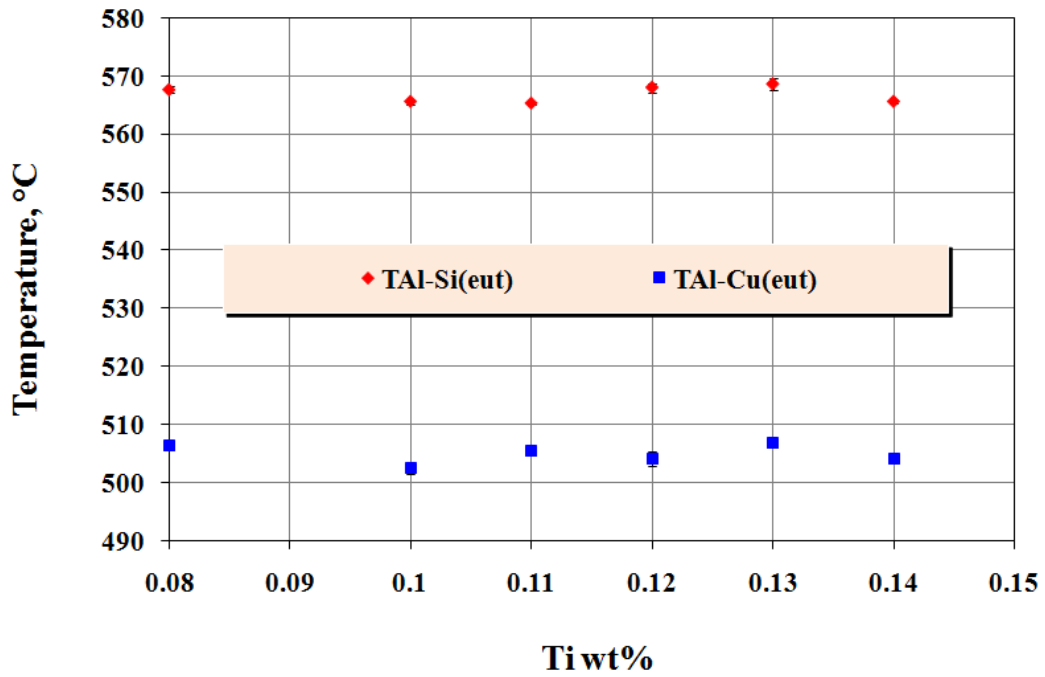


Fig. 5-28 Effect of Ti on $T_{E, nuc}^{Al-Si}$ and $T_{E, nuc}^{Al-Cu}$ in AlSi7Cu3 alloy

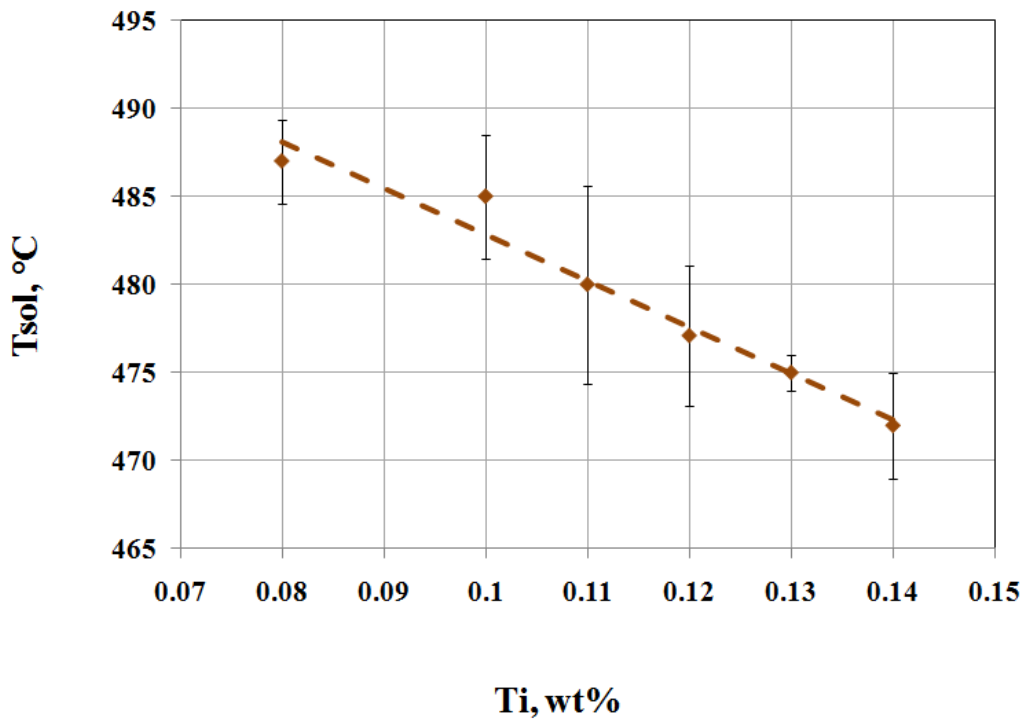


Fig. 5-29 Effect of Ti on Tsol in AlSi7Cu3 alloy

Their results reveal that an optimum amount of Ti for grain size refinement does not always match with the amount of Ti for optimal SDAS reduction. In this study, the grain size was not measured, but the impressive coincidence is the same trend of SDAS obtained in different Al-Si-Cu alloys, under different cooling conditions and Ti amount.

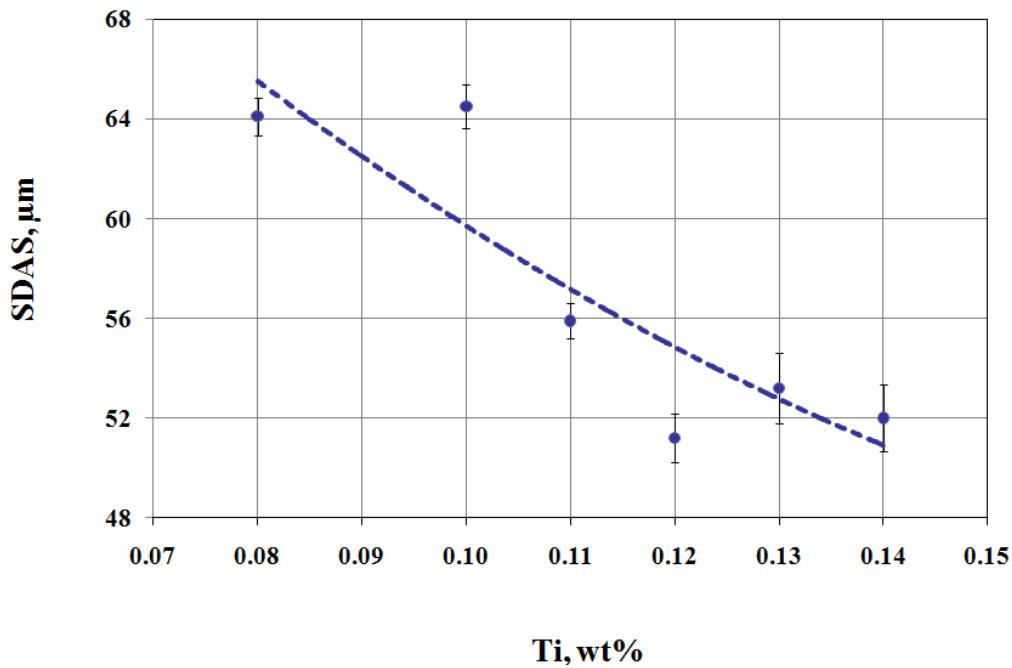


Fig. 5-30 Effect of Ti on the SDAS in AlSi7Cu3 alloy

Taking into account the literature data and the results revealed in this work, that was proven that effect of Ti on SDAS is distinguished from the effect of Ti on the grain, but until now there are not enough data that can illuminate this issue in Al-Si alloys. In the work of B.Hu and H.Li it was clarified that the higher Ti content in the melt led to the rapid growth of existing TiAl_3 nuclei instead of the formation of the new TiAl_3 which did not change grain refining effect (when in this case Ti wt% is above 0.13 wt%), but the growth of TiAl_3 at higher Ti content could reduce the active Ti elements inside the melt and in that way caused an increase of SDAS.

Fig. 5-31 and 5-32 illustrate the SDAS versus t_f and SDAS versus $\Delta\tau^*$, respectively in AlSi7Cu3 alloy.

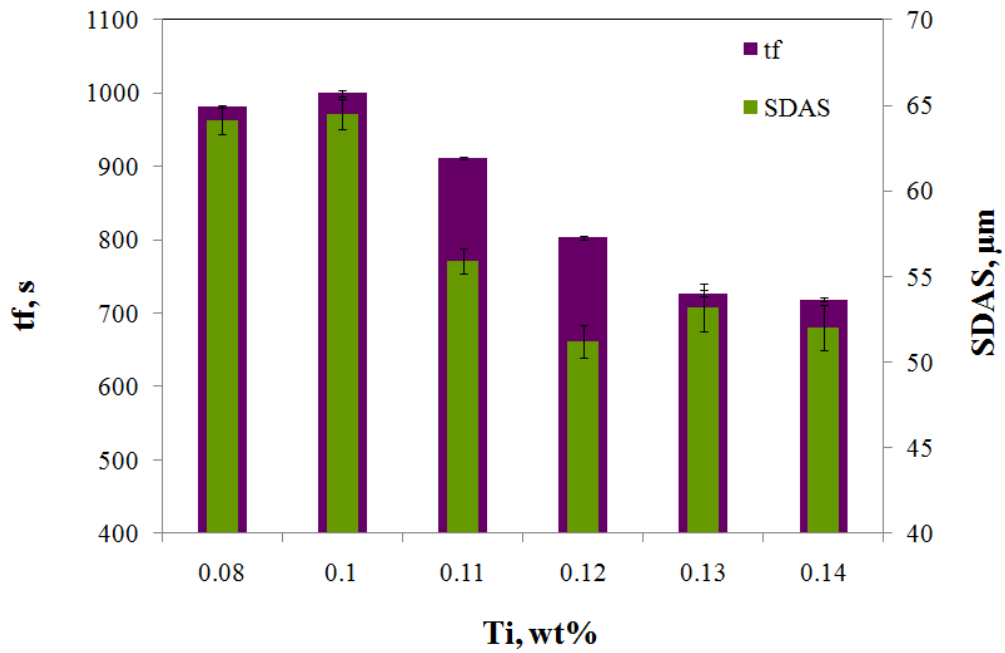


Fig. 5-31 Influence of Ti on t_f and SDAS in AlSi7Cu3 alloy

It can be seen in Fig 5-31 there is a steady reduction of solidification time as Ti content increases, while in the case of SDAS one minimum at 0.12 wt% Ti can be noted and above that slight increase of SDAS value. Completely another behaviour was discovered in the case of $\Delta\tau^*$ versus Ti content, where one minimum corresponding to 0.12 wt% Ti as same as in the case of SDAS was detected.

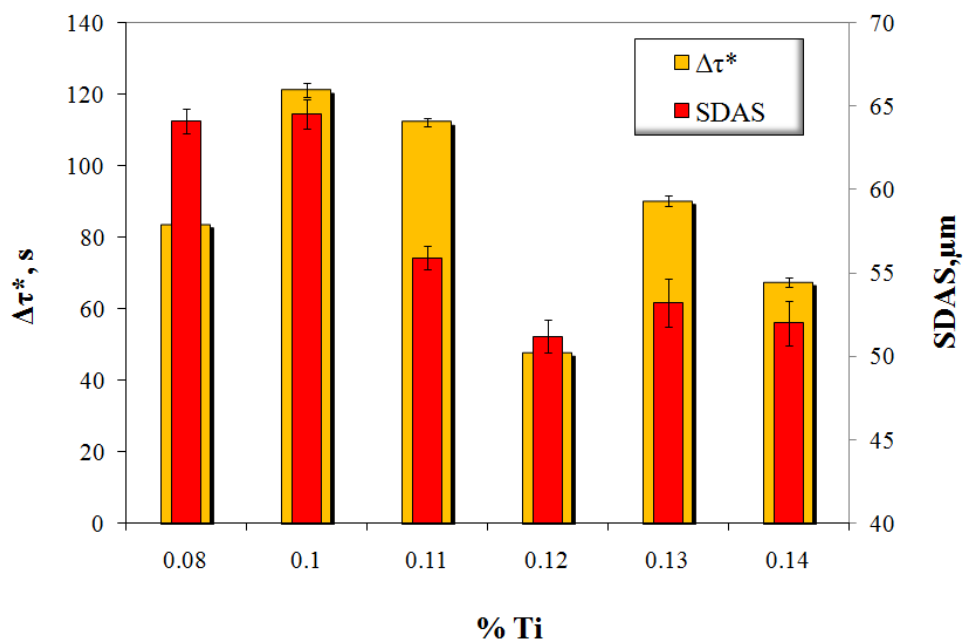


Fig. 5-32 Influence of Ti on $\Delta\tau^*$ and SDAS in AlSi7Cu3 alloy

The same mathematical model expressed by Eq. 3-3 was used to calculate the SDAS value of AlSi7Cu3 alloy containing varying Ti contents based on total solidification time, t_f and $\Delta\tau^*$. The difference between the experimental values of SDAS and the calculated values of SDAS suggested that without additional modification the tested mathematical model could not be valid for both correlations SDAS- t_f and SDAS- $\Delta\tau^*$ (see Appendix, Table 2A).

5.5.3. The effect of zinc

Zinc has a relatively high solubility in aluminum both at high temperature and at room temperature [114]. During solidification, zinc successively goes into solid solution and it is therefore expected to alter only the liquidus region. However, the role of zinc is not well understood. Aluminum-zinc alloys containing other elements offer the highest combination of tensile properties in wrought aluminum alloys. It is believed that zinc up to 3.00 wt % may improve the high-temperature properties of aluminium alloys besides machinability [34, 43]. Particularly, the role of Zn in solidification of Al-Si alloys and its impact on the solidification features as well microstructure features such as SDAS have not been investigated until the present time. Only, in the paper of Gowri and Samuel [85], some experimental data regarding effect of Zn on A380 alloy solidification can be found. Nevertheless, the content of Zn in their work did not cover the range of Zn (0-3.0 wt%) that could be detected in Al-Si alloys obtained from the secondary alloys. They tested behaviour of Zn in A380 alloy only for two content 1.7 and 3.0 wt%.

In this study the zinc content was varied in the range from 0.5 to 3.0 wt % and the average chemical composition of all test samples (1A-5A) is presented in Table 5-7.

Table 5-7 Chemical composition of Al-Si-Cu alloys containing different Zn content

Alloy	Si	Fe	Cu	Mn	Mg	Zn	Ti
	wt %						
1A	7.61	0.63	3.35	0.29	0.30	0.87	0.14
2A	7.68	0.60	3.57	0.30	0.30	1.21	0.14
3A	7.97	0.68	3.65	0.29	0.28	1.78	0.12
4A	7.93	0.62	3.46	0.33	0.27	2.41	0.11
5A	7.51	0.47	3.37	0.21	0.23	2.77	0.12

The solidification features $T^{\alpha,den}_{nuc}$ (T_{liq}), $T^{\alpha,den}_{coh}$ (T_{DCP}), $T^{Al-Si}_{E, nuc}$ (T_{Al-Si}) $T^{Al-Cu}_{E, nuc}$ (T_{Al-Cu}), T_{sol} , and SDAS, analysed previously as the functions of different Si, Cu and Ti content were as well examined as functions of different Zn contents in AlSi7Cu3 alloy.

The resulting cooling curves for the minimal, medium and maximal Zn content and corresponding microstructures can be seen in Fig. 5-33. There was an observable change of the initial part of cooling curves with the addition of Zn what indicated that Zn shifted $T^{\alpha,den}_{nuc}$ temperature and also a slight effect of Zn on the Al-Cu eutectic reaction was noted. The major Al-Si eutectic reaction was not affected by the addition of zinc in AlSi7Cu3 alloys.

The characteristic reactions identified on the cooling curves of AlSi7Cu3 alloys containing different Zn content and the temperatures at which the reactions took place are denoted in Table 5-8.

Table 5-8 Characteristic reactions in AlSi7Cu3 containing different Zn contents

Alloys	Temperature, °C	Reactions
AlSi7Cu3 + (0.5 -3.0 wt %Zn)	598.6 - 591.4	Precipitation of α -Al dendritic phase
	560.3 \pm 0.5	Al-Si eutectic reaction
	493.6 - 488.6	Al-Al ₂ Cu eutectic reaction
	473 - 464	End of solidification

The effect of different Zn contents on $T^{\alpha,den}_{nuc}$ and $T^{\alpha,den}_{coh}$ is presented in Fig. 5-34. As it can be seen in Fig. 5-34, the addition of Zn up to 2.8 wt% enabled the reduction of the $T^{\alpha,den}_{nuc}$ and $T^{\alpha,den}_{coh}$ about 7 and 4°C respectively. In comparison to Si, Cu and Ti, the effect of Zn on $T^{\alpha,den}_{nuc}$ and $T^{\alpha,den}_{coh}$ was less pronounced.

The correlation between different Zn contents and $T^{\alpha,den}_{nuc}$ and $T^{\alpha,den}_{coh}$ can be described using logarithmic expressions:

$$T^{\alpha,den}_{nuc}(\text{AlSi7Cu3}) = -5.3 \ln(\text{Zn \%}) + 597.3 \text{ °C} \quad R^2 = 0.90 \quad (5-20)$$

$$T^{\alpha,den}_{coh}(\text{AlSi7Cu3}) = -3.2 \ln(\text{Zn \%}) + 592.9 \text{ °C} \quad R^2 = 0.99 \quad (5-21)$$

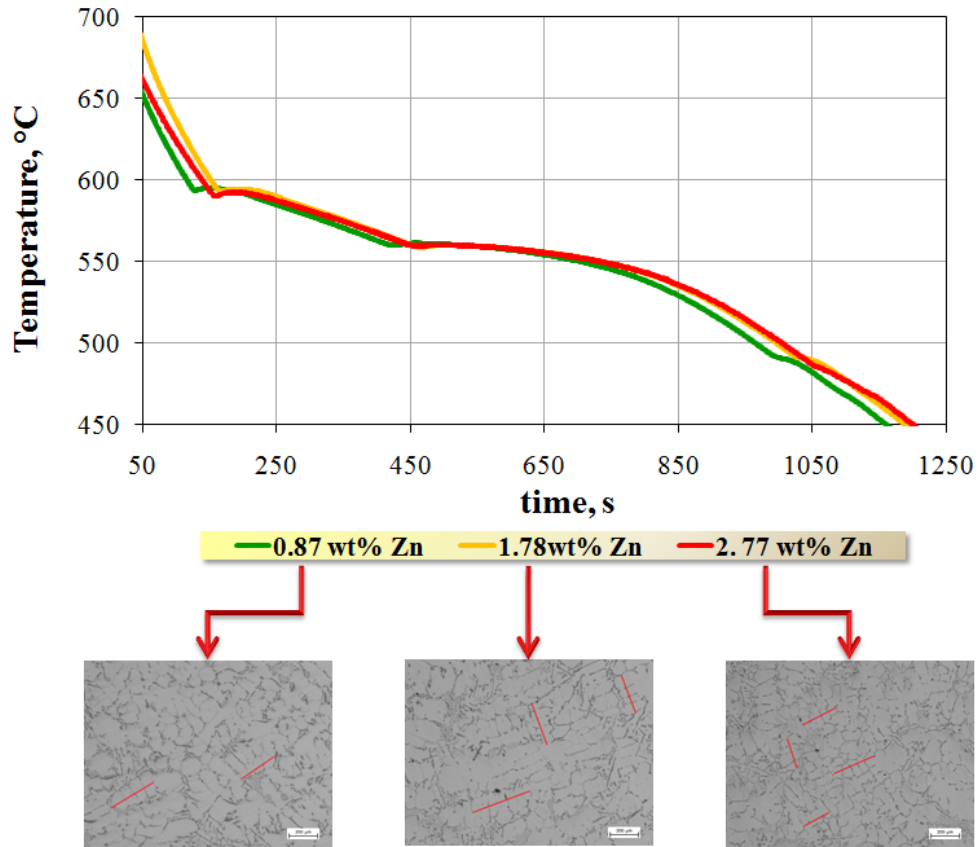


Fig. 5-33 Cooling curves and microphotographs of AlSi7Cu3 alloy containing different Zn contents

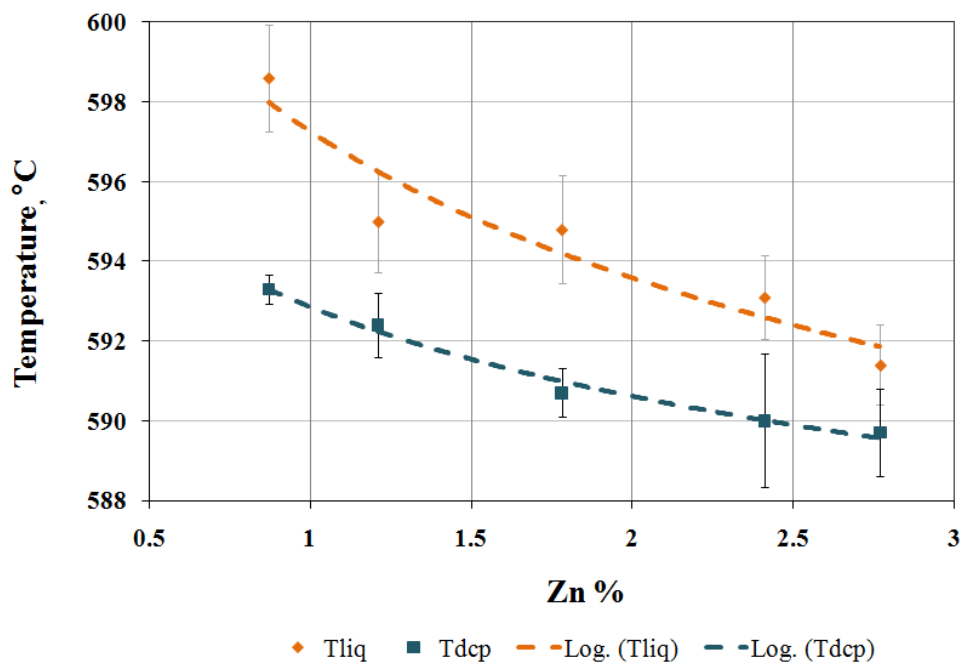


Fig. 5-34 Effect of Zn on $T_{nuc}^{\alpha,den}$ and $T_{dcp}^{\alpha,den}$ temperatures in AlSi7Cu3 alloy

It has been previously mentioned that addition of Zn did not influence on the Al-Si eutectic reaction as well $T_{\text{nuc}}^{\text{Al-Si}}$ temperature. On the other side, $T_{\text{nuc}}^{\text{Al-Cu}}$ temperature was slightly affected by the addition of Zn. The $T_{\text{nuc}}^{\text{Al-Si}}$ and $T_{\text{nuc}}^{\text{Al-Cu}}$ versus Zn content are shown in Fig. 5-36. It was observed that addition of Zn up to 2.8 wt% resulted the reduction of $T_{\text{nuc}}^{\text{Al-Cu}}$ about 5 °C. The relationship between Zn content and both eutectic temperatures can be described by the following expressions:

$$T_{E, \text{nuc}}^{\text{Al-Si}}(\text{AlSi7Cu3}) \neq f(\text{Zn \%}) \text{ } ^\circ\text{C} \quad (5-22)$$

$$T_{E, \text{nuc}}^{\text{Al-Cu}}(\text{AlSi7Cu3}) = -2.7 (\text{Zn}\%)^2 + 6.5 (\text{Ti}\%) + 489.9 \text{ } ^\circ\text{C} \quad R^2 = 0.97 \quad (5-23)$$

As it can be seen in Fig. 5-37, Zn strongly influenced T_{sol} in AlSi7Cu3 alloy. The addition of Zn up to 2.8 wt% contributed to the remarkable decrease of T_{sol} about 19 °C.

The correlation between T_{sol} and Zn content is given by the following equation:

$$T_{\text{sol}}(\text{AlSi7Cu3}) = -9.1(\text{Zn}\%) + 489.7 \text{ } ^\circ\text{C} \quad R^2 = 0.94 \quad (5-24)$$

The influence of Zn addition on the microstructure can be seen in the microphotographs presented in Fig. 5-35.

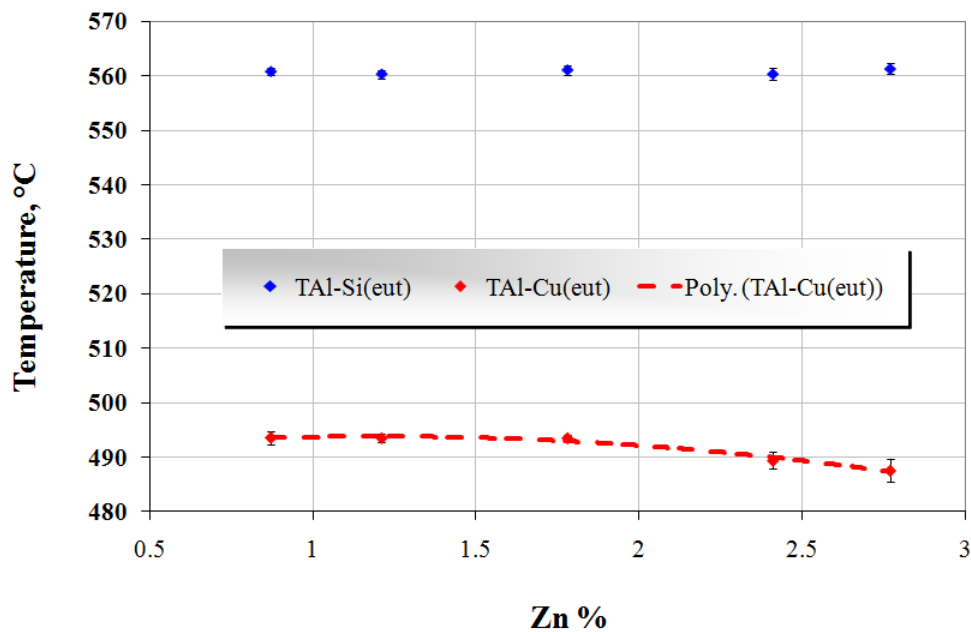


Fig. 5-35 Effect of Zn on $T_{\text{nuc}}^{\text{Al-Si}}$ and $T_{\text{nuc}}^{\text{Al-Cu}}$ temperatures in AlSi7Cu3 alloy

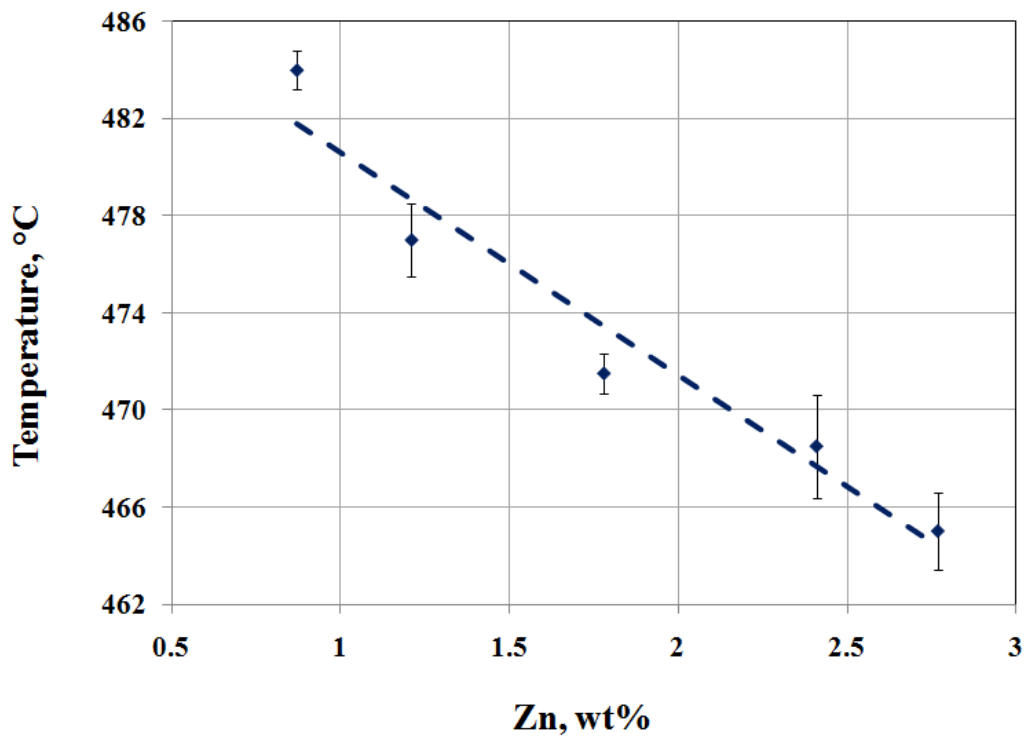


Fig. 5-36 Effect of Zn content on T_{sol} in AlSi7Cu3 alloy

As microphotographs in Fig. 5-34 reveal, the addition of Zn enable microstructure refinement, particularly decrease of SDAS. In Fig. 5-37 it is shown that increase of Zn content from 0.5 up to 2.8 wt% results the reduction of SDAS of $6.7 \mu\text{m}$.

The correlation equation that the best expresses relationship between Zn content and SDAS is a polynomial equation of the second degree:

$$\text{SDAS} = 0.33(\text{Zn } \%)^2 - 3.2 (\text{Zn } \%) + 66.4 \mu\text{m} \quad R^2 = 0.85 \quad (5-24)$$

Since the addition of Zn leads to the reduction of SDAS in AlSi7Cu3, it is expected that at the same time the addition of Zn shortens the total solidification time, t_f . On the contrary, the results shown in Fig. 5-38 revealed completely another dependence between t_f and Zn contents. At the same time, the addition of Zn led to shorten $\Delta\tau^*$ and that indicated on the same trend as in the case of SDAS versus Zn content. This effect of Zn on SDAS and $\Delta\tau^*$ is illustrated in Fig. 5-39.

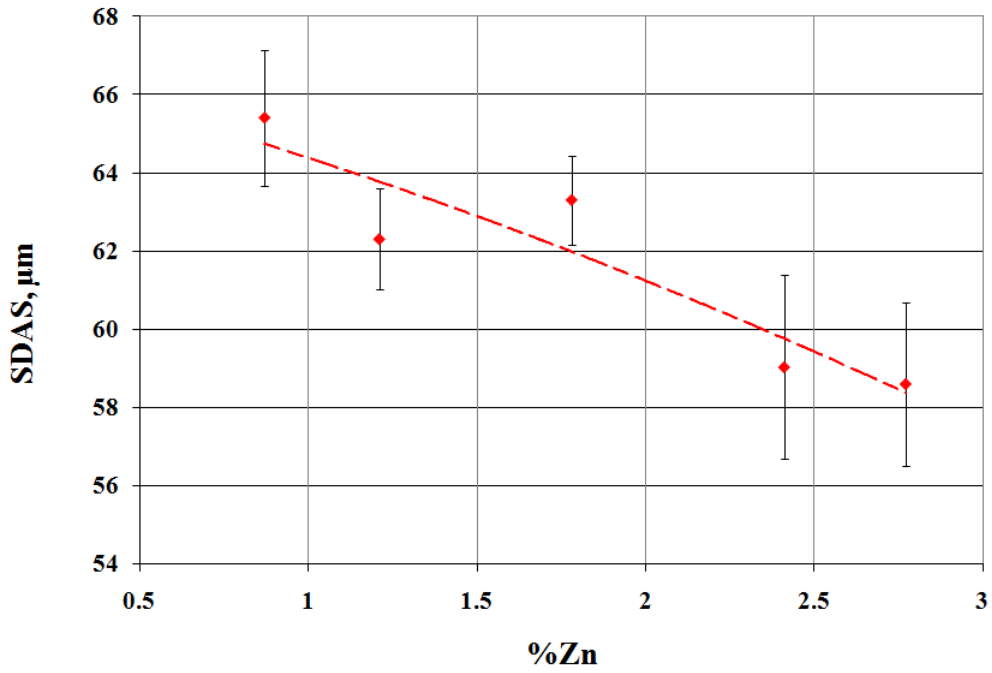


Fig. 5-37 Effect of Zn on the SDAS in AlSi7Cu3 alloy

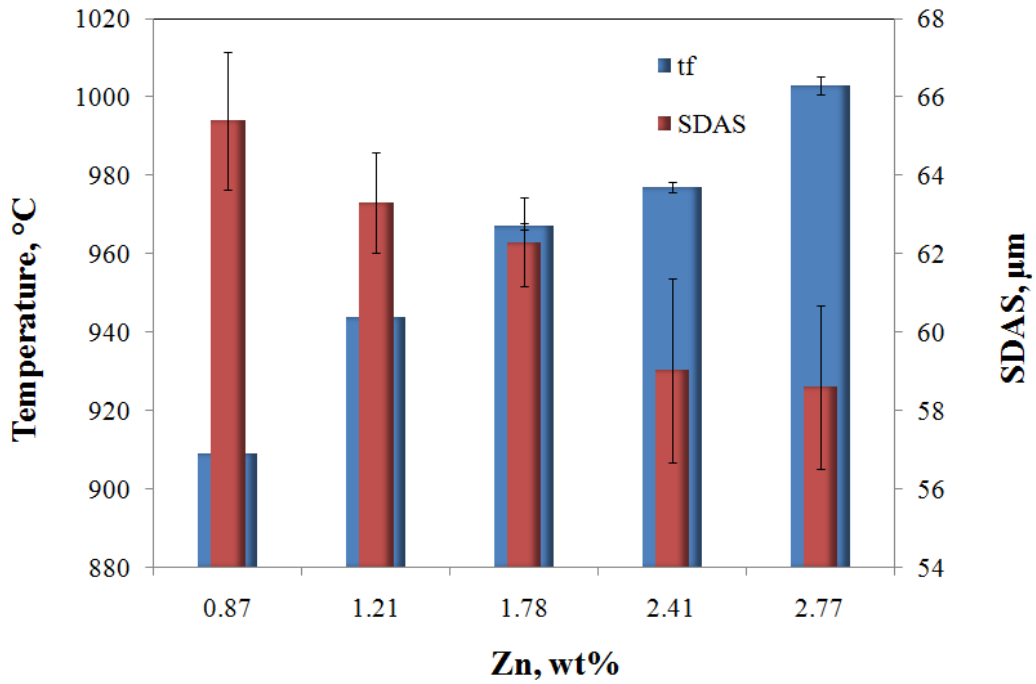


Fig. 5-38 Influence of Zn content on t_r and SDAS in AlSi7Cu3 alloy

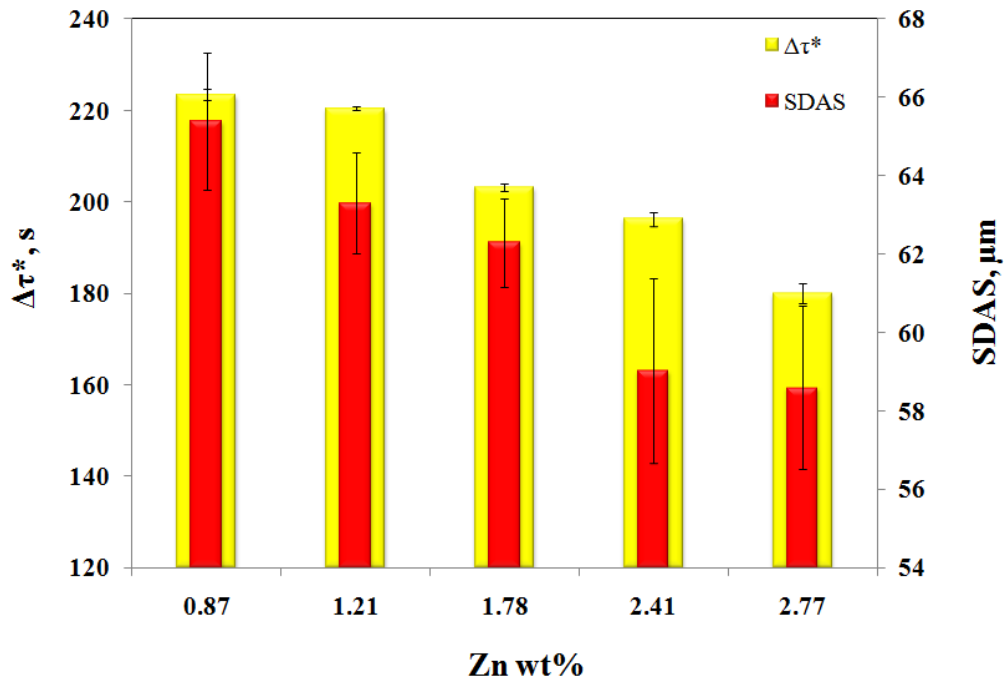


Fig. 5-39 Influence of Zn content on $\Delta\tau^*$ and SDAS in AlSi7Cu3 alloy

Based on the obtained results, it could be outlined that more suitable kinetic parameter that determined the dendrite growth as Zn content was varied, might be $\Delta\tau^*$. Verification of the mathematical model (Eq. 3-3) describing SDAS and solidification time relationship, has very good agreement can be achieved, especially when the value of the coarsening factor in the equation (3-3) M is 7. In that case, the deviation of experimental values of SDAS from calculated values of SDAS ranges between 1 and 4.8 % (see Table 3A in Appendix).

5.5.4. The effect of magnesium

In the European specification for AlSi7Cu3 alloy, the maximal allowed concentration of Mg is 0.3 wt%. Since the majority of die-casting alloys are produced from secondary sources (scrap) which inherently contain a higher percentage of magnesium, it becomes a heavy burden on the part of secondary smelters to remove that excess of magnesium. Therefore, there has been an active campaign to change the allowable level of magnesium in alloys. Inspire of the numerous studies done to establish the beneficial effect of increasing magnesium on the mechanical and machining properties, the specification still stands at max. 0.3 wt%. Alike, the effects of Mg on the solidification features of aluminum alloys are not being extensively researched in the literature. Few available works [86, 115-117] deal only

with the impact of Mg on the solidification feature, such as effect of Mg on the major and minor eutectic temperature of Al-Si alloys. In the work of Heusner and Schneider [115], it was found that addition of Mg up to 1 wt% in AlSi11 alloy leads to the dramatically reduction of Al-Si eutectic temperature of 10 °C. As it was reported in the reference [86], the increase of Mg content up to 0.5 wt% lower both the major (Al-Si) and minor (Al-Cu) eutectic temperature of A380 alloy. Unfortunately, there is a lack of literature data regarding the effect of Mg on other solidification features as well microstructure feature such as SDAS. Especially the concentrations of Mg above 1 wt% in AlSi alloys have not until present time investigated. This study was focused on the solidification behaviour of AlSi7Cu3 alloy in the presence of higher magnesium contents, ranged from 0.22 to 2.97 wt%. The study examines the effect of Mg from 0.22 to 2.97 wt%. on the solidification features, $T_{nuc}^{\alpha,den}(T_{liq})$, $T_{coh}^{\alpha,den}(T_{DCP})$, $T_{E, nuc}^{Al-Si}$, $T_{E, nuc}^{Al-Cu}$, T_{sol} and SDAS. The chemical composition of all tested alloys containing different Mg contents from the mentioned range is presented in Table 5-9.

Table 5-9 Chemical composition of AlSi7Cu3 alloy containing different Mg contents

Alloy	Si	Fe	Cu	Mn	Mg	Zn	Ti
	wt %						
1A	7.39	0.37	3.33	0.40	0.22	0.56	0.15
2A	7.48	0.39	3.45	0.41	0.53	0.63	0.15
3A	7.18	0.45	3.62	0.11	1.10	0.62	0.15
4A	7.35	0.39	3.63	0.42	1.64	0.64	0.15
5A	7.65	0.44	3.18	0.45	2.22	0.61	0.15
6A	7.80	0.38	3.46	0.37	2.97	0.62	0.15

Three representative cooling curves related to the minimal, medium and maximal Mg content in AlSi7Cu3 alloy including the corresponding microphotographs are shown in Fig.5-40. Looking at the shown microphotographs, it is noticeable that the addition of Mg enables microstructure refinement, as a first decrease of SDAS. As magnesium level increases, the amount of Mg₂Si phase present in the microstructure increases to. Inspire of the higher magnesium content (> 0.5 wt%), the Mg₂Si phase was faintly visible in the microstructure (see the microphotograph corresponding the minimum Mg content).

It is deduced from the cooling curves shown in Fig. 5-41 that Mg addition changes not only the region of the eutectic reactions as it was reported in the mentioned literature [85, 115] but also the impact of Mg on the primary reaction and the end of solidification process can be observed. Among the common reactions detected in AlSi7Cu3 alloys, adding Mg above 1 wt%, the precipitation reaction of Mg₂Si phases can be also detected. All reaction identified on the cooling curves of AlSi7Cu3 alloy containing different Mg contents are listed in Table 5-10.

It is necessary to add that the peak of Mg₂Si phase on the cooling curves was extremely visible for the Mg content of 1.1 and 1.6 wt%. Above 1.6 wt% Mg, the peak of major eutectic reaction and the peak related to the precipitation of Mg₂Si phase overlap presumably each other. As it was stated in reference [118], Q - Al₅Cu₂Mg₈Si₆ phase can be also expected in the microstructure and this phase precipitates together with Mg₂Si phase when Mg wt% is higher than 0.5 wt%. The detection of Q-phase in microstructure of alloys containing above 0.5 wt% Mg failed in this study.

Table 5-10 Characteristic reactions and temperatures in AlSi7Cu3 alloy containing Mg

Alloys	Temperature, °C	Reactions
AlSi7Cu3 + (0.2 -3.0 wt %Mg)	603.3 – 598.7	Precipitation of α-Al dendritic phase
	562.5 – 536.3	Al-Si eutectic reaction
	543.2 - 536	Precipitation of Mg ₂ Si phase
	505 - 496.6	Al-Al ₂ Cu eutectic reaction
	487.5 – 479	End of solidification

The effect of different Mg contents on $T_{nuc}^{\alpha,den}$ and $T_{coh}^{\alpha,den}$ temperatures can be seen in Fig. 5-41. From the charts presented in Fig. 5-41, it can be seen that increase of Mg content from 0.22 up to 2.97 wt% reduces both $T_{nuc}^{\alpha,den}$ and $T_{coh}^{\alpha,den}$ temperatures about 5 and 7 °C, respectively.

In this case, the correlation between $T_{nuc}^{\alpha,den}$ and Mg content can be expressed by a linear equation, while a polynomial expression of the second degree is fitted the best to the correlation between $T_{coh}^{\alpha,den}$ and Mg content. These equations can be written as the following:

$$T_{nuc}^{\alpha,den}(\text{AlSi7Cu3}) = -2.0 \text{ Mg \%} + 604.3 \text{ }^{\circ}\text{C} \quad R^2 = 0.92 \quad (5-24)$$

$$T_{coh}^{\alpha,den}(\text{AlSi7Cu3}) = -0.5 (\text{Mg\%})^2 - 4.8 (\text{Mg\%}) + 589.1 \text{ }^{\circ}\text{C} \quad R^2 = 0.90 \quad (5-25)$$

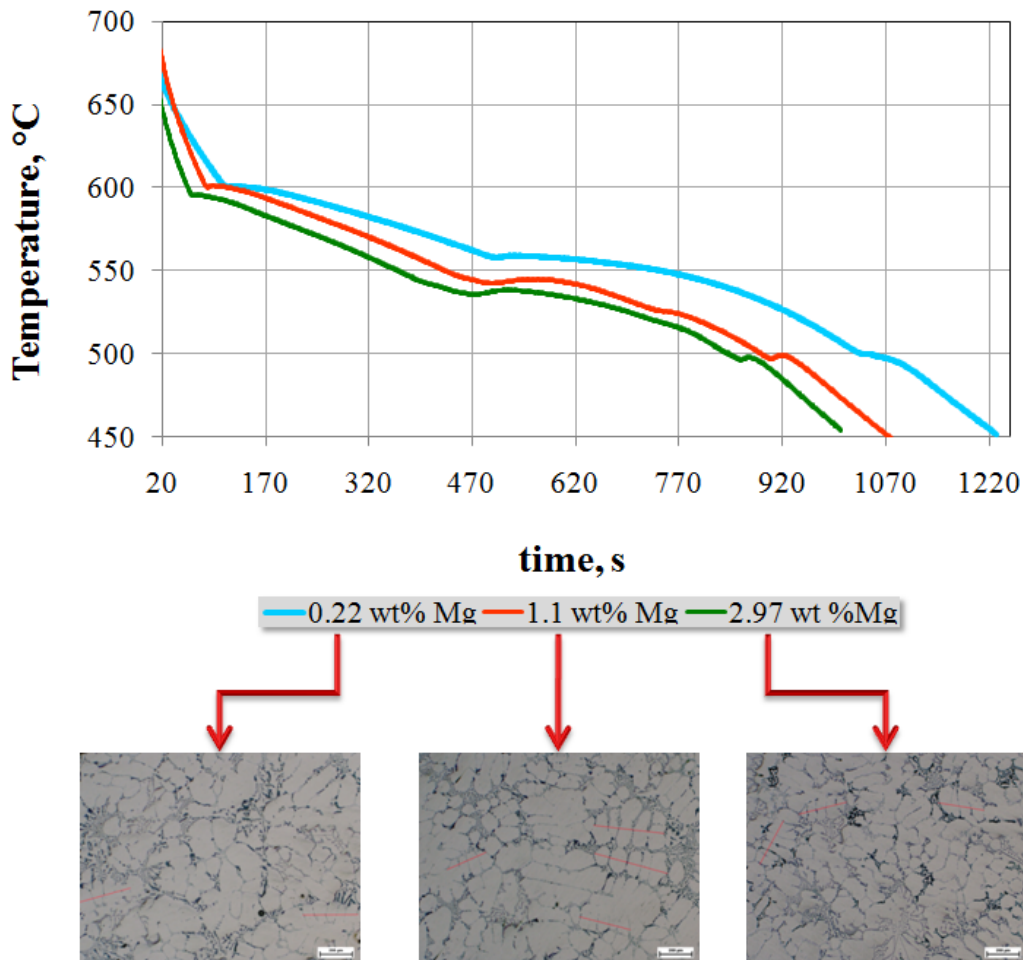


Fig. 5-40 Cooling curves and microphotographs corresponding to minimum, medium and maximum Mg content in AlSi7Cu3 alloy

In Fig. 5-42 it is illustrated the effect of Mg on $T_{E, nuc}^{\text{Al-Si}}$ and $T_{E, nuc}^{\text{Al-Cu}}$ temperatures. As it is observed, the $T_{E, nuc}^{\text{Al-Si}}$ temperature is strongly affected by the addition of Mg. In addition to, the eutectic silicon becomes finer in the presence of higher Mg content. The increase of Mg from 0.22 to 2.97 wt% contributes to the substantial decrease of $T_{E, nuc}^{\text{Al-Si}}$ temperature about 20 °C. On the contrary, the addition of Mg has no such strong influence on the $T_{E, nuc}^{\text{Al-Cu}}$ temperature in AlSi7Cu3 alloy. In other words, the addition of Mg up to 1 wt % cause a slight increase of $T_{E, nuc}^{\text{Al-Cu}}$, while the addition from 1 up to 3 wt% Mg enables the decrease of $T_{E, nuc}^{\text{Al-Cu}}$ about 10 °C.

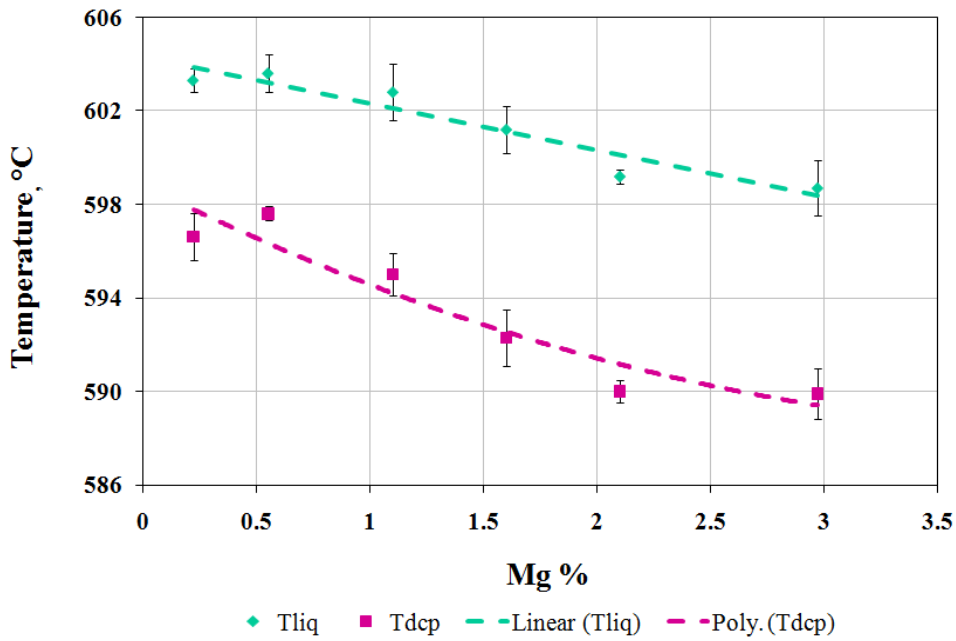


Fig. 5-41 Effect of Mg content on $T^{\alpha,den}_{nuc}$ and $T^{\alpha,den}_{coh}$ in AlSi7Cu3 alloy

According to the results shown in Fig. 5-43, the correlations between $T^{Al-Si}_{E, nuc}$ and $T^{Al-Cu}_{E, nuc}$ and Mg content can be described using the following expressions:

$$T^{Al-Si}_{E, nuc} (AlSi7Cu3) = -9.9 \ln(Mg\%) + 547.4 \text{ } ^\circ\text{C} \quad R^2 = 0.97 \quad (5-26)$$

$$T^{Al-Cu}_{E, nuc} (AlSi7Cu3) = -3.6(Mg\%)^2 + 9.6(Mg\%) + 498.6 \text{ } ^\circ\text{C} \quad R^2 = 0.96 \quad (5-27)$$

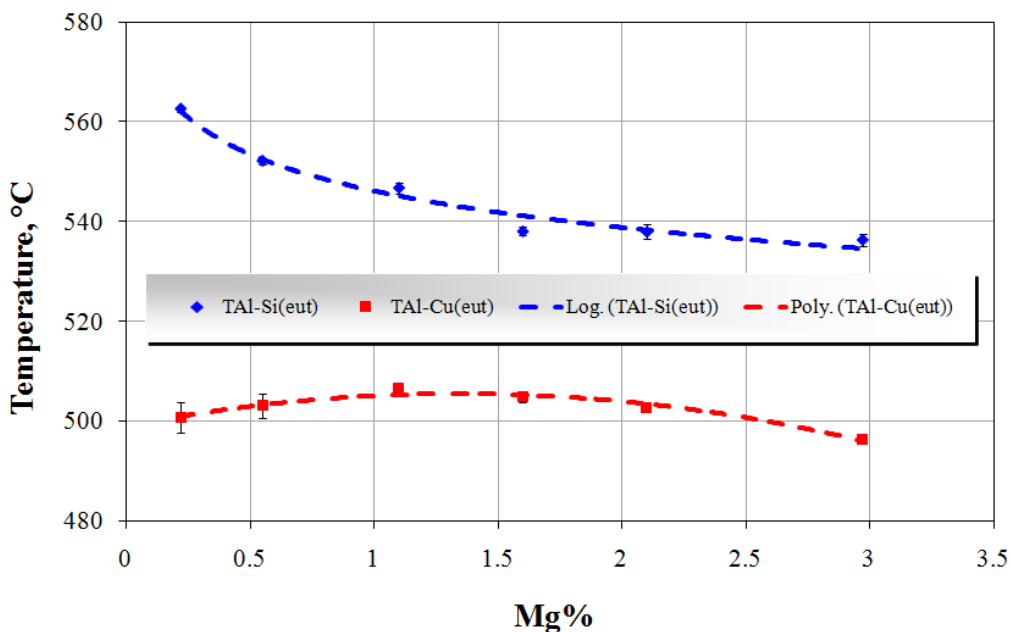


Fig. 5-42 Effect of Mg content on $T^{Al-Si}_{E, nuc}$ and $T^{Al-Cu}_{E, nuc}$ temperatures in AlSi7Cu3

As it was previously mentioned, Mg has also impact on the end of solidification process. In fact, Mg shifts T_{sol} to lower values shorten the total solidification time of AlSi7Cu3 alloy. The effect of Mg on T_{sol} can be seen in Fig. 5-43. From Fig. 5-43 it is seen that increase of Mg from 0.22 to 3.0 wt% lead to the reduction of T_{sol} approximately 11 °C. The relationship between Mg content and T_{sol} can be expressed by polynomial equation of the second degree as following:

$$T_{sol}(AlSi7Cu3) = -0.3 (Mg\%)^2 - 3.0(Mg\%) + 487.2 \text{ } ^\circ\text{C} \quad R^2=0.95 \quad (5-29)$$

In order to estimate the effect of SDAS, the cooling curve analysis has been supplemented by the metallographical observation. The results of metallographic analysis reveal that Mg addition strongly reduces the SDAS value in AlSi7Cu3 alloy. As it is depicted in Fig. 5-44 the increase of Mg content from 0.22 to 2.97 wt% reduces the SDAS in Al-Si7Cu3 alloy about 17 μm .

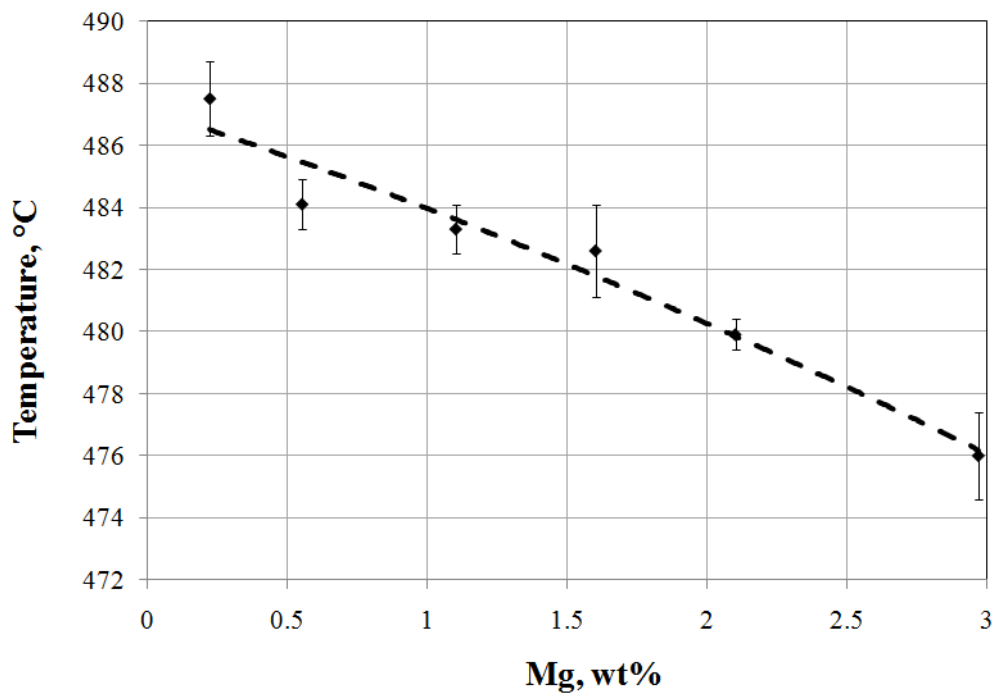


Fig. 5-43 Effect of Mg content on T_{sol} temperature in AlSi7Cu3 alloy

Using the polynomial expression of the second degree the correlation between SDAS and Mg content can be described with high regression coefficient as it follows:

$$\text{SDAS (AlSi7Cu3)} = 2.5(\text{Mg \%})^2 - 14.3(\text{Mg \%}) + 69.6 \mu\text{m} \quad R^2 = 0.99 \quad (5-30)$$

It was also found that Mg addition in AlSi7Cu3 alloy makes the total solidification time shorter and at the same time reduces the SDAS values. Fig. 5-45 illustrates the trend of SDAS and t_f versus Mg additions. Similar trend can be noticed in Fig. 5-46 showing the influence of Mg addition on SDAS and $\Delta\tau^*$ in AlSi7Cu3 alloy. The mathematical model (3-3) commonly used to express the relationship between SDAS and t_f has been also verified by the results with Mg regarding relationship between SDAS and t_f as well SDAS and $\Delta\tau^*$. When the kinetic parameter $\Delta\tau^*$ is inserted in the Eq (3-3), the deviation of experimental SDAS values from the calculated was up to 10 %. Unlike that result, higher deviation (up to 30 %) was achieved applying the t_f in the Eq (3-3). In that way, it was shown that $\Delta\tau^*$ might be more suitable kinetic parameter determining the dendrite growth when the Mg content was varied.

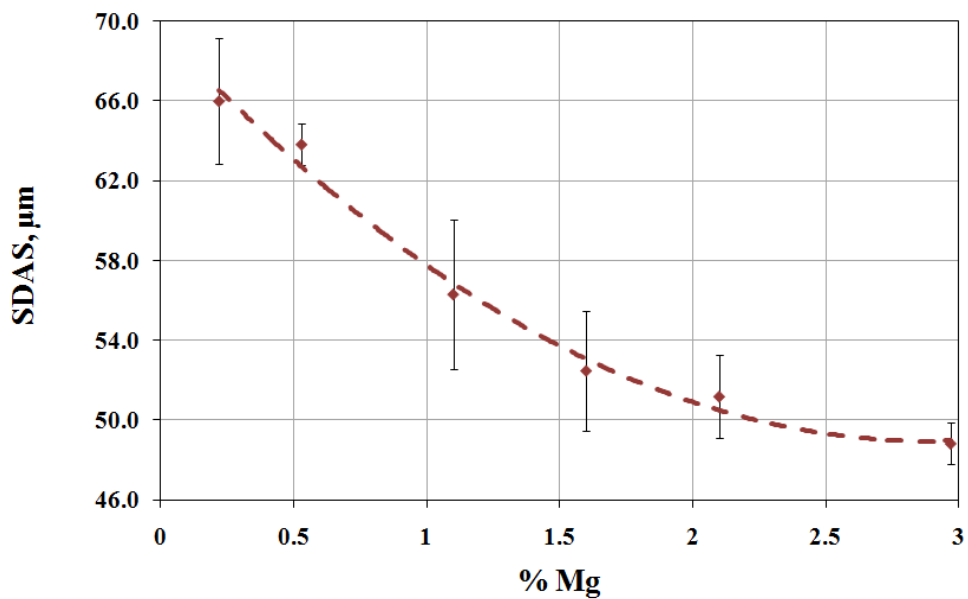


Fig. 5-44 Influence of Mg on the SDAS in AlSi7Cu3 alloy

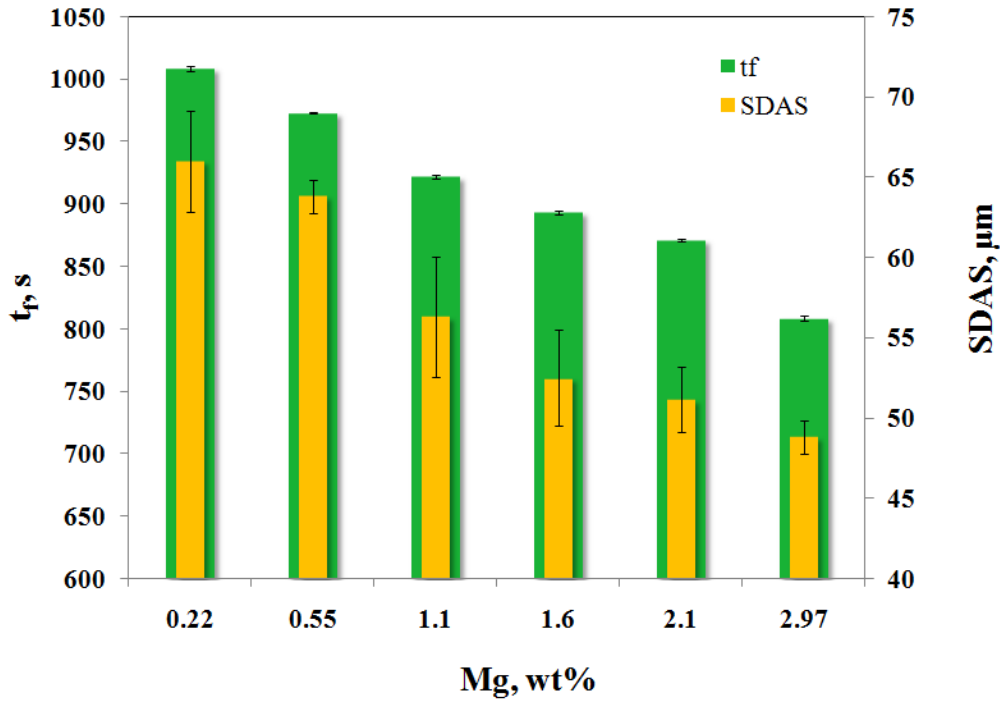


Fig. 5-45 Influence of Mg on the SDAS and t_f in AlSi7Cu3 alloy

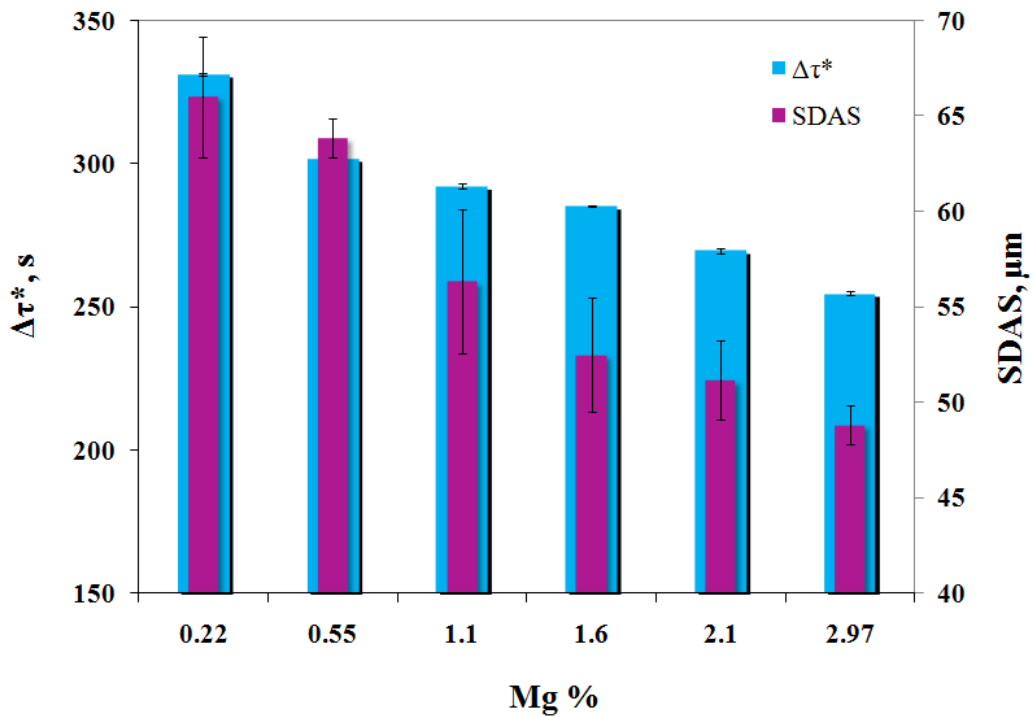


Fig. 5-46 Influence of Mg on the SDAS and $\Delta\tau^*$ in AlSi7Cu3 alloy

5.5.5. The effect of strontium

Although the major alloying elements have significant impact on the solidification path of AlSiCu alloys, there are also some minor elements that can change solidification path of AlSiCu alloys [116-121]. Strontium is one of these elements, normally added to aluminum melt in order to modify the morphology of the Al-Si eutectic. Modifiers such as sodium and strontium in hypoeutectic silicon alloys (essentially those with less than 12% silicon) tend to reduce interfacial tension between eutectic phases. The reduction in interfacial tension increases the contact angle between aluminum and silicon, allowing the aluminum to envelop and arrest the growth of the silicon crystal. The modifying effect is the transition from blocky, acicular and needle-like silicon phases to a fine fibrous silicon structure [122]. This improved microstructure leads to enhancement of the properties of the cast products. As it was reported in the reference [123], the addition of Sr changes also the morphology of Cu-phases in AlSiCu alloys, leading to more intensive precipitation of so called “blocky”, Al₂Cu phase that Cu-eutectic form, Al-Al₂Cu.

This study shows the state-of the art in understanding the main effect of Sr on the solidification behaviour of AlSi7Cu3 alloy. Although the addition of Sr to Al-Si alloys is generally related to the term of modification of eutectic silicon, in fact the Al-Si growth temperature, in this work it is also proven that Sr possesses an additional effect regarding precipitation of the minor eutectic Al-Al₂Cu eutectic as well the fraction of copper rich eutectic phases. In addition to, the effect of Sr on SDAS values in AlSi7Cu3 alloy has been examined and the obtained results indicate that Sr does not affect the SDAS as well the temperatures related to the initial reaction on the cooling curve. Such result is not in agreement with some published results [124].

To monitor the effect of Sr on solidification features, Sr has been added in the form of Al-Sr 10 master alloy to the AlSi7Cu3 melt. The average chemical composition of the alloys containing different Sr contents can be seen in Table 5-11.

The main method of assessing chemical modification of the silicon structure of the Al-Si-Cu alloy is to perform Optical Emission Spectroscopy analysis (OES). Quantification of the amount of strontium in the AlSiCu aluminium melt by OES analysis can give an actual strontium content, however, OES analysis does not assess the activity of strontium in a AlSiCu melt (i.e. how much strontium is available to actively convert acicular silicon particles to a more fibrous structure). Over time, strontium reacts with other elements in the melt and hence loses its potency as a modifier (i.e. it becomes inactive). Therefore, OES can not assess

the amount of active strontium (i.e. the strontium that has the potential to modify the silicon particles).

Table 5-11 Chemical composition of AlSi7Cu3 alloy containing different Sr contents

Alloy	Si	Fe	Cu	Mn	Mg	Zn	Ti	Sr, ppm
	wt %							
1A	7.25	0.22	3.59	0.42	0.22	0.85	0.15	1
2A								55
3A								83
4A								107
5A								143
6A								173
7A								210

An alternative method to determine the relative activity of chemical modifier is the determination of depression of eutectic Al-Si eutectic growth temperature, parameter via Thermal Analysis technique. Fig. 5-47 illustrates two representative cooling curves and corresponding microphotographs related to the Sr content of 1 ppm and 143 ppm in AlSi7Cu3 alloy. As it can be noticed from the Fig. 5-47 the additions of modifier leads to the depression of the nucleation and growth temperatures of main eutectic reaction on the cooling curve. The microphotographs presented in Fig. 5-47 show the effect of modification on the eutectic-silicon or other words the shape of eutectic silicon corresponding to the content of 1 and 143 ppm Sr. It can be added that addition of Sr in AlSi7Cu3 alloy does not affect on the initial part of cooling curves and in that way, the α -Al nucleation temperature, α -Al undercooling temperature, α -Al growth temperature and dendrite coherency temperature are kept constant for the whole concentration range of Sr examined in this work. The cooling curves overlap each other in that initial area (see Fig. 5-47). Unlike the other alloying elements examined in this study, the $T_{nuc}^{\alpha,den}(T_{liq})$ and $T_{coh}^{\alpha,den}(T_{DCP})$ are not affected by Sr additions:

$$T_{nuc}^{\alpha,den}(\text{AlSi7Cu3}) \neq f(\text{Sr}) \text{ } ^\circ\text{C} \quad (5-31)$$

$$T_{coh}^{\alpha,den}(\text{AlSi7Cu3}) \neq f(\text{Sr}) \text{ } ^\circ\text{C} \quad (5-32)$$

The increase of Sr content in AlSi7Cu3 alloy shifted the T_{sol} to lower levels. Fig. 5-47 indicates also that addition of Sr to AlSi7Cu3 melt alter $T_{E, nuc}^{Al-Cu}$ (T_{Al-Cu}).

As it is seen in Fig 5-48, the expecting effect of Sr on $T_{E, G}^{Al-Si}$ and depression of the Al-Si eutectic growth temperature, $\Delta T_{E, G}^{Al-Si}$ is confirmed on the AlSi7Cu3 alloy examined in this study. The increase of Sr from 1 to 210 ppm reduces $T_{E, G}^{Al-Si}$ about 10 °C. Such results are in very good agreement with the published papers [121-125]. At the same time depression of the Al-Si eutectic growth temperature increases 10 °C as the Sr content increase from 1 to 210 ppm.

The equations (5-33) and (5-34) express the correlation between $T_{E, G}^{Al-Si}$ and $\Delta T_{E, G}^{Al-Si}$ with Sr content, respectively. In Fig. 5-49 an additional effect of Sr addition regarding the effect on aluminum-silicon-copper eutectic nucleation temperature, $T_{E, NUC}^{Al-Cu}$ and quantity of Cu-bearing phase in AlSi7Cu3 alloy is presented. As it can be noticed, $T_{E, NUC}^{Al-Cu}$ temperature rises from 504.8 to 510.8°C when the strontium level increased from 1 to 210 ppm. It is also evident that the same Sr addition result in higher content of Cu-phase in AlSi7Cu3 alloys. In this case the quantity of Cu-bearing phases was determined as the total area of all present Cu-phases including “blocky” and eutectic phase. The quantity of these Cu – phases was not determined individually, although in the literature there is an indication that Sr addition leads to the higher quantity of blocky and lower quantity of eutectic Cu-phase [123]. The correlation equations (5-35) and (5-36) are the best fitted with the experimental results related to $T_{E, NUC}^{Al-Cu}$ and total fraction of Cu-bearing phases.

It was found that the addition of Sr considerably increases the end of solidification temperature from 479 to 491°C when strontium is increased from 1 to 210 ppm.

$$T_{E, G}^{Al-Si} = 0.0002 (Sr)^2 - 0.10 (Sr) + 563.7 \text{ °C} \quad R^2=0.97 \quad (5-33)$$

$$\Delta T_{E, G}^{Al-Si} = 0.0002 (Sr)^2 + 0.9 (Sr) - 0.6 \text{ °C} \quad R^2=0.97 \quad (5-34)$$

$$T_{E, G}^{Al-Si} = 1E-04(Sr)^2 + 0.01 + 504.8 \text{ °C} \quad R^2=0.99 \quad (5-35)$$

$$\text{Total \% Cu phases} = -5E-07(Sr)^3 + 0.002(Sr)^2 + 0.005 (Sr) + 3.3 \quad R^2=0.97 \quad (5-36)$$

In Fig. 5-50 it is shown effect of Sr addition on SDAS in AlSi7Cu3 alloy and it is obvious that SDAS values are not affected by Sr addition or in other words:

SDAS \neq f(Sr)

(5-37)

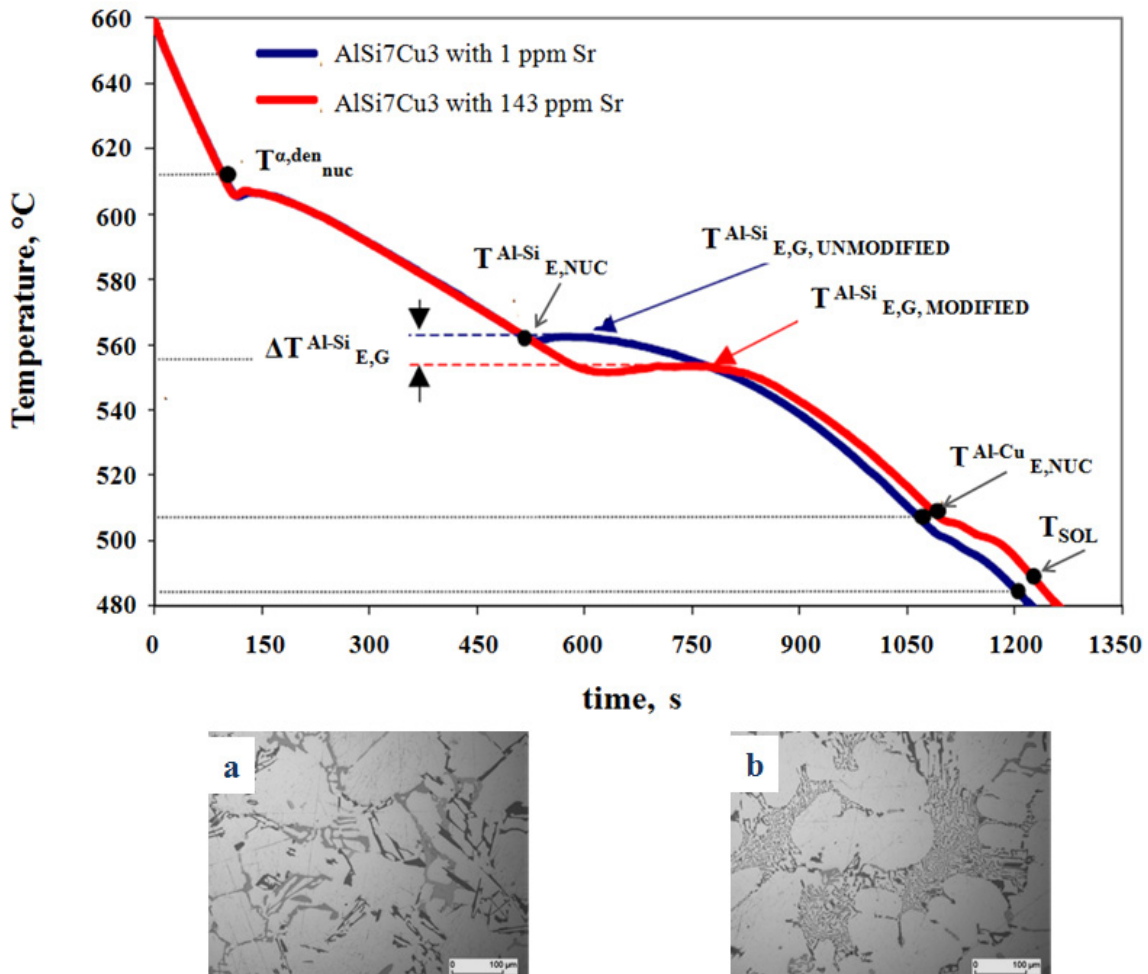


Fig. 5-47 Cooling curves and the corresponding microphotographs of AlSi7Cu3 alloy containing 1 and 143 ppm Sr

- a- Microphotograph of AlSi7Cu3 alloy containing 1 ppm Sr
 b- Microphotograph of AlSi7Cu3 alloy containing 143 ppm Sr

- $T_{E,G, UNMODIFIED}^{Al-Si}$ - Al-Si eutectic unmodified temperature is the maximum temperature that is achieved during the recalescence of the melt from the nucleation temperature without any addition of modifiers.
- $T_{E,G, MODIFIED}^{Al-Si}$ - Al-Si eutectic modified growth temperature is the maximum temperature after addition of modifiers (usually Al-10%Sr master alloy) that is achieved during nucleation temperature.
- $\Delta T_{E,G}^{Al-Si}$ - Depression of the Al-Si eutectic growth temperature, represents the temperature difference between the unmodified and modified Al-Si eutectic temperature.

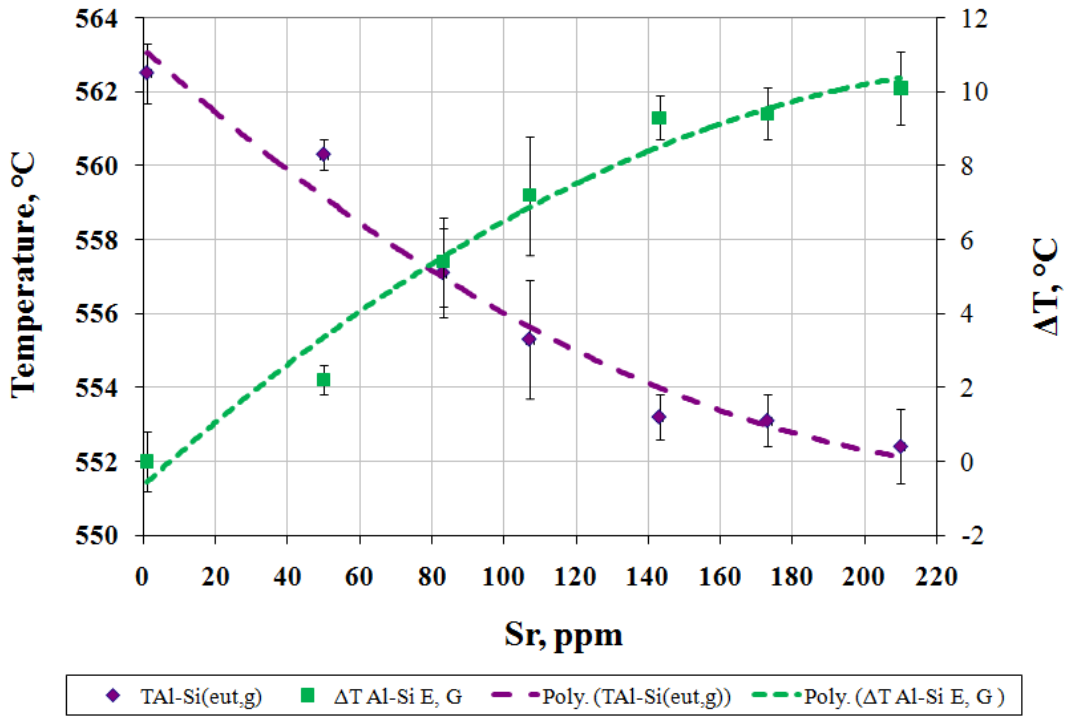


Fig. 5-48 Influence of Sr addition on the $T_{E,G}^{Al-Si}$ and $\Delta T_{E,G}^{Al-Si}$ in AlSi7Cu3 alloy

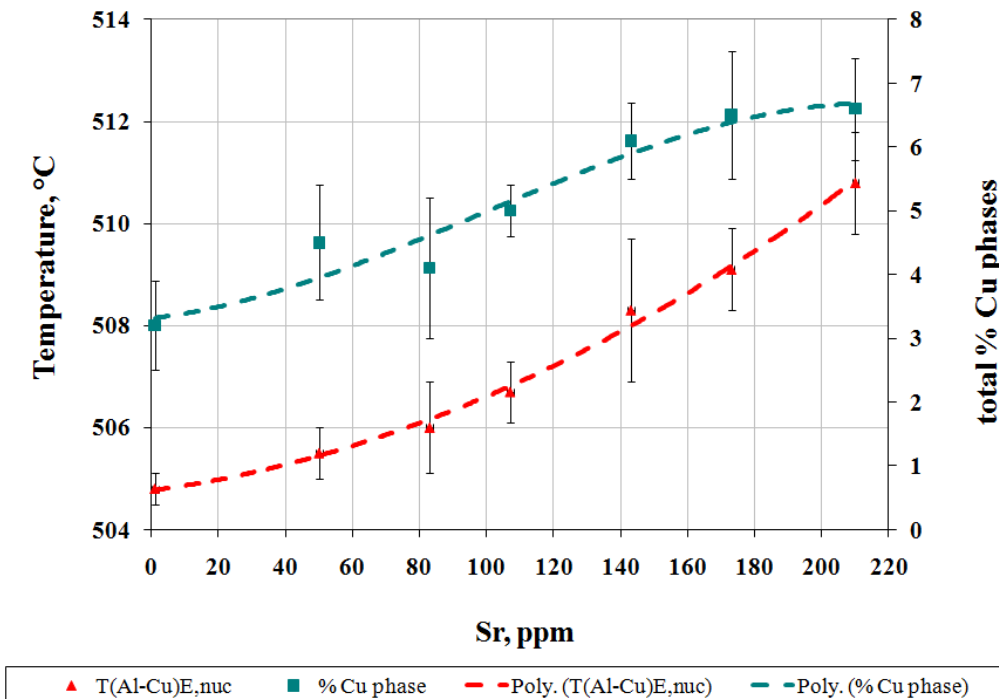


Fig.5-49 Influence of Sr addition on the $T_{E,NUC}^{Al-Cu}$ and total fraction of Cu-bearing phases in AlSi7Cu3 alloy

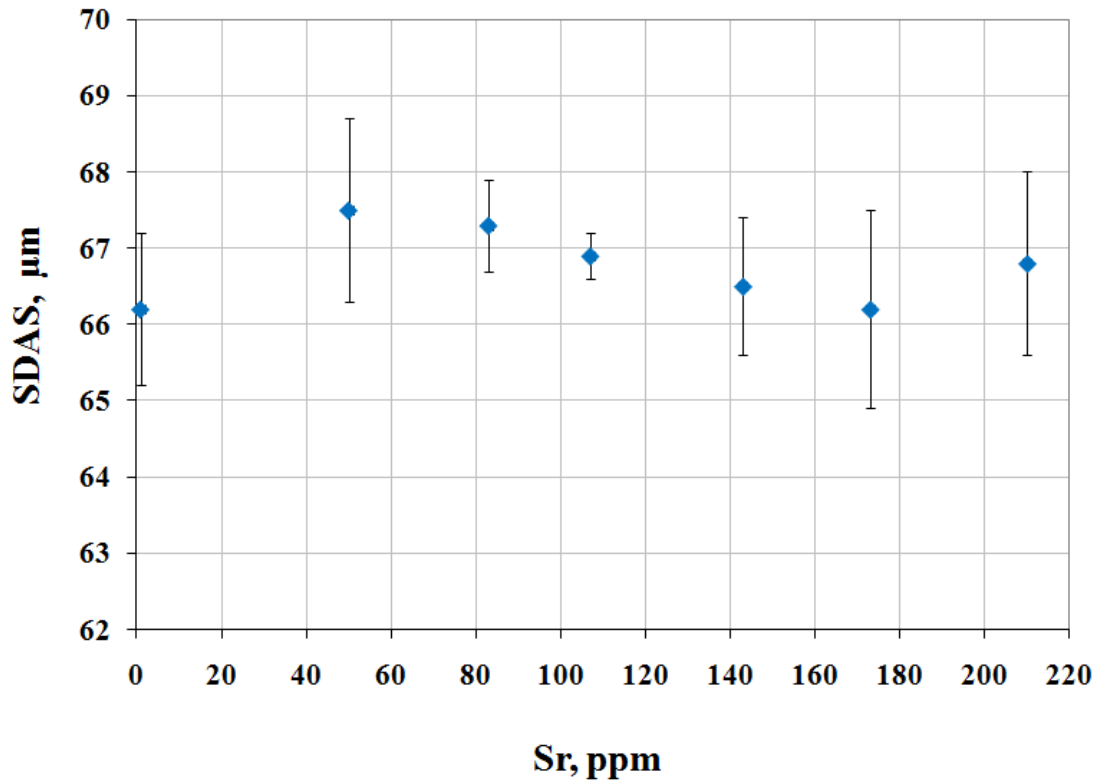


Fig. 5-50 Influence of Sr on the SDAS value in AlSi7Cu3 alloy

5.6. Comparative effect of different parameters

In this chapter the following graphs are presented as a summary of the results of this study. The effect of different alloying elements on the main solidification features is expressed versus the addition of 2 wt% of Si, 1 wt% of Cu, Zn and Mg, 0.01 wt% of Ti and 20 ppm of Sr.

The Fig. 5-51 reveals the effect of alloying elements on the T_{liq} temperature. The graphs clearly depicts that major alloying element possess the strongest impact on the T_{liq} temperature, where the addition of 2 wt% of Si (increase from 7 to 9 wt% Si) in the AlSiCu1 alloy contributes to the decrease of 17.5 °C. At the same time, the effect of 1 wt% Cu and 1 wt% of Mg addition is obvious. On the contrary, the addition of Sr has no effect on the T_{liq} temperature.

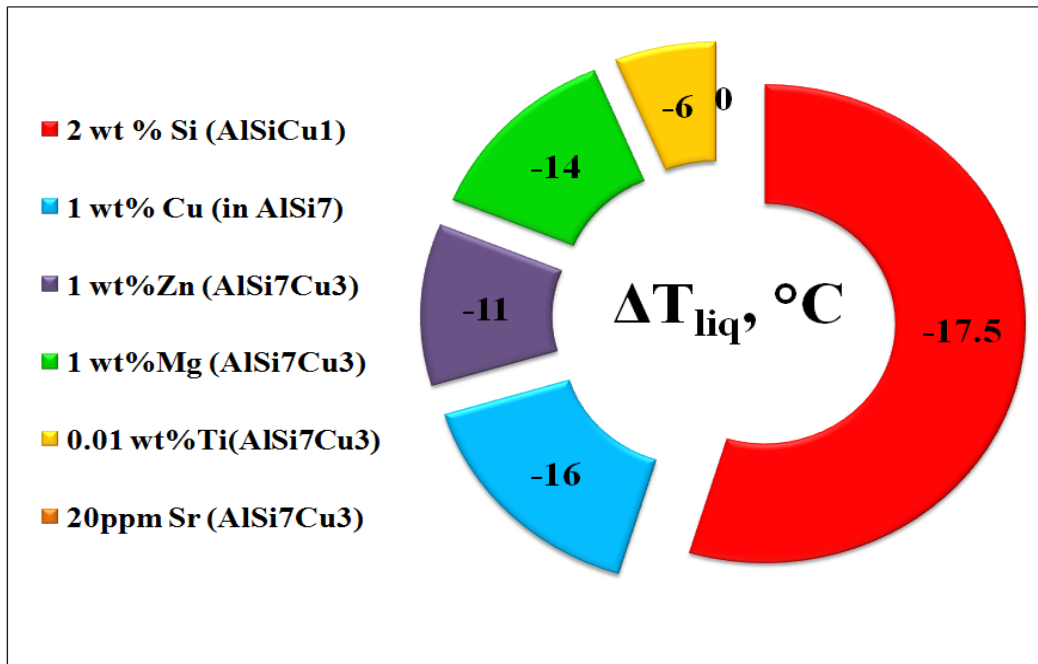


Fig. 5-51 The comparative effect of alloying elements on T_{liq} temperature

In Fig. 5-52 the comparative effect of alloying elements on T_{DCP} is presented. As in the previous case, the addition of Si shows also the dominant effect on T_{DCP} temperature that reaches the reduction of 15 °C with the addition of 2 wt% Si, but the addition of Sr has no effect on T_{DCP} .

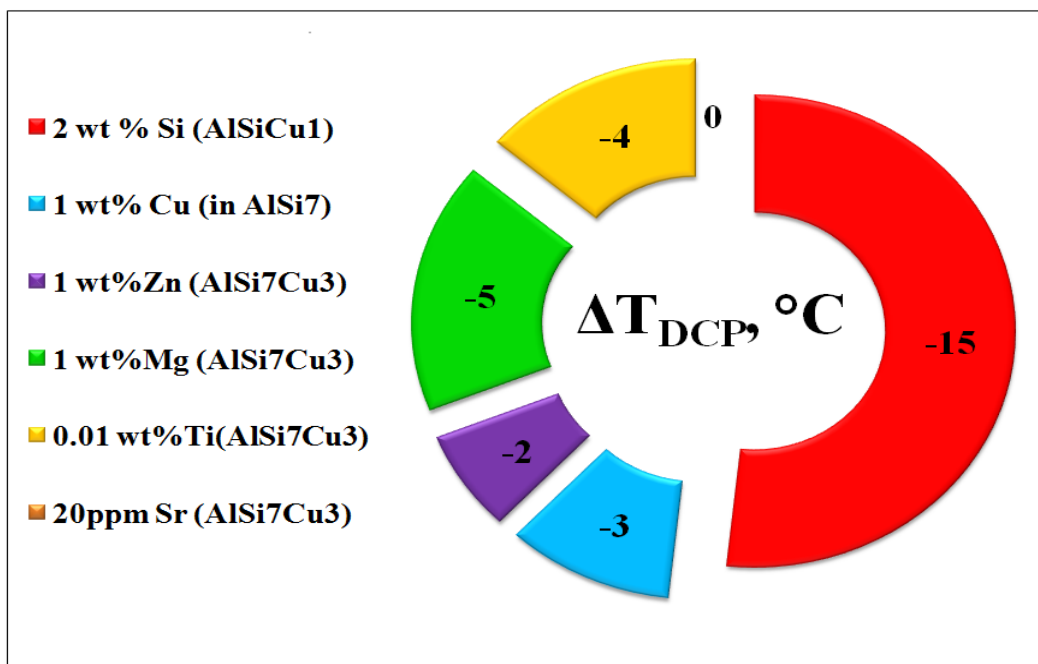


Fig. 5-52 The comparative effect of alloying elements on T_{DCP} temperature

The comparative effect of alloying elements on the T_{Al-Si} temperature is illustrated in Fig. 5-53. Beside the expected effect of Si addition on T_{Al-Si} temperature, it is seen surprising effect of Mg. The addition of 1 wt% Mg shows tremendous reduction of T_{Al-Si} temperature, 7 °C. The elements such as Zn and Ti has no effect on the T_{Al-Si} temperature. Taking into account the addition of only 20 ppm Sr to the basic alloy, it can be concluded that Sr decreases the T_{Al-Si} temperature all the same.

As it can be seen in Fig. 5-54, the comparative effect of alloying elements on T_{Al-Cu} temperature seems completely different as in the previous cases. It means that addition of the elements such as Sr, Mg, Cu and Zn leads to the increase of T_{Al-Cu} temperature. Among the mentioned alloying elements, the addition of 1 wt% Mg shows significant effect providing the increase of T_{Al-Cu} temperature about 5 °C. As in the case of T_{Al-Si} temperature, the same remark regarding Sr stands for T_{Al-Cu} temperature, but leading to the increase of T_{Al-Cu} temperature. The addition of titanium and zinc do not affect T_{Al-Cu} temperature.

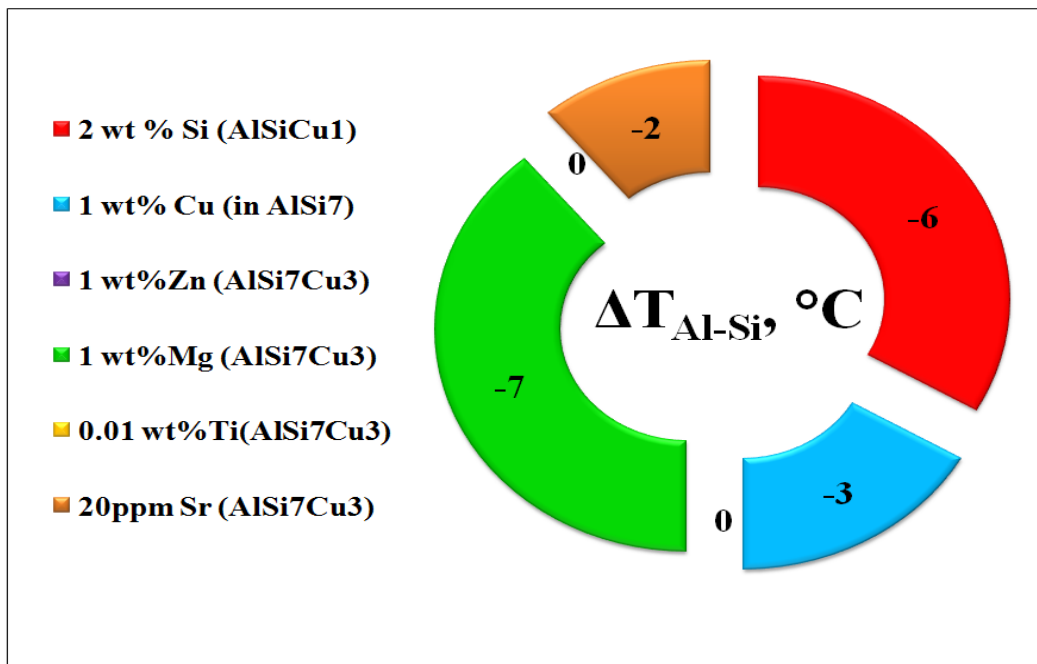


Fig. 5-53 The comparative effect of alloying elements on T_{Al-Si} temperature

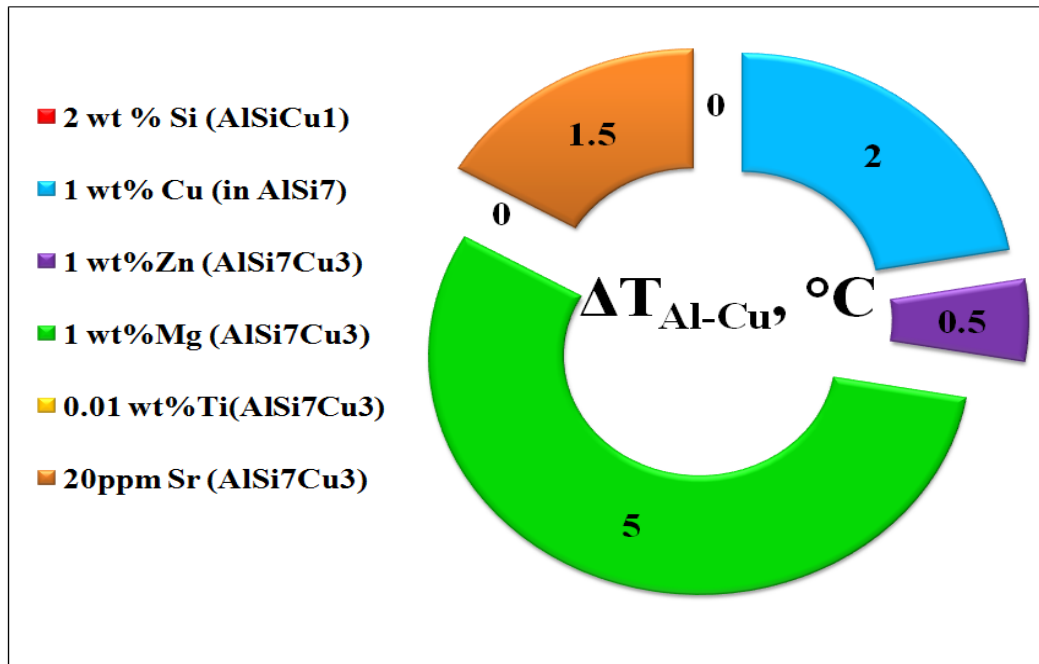


Fig. 5-54 The comparative effect of alloying elements on T_{Al-Cu} temperature

The summary effect of alloying elements on SDAS is presented in the Fig. 5-55. As it was expected and evidently seen on this graph the addition of 2 wt% Si contributes substantially to decrease of SDAS, 8.5 μm . Moreover, there is a remarkably contribution of Ti, which addition of 0.01 wt% enables the SDAS decrease of 8.5 μm . The elements such as Mg, Cu and Zn show lower impact on SDAS. As it was thought, Sr does not affect SDAS value.

The graph in Fig. 5-56 reveals the summary effect of mold temperature with and without water cooling in comparison to the pouring temperatures. As it was mentioned the reduction of both T_{mold} (from 350 to 250 °C) and T_{pour} temperatures (from 750 to 650 °C) was equal, 100 °C. It can be observed from Fig. 5-56 that among the casting parameters the strongest influence on SDAS has the pouring temperature providing the increase of SDAS of 6 μm . The decrease of the mold temperature without water cooling of the mold points out the similar reduction of SDAS value, while in the water cooling of the mold diminishes effect of mold temperature but it leads to the further decrease of SDAS.

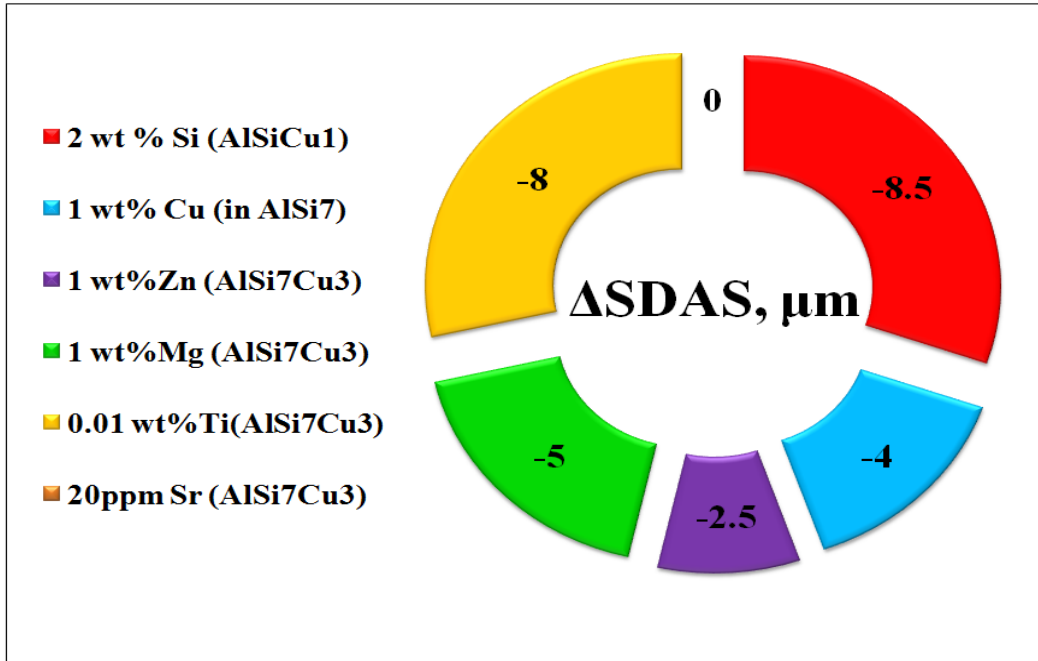


Fig. 5-55 The comparative effect of alloying elements on SDAS

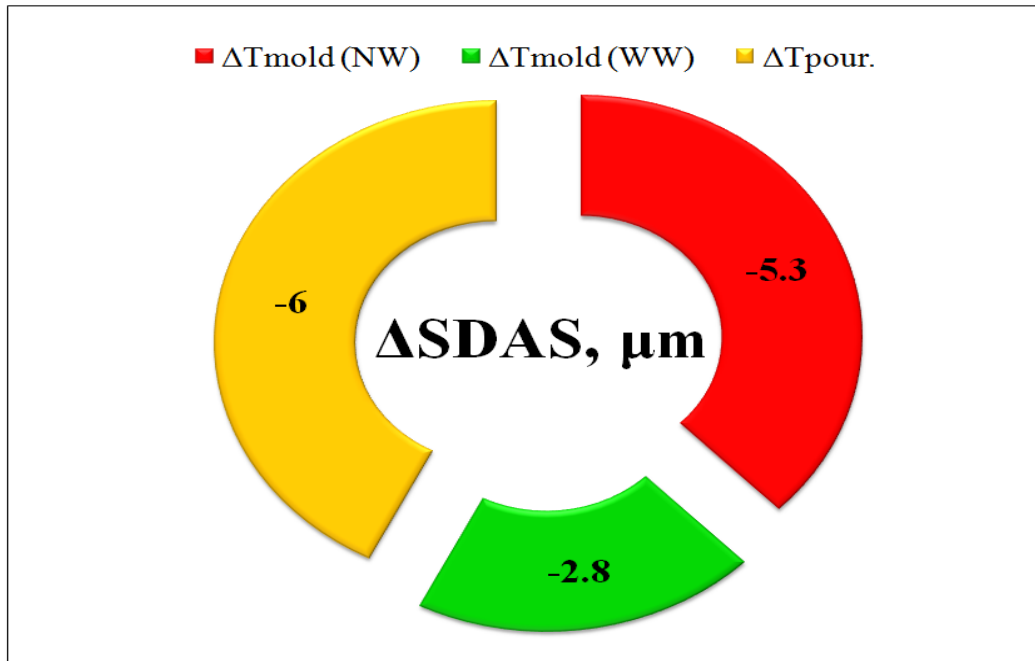


Fig. 5-56 The comparative effect of mold temperature and pouring temperature on SDAS

6. Conclusions

The results of the preliminary experiments confirmed that the solidification process as well as microstructure features in the complex shape castings are difficult to control and therefore to fulfil the stringent demand regarding the SDAS values. The AlSi7Cu3 cylinder head produced by tilt pouring gravity die casting process was taken in this study as an example to document the solidification behavior in the real casting with complex geometry. The relationship between the SDAS values and the cooling rates proves the suspected correlation extensively applied in the scientific works available in the literature.

The parameters affecting the solidification behavior of AlSi7Cu3 alloy were examined in this work with the special emphasis on the SDAS. Among the casting parameters, the effect of mold temperature with and without water cooling and the effect of pouring temperatures have been considered. As it was illustrated in Fig. 5-57, the reduction of pouring temperature, in the range permitted by alloy specification had a more direct and remarkable effect on SDAS decrease than reducing the mold temperature. The combined effect of mold temperature reduction and the water cooling of the mold wall enables to shorten the total solidification time as well to reach the finer values of SDAS. However, the impact of mold temperature reduction in the presence of water cooling of the mold wall has been slightly diminished (Fig. 5-13).

Although the effect of chemical composition of AlSiCu alloys has been overshadowed by the dominant impact of cooling rate and/or solidification time, the results of this study confirm that even slight changes in the concentration might provide a variation in the reaction temperature and the resultant microstructure. The individual impact of alloying elements, Si, Cu, Mg, Ti, Zn and Sr on the solidification behavior of AlSi7Cu3 alloy has been assessed and the comparative effect of different alloying element on the main solidification features was illustrated by the ring graphs in the Fig. (5-52) – (5-57).

It was found that addition of 2 wt% Si, the major alloying element enables the most pronounced decrease of the T_{liq} and T_{DCP} , temperatures. The addition of other alloying elements also showed the significant decrease of T_{liq} temperature. Comparing the Ti additions with additions of other alloying elements except Sr, it might be said that effect of Ti should be

100 or 200 times multiple and then to be compared with other alloying elements. Therefore, it could be after concluded that Ti possess the strongest impact on the T_{liq} and T_{DCP} temperatures. Concerning the effect of alloying elements on the SDAS, a similar situation was noticed. In addition, Si has provided the highest reduction of SDAS values (8.5 μm). The addition of 1 wt% of the alloying elements such as Mg, Cu and Zn contributes to a noticeable decrease of SDAS (5, 4, and 2.5 μm). However, it could be also claimed in the case of SDAS value that the effect of Ti on SDAS in respect to its content in the basic alloy was the strongest. Unlike the other alloying elements, the contribution of Sr to the change of T_{liq} and T_{DCP} temperatures and SDAS values was not detected in this study.

Concerning the effect of different alloying elements on the precipitation temperatures of the major, T_{Al-Si} and minor eutectic, T_{Al-Cu} a tremendous effect of Mg has been found. The addition of 1 wt % of Mg led to a significant decrease of T_{Al-Si} about 7 °C. As it was expected, the contribution of Si addition to T_{Al-Si} was quite high. From the same point of view as in the case of Ti, the contribution of Sr to the T_{Al-Si} and T_{Al-Cu} temperatures can be considered the most tremendous. The addition of Zn and Ti in AlSi7Cu3 alloys did not cause any change of T_{Al-Si} and T_{Al-Cu} .

According to the results of this study, the kinetic of dendrite growth versus the chemical composition might be rather interpreted by a novel kinetic parameter, $\Delta\tau^*$ then conventional t_f . As a confirmation of this remark, the mathematical model, commonly used to describe the relationship between the SDAS and solidification time, has been verified. According to the verification of the model, it might be emphasis, that $\Delta\tau^*$ much better correlate to SDAS then the total solidification time.

The findings in this study could have important implications for Al-Si alloys in particular, due to their wide spread applications in the automotive industry. That is not needed to emphasize that cooling rate has the leading effect on the solidification behavior and resultant size of SDAS. However, it has been shown that the effect of chemical composition is significant and can not be neglected. Therefore, the variation of the chemical composition could be used for fine tuning in order to reach the desired size of the SDAS.

7. Literature

- [1] J. G Kaufman, E.L. Rooy, Aluminium Alloy Castings Properties, Processes and Applications, ASM International, Materials Park, USA, 2004
- [2] I.J. Polmear, Light Metals, E. Arnold Publishers, London, UK, 1981
- [3] J. E. Gruzleski, B. M. Closset, Treatment of liquid Al-Si alloys, AFS, Inc., 1990
- [4] Aluminium Federation, The Properties of Aluminium and Its Alloys, ALFED UK, 1983
- [5] J. Datta, Ed. Aluminium Schlüssel: Key to Aluminum Alloy: 6th ed. Aluminum Verlag, Düsseldorf, Germany, 2002
- [6] G.K. Sigworth, F. Dehart, Recent Developments in the High Strength Aluminium-Copper Casting Alloys A206, AFS Transactions 111, 2003, 341-354
- [7] C.H. Cáceres, C.J. Davidson, J. R. Griffiths, Q.G. Wang, The effect of Mg on the microstructure and Mechanical behaviour of Al-Si-Mg Casting Alloys, Metallurgical Material Transaction, 30A, 1999, 2611-2618
- [8] K. Müller, W. Reif, Einfluß von Begleit- und Spurenelementen auf die Kornfeinung hochsilizium Al-Si-Guslegierungen auf Reinstbasis, Metall 51, 1-2, 1997, 25-32
- [9] K.G. Basavakumar, P.G. Mukunda, M. Chakraborty, Influence of grain refinement and modification on microstructure and mechanical properties of Al-7Si and Al-7Si-2.5Cu cast alloys, Materials Characterization, 59, 2008, 283 – 289
- [10] E. Maier, G. Lang, Herstellung der Aluminium-Gußlegierung AlSi7Mg unter Berücksichtigung ihrer Veredelung mit Na, Sr und Sb, Aluminium 61. Jahrgang, 12, 1985, 193-201

- [11] S.G. Shabestari, S. Ghodrat, Assessment of modification and formation of intermetallic compounds in aluminum alloy using thermal analysis, *Materials Science and Engineering A* 467, 2007, 150–158
- [12] Perspektiven-Geschäftsbericht 2007/2008, Wirtschaftsvereinigung e.V. Metalle, Berlin, 2008
- [13] Ch. Schmitz, Handbook of Aluminium Recycling-Fundamentals Mechanical Preparation Metallurgical Processing Plant Design, Vulkan-Verlag GmbH, 2006
- [14] R. C. Creese, Introduction to manufacturing process and materials, Marcel Dekker Inc., 1999.
- [15] L. Pavlak, Effect of filling conditions on the quality of cast aluminum cylinder heads, *Metalurgija - Journal of Metallurgy*, 14, 2008, 31-39
- [16] R. Bähr, F.Mnich, H.C. Saewert, D. Fiedler, Neue Wege in der virtuellen Produktenentwicklung Praxisbeispiele, Gießtechnik im Motorenbau - Anforderungen der Automobilindustrie, Tagung Magdeburg, 1.-2.2.2005, VDI-Bericht 1830, Düsseldorf: VDI Verl., 2005, 199 – 208
- [17] J. Pavlovic-Krstic, R. Bähr, G. Krstic, New Casting Technologies and prediction of casting properties using advanced computational simulation technology, International PhD Foundry Conference, June 1.-3. Brno, 2009, 117-125
- [18] H.C. Saewert, F. Mnich, E. Krebs, R. Bähr, NEMAK Dynamic Casting System (NDCS) - Wechselbeziehungen zwischen den Anforderungen an Aluminiumgussteile und der Entwicklung von Gießverfahren, *Druckguss*, 2007, 13-21
- [19] R. Molina, M. Leghissa, L. Mastrogiacomo, New developments in high performance cylinder heads: Application of LHIP and Split Cylinder Head Concept, *Metallurgical Science and Technology*, 2008, 2-8
- [20] M.J. Nunney, Light and heavy vehicle technology, The Bath Press England, 2003

- [21] ASM Metals Handbook, 10th ed., vol. 15: Casting, ASM-Metals Park, Ohio, 1990
- [22] K.E. Höner, J. Grosse, Mechanische Eigenschaften und Bruchverhalten von Aluminium-Silicium-Gußlegierungen, Gieserei 78, 18, 1991, 655-661
- [23] H.M. Tensi, R. Rösch, C. Xu, S. Spaic, Beeinflussung von Gefüge und Festigkeit einer technischen AlSi-Gußlegierung, Aluminium 69, 7, 1993, 634-640
- [24] B. Lenczowski, H. Koch, K. Eigenfeld, B. Plege, A. Franke, S. Klan, Neue Entwicklung auf dem Gebiet der warmfesten Aluminium-Gußwerkstoffe, Gießerei, 91, 2004, 32-38
- [25] F. Langmayr, F. Zieher, Thermomechanik in Zylinderköpfen, Ventiltrieb und Zylinderkopf, VDI Berichte 1813, VDI Verlag GmbH, Düsseldorf, 2004, 227-243
- [26] S. Trampert, F. Maassen, Zylinderköpfe für hohe Spitzendrücke und Literleistungen, Ventiltrieb und Zylinderkopf, VDI-Berichte 1813, VDI Verlag GmbH, Düsseldorf, 2004, 203-216
- [27] J. Campbell, Castings, 2nd ed., Butterworth-Heinemann, Oxford, 2003
- [28] R. Colás, A. Rodríguez, J. Talamantes, S. Valtierra, Solidification analysis of aluminium engine block, Int. J. Cast Met. Res., 17, 2004, 332–338
- [29] J. B. Heywood, Internal Combustion Engine Fundamentals, McGraw-Hill Int. Ed., New York, 1989
- [30] P. M. Norris, M.C. Hastings, W.J. Wepfer, An experimental investigation of liquid coolant heat transfer in a diesel engine, International Journal of Experimental Heat Transfer, Thermodynamics and Fluid Mechanics, 7, 1994, 43–51
- [31] R. B. Gundlach, B. Ross, A. Hetke, S. Valtierra, J. F. Mojica, Thermal fatigue resistance of hypoeutectic aluminum-silicon castings, AFS Transactions, 104, 1994, 205–211

- [32] J. Campbell, R.A.Harding, Casting Technology, In TALAT 2.0 cd-rom, EAAA, Bruxelles, 1994
- [33] T. Beck, I. Henne, D. Loehe, Materials Science and Engineering A, 483–484, 2008, 382–386
- [34] L. Bäckerud, G. Chai, J. Tamminen, Solidification Characteristics of Aluminum Alloys, Vol.2: Foundry Alloys, AFS/SKANALUMINUM, 1990
- [35] R. Minichmayr, W. Eichseder, Lebensdauerberechnung von Gussbauteilen unter Berücksichtigung des lokalen Dendritenarmabstandes und der Porosität, Gießerei 90, 5, 2003, 70-75
- [36] I. Henne, T. Beck, D. Löhe, Modellierung der Schädigungsentwicklung thermisch-mechanisch hochbeanspruchter Motorbauteile und Ermittlung geeigneter Werkstoffkennwerte, 4. Arbeitskreissitzung zum FVV-Vorhaben, 819, 2004
- [37] B. Zhang, M. Garro, C. Tagliano, Dendrite Arm Spacing in Aluminium Alloy Cylinder Heads produced by gravity semi-permanent mold, Metallurgical science and Technology, 21, 1, 2003, 3-9
- [38] J. Pavlovic, M. Djurdjevic, O. Bouska, R. Bähr, The influence of the chemical composition and cooling conditions on the secondary dendrite arm spacing in Al-Si cylinder head, 44th Foundry Days and 4th International PhD Foundry Conference, Brno, Czech Republic, 16-17. October, 2007, 12-22
- [39] H. Sehitoglu, Thermal and thermomechanical fatigue of structural alloys. ASM Handbook – Fatigue and fracture, Ohio, 1996
- [40] J.J. Thomas, L. Verger, A. Bignonnet, E. Charkaluk, Thermomechanical design in the automotive industry, Fatigue Fracture Engineering Material Structure, 27, 2004, 887–95

- [41] A. Wickberg, G. Gustafson, LE. Larson, Microstructural effects on the fatigue properties of a cast AlSi7Mg alloy, SAE Transaction, 93, 1984, 728–35
- [42] O. Vorren, J.E. Evensen TB Pedersen, Microstructure and mechanical properties of AlSi(Mg) casting alloys. AFS Trans, 92, 1984, 459–66
- [43] ASM Handbook, Vol. 2, Properties and Selection: Nonferrous Alloys and Special-Purpose Materials, ASM International, 1996
- [44] L. Ratke, Utilization of Space Today and Tomorrow, Space as a Laboratory-Part 5, Springer Berlin Heidelberg, 2006
- [45] X. Zhu, A. Shyam, J.W. Jones, H. Mayer, J.V. Lasecki, J.E. Allison, Effects of microstructure and temperature on fatigue behavior of E319-T7 cast aluminum alloy in very long life cycles International Journal of Fatigue, 28, 2006, 1566–1571
- [46] V. Firouzdor, M. Rajabi, E. Nejati, F. Khomamizadeh, Effect of microstructural constituents on the thermal fatigue life of A319 aluminum alloy, Materials Science and Engineering A 454–455, 2007, 528–535
- [47] F. Bonollo, R. Tovo, TALAT Lecture 1254 - Fatigue in Al casting alloys: metallurgical aspects, EAA - European Aluminium Association, 1999
- [48] R. N. Grugel, Secondary and tertiary dendrite arm spacing relationships in directionally solidified Al-Si alloys, Journal of Material Science, 28, 1993, 677-683
- [49] N. J. Whisler, T. Z. Kattamis, Dendritic Coarsening during Solidification, Journal of Crystal Growth 15, 1972, 20-24
- [50] U. Feurer, Quality Control of Engineering Alloys and the Role of Metals Science, H. Nieswaag and J.W. Schut, eds., Delft University of Technology, Delft, The Netherlands, 1977, 131-145
- [51] M.C. Flemings, Solidification Processing, McGraw-Hill, New York, America, 1974

- [52] L. Bäckerud, E. Krol, J. Tamminen, Solidification Characteristic of Aluminium alloys, Volume 1, Scanaluminium, Norway, 1986
- [53] W. Kurz, D.J.Fisher, Fundamentals of solidification, Trans Tech SA, Switzerland, 1989
- [54] W.W. Mullins, R.F. Sekerka, Morphological Stability of a Particle Growing by Diffusion or Heat Flow, *Journal of Applied Physics*, 34, 1963, 323–329
- [55] R. Trivedi, W. Kurz, Dendritic Growth, *International Materials Review*, 39, 1994, 49–74
- [56] M.E. Glicksman, M.B. Koss, Dendritic Growth Velocities in Microgravity, *Physics Review Letters*, 73(4), 1994, 573–576
- [57] S.H. Han, R. Trivedi, Primary Spacing Selection in Directionally Solidified Alloys, *Acta Metallurgica*, 42, 1994, 25–41
- [58] G.L. Ding, W. Huang, X. Lin, Y. Zhou, Prediction of Average Spacing for Constrained Cellular/Dendritic Growth, *Journal of Crystal Growth*, 177, 1997, 281–288
- [59] L. Makkonen, Spacing in Solidification of Dendritic Arrays, *Journal of Crystal Growth*, 208, 2000, 772–778
- [60] J.A. Warren, J.S. Langer, Prediction of Dendritic Spacings in a Directional-Solidification Experiment, *Physics Review E*, 1993, 47, 2702–2712
- [61] S.Z. Lu, J.D. Hunt, Numerical Modelling of Cellular and Dendritic Array Growth: Spacing and Structure Predictions, *Material Science Engineering A*, 1993, 173, 79–83
- [62] R. Trivedi, Interdendritic Spacing: Part II. A Comparison of Theory and Experiment, *Metallurgical Transaction*, 1984, 15A, 977–982

- [63] M. Asta, C. Beckermann, A. Karma, W. Kurz, R. Napolitano, M. Plapp, G. Purdy, M. Rappaz, R. Trivedi, Solidification microstructures and solid-state parallels: Recent developments, future directions, *Acta Materialia*, 57, 2008, 941-971
- [64] <http://fluid.ippt.gov.pl/metro/CDROM-PL/kursy/...en/metro-ippt-lecture03.pdf>
- [65] B. Zhang, M. Garro, C. Tagliano, Dendrite arm spacing in aluminium alloy cylinder heads produced by gravity semi-permanent mold, *Metallurgical Science and Technology*, 21, 2003, 3-9
- [66] H. Banghong Hu, L. Hang, Comparison of effects of master alloys containing titanium and/or boron on the grain size and dendrite arm spacing of DIN226S aluminium alloy, *Journal of materials science letters*, 16, 1997, 1750±1752
- [67] L.Yu, X.Liu, Z. Wang, X. Bian, Grain refinement of A356 alloy by AlTiC/AlTiB master alloys, *Journal of materials science*, 40, 2005, 3865-3867
- [68] L. Liu, A.M. Samuel, F.H. Samuel, H.W. Doty, S. Valtierra, Characteristics of α -dendritic and eutectic structures in Sr-treated Al-Si casting alloys, *Journal of material science* 38, 2004, 1-10
- [69] R. Bähr, M. Djurdjevic, J. Pavlovic, Control and Prediction of Casting Characteristics Using Thermal Analysis Techniques, *Machine Manufacturing*, 1, 2009, 26-30
- [70] L. Ananthanarayanan, J. E. Gruzleski, Thermal Analysis Studies on the Effect of Cooling Rate on the Microstructure of the 319 Aluminium Alloy, *AFS Transactions*, 141, 1992, 383-391
- [71] D.M. Stefanescu, G. Upadhyay, D. Bandyopaadhyay, Heat Transfer-Solidification Kinetics Modeling of Solidification of Castings, *Metallurgical Transactions A*, 2A, 1990, 997-1005

- [72] M.B. Djurdjevic, R. Hasenbusch, J. H. Sokolowski, Assessment of the Hydrogen Level in 319 Aluminium Alloy Melt Using the Thermal Analysis Technique, TMS Conference, Seattle, 1-8, February, 2002
- [73] H. Fredriksson, U. Åkerlind, Materials Processing During Casting, John Wiley & Sons, Ltd. 2006
- [74] T. Stockwell, NSERC/Ford/University of Windsor Industrial Research Chair, Experimental Results, Unpublished Report, 1997
- [75] L. Arnberg, L. Bäckerud, G. Chai, Solidification Characteristics of Aluminium Alloys, Vol. 3: Dendrite Coherency, AFS, Des Plaines, 1996
- [76] G. Chai, Dendrite Coherency During Equiaxed Solidification in Aluminum Alloys, Ph.D. Thesis, U. of Stockholm, Sweden, 1994
- [77] R.C Zamarripa, J.A. Ramos-Salas, J. Talamantes-Silva, S.Valtierra, R. Calas, Determination of the Dendrite Coherency Point during Solidification by means of Thermal Diffusivity Analysis, Metallurgical and Material Transaction A, 38A, 2007, 1875-79
- [78] D.A. Spencer, R. Mehrabian, M.C. Flemings, Rheological Behavior of Sn-15 Pct Pb in the Crystallization Rang, Metallurgical Transactions, Vol. 3, 1972, 1925-1932
- [79] L. Arnberg, G. Chai, L. Backend, Determination of Dendritic Coherency in Solidification Melts by Rheological Measurements, Material Science Engineering A173, 1993, 101-103
- [80] G. Chai, L. Bäckerud, T. Rolland, L. Arnberg, Dendrite Coherency During Equiaxed Solidification in Binary Aluminum Alloys, Metallurgical and Material Transaction A, 26A, 1995, 965-970

- [81] M.B. Djurdjevic, W. T. Kierkus, R. E. Liliac, J. H. Sokolowski, "Extended Analysis of Cooling Curves", 41th Annual Conference of Metallurgists of CIM, 2002
- [82] M. B. Djurdjevic, W. T. Kierkus, J. H. Sokolowski, 40th Annual Conference of Metallurgists of CIM, 2001
- [83] N. Veldman, A. Dahle, D. St. John, Die Casting & Tooling Technology Conference, 22-25 June, Melbourne, Australia, 1997
- [84] D. Emad, L. V. Whiting, S. Nafisi, R. Ghomashchi, Application of Thermal Analysis in quality control of solidification processes, Journal of Thermal Analysis and Calorimetry, 81, 2005, 235–242
- [85] N. Veldman, A. Dahl, D. St. John, L. Arnberg, Metallurgical and Material Transaction A, 32A, 2001, 147-155
- [86] S. Gowri, F.H. Samuel, Effect of Alloying Elements on the Solidification Characteristics and Microstructure of Al-Si-Cu-Mg-Fe 380 Alloy, Metallurgical and materials Transaction A, 25A, 1994, 437-449
- [87] J. Cho, X. Yan, C.R. Lopper, Microsegregation of copper in cast aluminium alloys, AFS Transaction, 124, 2003, 1-17
- [88] S.S. Sreeja Kumari, R.M. Pillai, T.P.D. Rajan, B.C. Pai, Effects of individual and combined additions of Be, Mn, Ca and Sr on the solidification behaviour, structure and mechanical properties of Al-7Si-0.3Mg-0.8Fe alloy, Materials Science and Engineering A 460–461, 2007, 561–573
- [89] J.A.E. Bell, W.C. Winegard, Dendrite Spacing in Tin-Lead Alloys, Journal Institute of Metals, 93, 1963, 357–359
- [90] S.H. Han, R. Trivedi, Primary Spacing Selection in Directionally Solidified Alloys, Acta Metallurgica, 42, 1994, 25–41

- [91] W. W. Mullins, R. F. Sekerka, On the Thermodynamics of Crystalline Solids, *Journal of Chemical Physics*, 82, 1985, 5192-5202
- [92] G.L. Ding, W. Huang, X. Lin, Y. Zhou, Prediction of Average Spacing for Constrained Cellular/Dendritic Growth, *Journal of Crystal Growth*, 177, 1997, 281–288
- [93] J.A. Warren, Ph.D. thesis, University of California, Santa Barbara, 1992
- [94] N. Al-Rawahi, G. Tryggvason, Numerical Simulation of Dendritic Solidification with Convection: Two-Dimensional Geometry, *Journal of Computational Physics* 180, 2002, 471–496
- [95] J.D. Hunt, A Numerical Analysis of Dendritic and Cellular Growth of a Pure Material Investigating the Transition from Array to Isolated Growth, *Acta Metallurgica*, 39, 1991, 2117–2133
- [96] S.Z. Lu, J.D. Hunt, Numerical Modelling Dendritic Array Growth: Spacing and Structure Predictions, *Metallurgical Transaction A*, 27A, 1996, 611–623
- [97] M.H. Burden, J.D. Hunt, Cellular and Dendritic Growth II, *Journal of Crystal Growth*, 22, 1974, 109–116
- [98] J.S. Langer, H. Müller-Krumbhaar, Theory of Dendritic Growth I- Elements of a Stability Analysis, *Acta Metallurgica*, 26, 1978, 1681–1687
- [99] V. Laxmanan, Dendritic Solidification-I. Analysis of Current Theories and Models, *Acta Metallurgica*, 33, 1985, 1023–1035
- [100] J.D. Hunt, *Solidification and Casting of Metals*, Metal Society, London, 1979
- [101] W. Kurz, D.J. Fisher, Dendritic Growth and Limit of Stability Tip Radius and Spacing, *Acta Metallurgica*, 29, 1981, 11–20

- [102] R. Trivedi, Interdendritic Spacing: Part II. A Comparison of Theory and Experiment, *Metallurgical Transaction*, 15A, 1984, 977–982
- [103] D.G McCartney, J.D. Hunt, Measurement of Cell and Primary Dendrite Arm Spacings in Directionally Solidified Aluminium Alloys, *Acta Metallurgica*, 29A, 1981, 1851–1863
- [104] D.G. McCartney, Ph.D. Thesis, Oxford University, 1981, 95
- [105] T. Okamoto, K. Kishitake, I. Bessho, Dendritic structure in unidirectionally solidified cyclohexanol, *Journal of Crystal Growth* 29, 1975, 131-136
- [106] C.T. Rios, R. Caram, Primary dendrite spacing as a function of directional solidification parameters in an Al-Si-Cu alloy, *Journal of Crystal Growth* 174, 1997, 65-69
- [107] S. Zajac, B. Bengtsson, Ch. Jönsson, Influence of cooling after homogenization and reheating to extrusion on extrudability and final properties of AA 6063 and AA 6082 alloys, *Materials Science Forum* 396-402, 2002, 399-404
- [108] C.H. Caceres, M.B. Djurdjevic, T.J. Stockwell, J.H Sokolowski, The Effect of Cu Content on the Level of Microporosity in Al-Si-Cu-Mg Casting Alloys, *Scripta Materialia*, Vol. 40, 1999, 631-637
- [109] H.W. Doty, A.M. Samuel, F. H. Samuel, Factors Controlling the Type and Morphology of Cu-Containing Phases in the 319 Aluminum Alloy, 100th AFS Casting Congress, Philadelphia, Pennsylvania, USA, April 20-23, 1996, 1-30
- [110] M. Djurdjevic, T. Stockwell., J. Sokolowski, J., The Effect of Strontium on the Microstructure of the Aluminum-Si and Aluminum-Cu Eutectics in the 319 Aluminum Alloy, *International Journal of Cast Metals Research*, 12, 1999, 67-73

- [111] G. Mrówka-Nowotnik, J. Sieniawski, M. Wierzbińska, Intermetallic phase particles in 6082 aluminium alloy, Archives of Materials Science and Engineering, Vol 28, 2007, 69-76
- [112] B. McClory, P. Crepeau, I. Mashal, Integration von Prozess- und Struktursimulationen bei Gussteilen, 16. Aachener Kolloquium Fahrzeug- und Motorentechnik 2007, 1219-1240
- [113] Srinivasan, U.T.S. Pillai, B.C. Pai, Effect of pouring temperature on the microstructure and the mechanical properties of low pressure sand cast LM25 alloy, International Journal of Microstructure and Materials Properties, 2, 2006, 139-148
- [114] Zahra, C.Y. Zahra, R. Ciach, Contribution to the study of the Al-Zn Phase Diagram, Journal of Thermal Analysis, Vol 26, 1983, 303-307
- [115] L. Heusler, W. Schneider, Influence of alloying elements on the thermal analysis results of Al-Si cast alloys, Journal of Light Metals 2, 2002, 17-26
- [116] X. G. Chen, Dissertation: Kristallisation des AlSi-Eutektikums und Anwendung der thermischen Analyse zur Kontrolle der Veredelung, RWTH Aachen, 1991
- [117] D. Dünkelmann, Thermoanalyse von Aluminium-Schmelzen mit systematischer Dokumentation, Giesserei 82, 18, 1995, 678- 681
- [118] H.R. Ammar, C. Moreau, A.M. Samuel, F.H. Samuel, H.W. Doty, Influences of alloying elements, solution treatment time and quenching media on quality indices of 413-type Al-Si casting alloys, Materials Science and Engineering A, 489 (1-2), 2008, 426-439
- [119] M. Djurdjevic, J Pavlovic, G. Byczynski, Der Einfluss von Hauptlegierungselementen und Kornfeinern auf den sekundären Dendritenarmabstand der AlSiCu Legierung, Praktische Metallographie, 2, 2009, 97- 114

- [120] M. Djurdjevic, G. Byczynski, C. Schechowiak, H. Stieler, J. Pavlovic, Quantifizierung des Einflusses von Strontium auf den Erstarrungsweg der Aluminium-Silicium-Kupfer-Legierungen mit dem Thermoanalyseverfahren, *Praktische Metallographie*, 3, 2009, 137-152
- [121] M. Castro-Roman, J.J. Montes-Rodriguez, M. Herrera-Trejo, Strontium Effect on the Solidification Path of a 319 Type Aluminum Alloy, *World Foundry Congress*, 4-7 June 2006, Harrogate, UK, 1-10
- [122] F. Lasagni, A. Lasagni, C. Holzapfel, F. Mücklich, H. P. Degischer, Three Dimensional Characterization of Unmodified and Sr-Modified Al-Si Eutectics by FIB and FIB EDX Tomography, *Advanced Engineering Materials*, 8, 2006, 719-723
- [123] Z. Li, A. M. Samuel, F. H. Samuel, C. Ravindran, S. Valtierra, H. W. Doty, Einflußfaktoren auf die Auflösung der CuAl₂-Phase in der Legierung 319, *GIESSEREI –PRAXIS*, 3, 2004, 99-108
- [124] A.K. Prasada Rao, K. Das, B.S. Murty, M. Chakraborty, Microstructural features of as-cast A356 alloy inoculated with Sr, Sb modifiers and Al–Ti–C grain refiner simultaneously, *Materials Letters* 62, 2008, 273–275
- [125] S.G. Shabestari, S. Ghodrati, Assessment of modification and formation of intermetallic compounds in aluminum alloy using thermal analysis, *Materials Science and Engineering A* 467, 2007, 150–158

8. List of tables and figures

List of tables:

Table 3-1 Solid solubility of elements in aluminum

Table 3-2 Classification of Casting Aluminum Alloys (Aluminum Association)

Table 3-3 List of characteristic temperatures with corresponding symbols

Table 4-1 Standard chemical composition of the basic alloy AlSi7Cu3

Table 4-2 Terms relevant for evaluation of SDAS

Table 5-1 Reaction during the solidification of AlSi7Cu3 alloy

Table 5-2 Variation of solidification time and SDAS with respect to mold temperature and cooling conditions

Table 5-3 Average chemical composition of the synthetic Al-Si alloys containing different Si and Cu content

Table 5-4 Characteristic reaction in Al-Si7 and Al-Si9 alloys containing different Cu contents

Table 5-5 Chemical composition of AlSi7Cu3 alloy containing different Ti contents

Table 5-6 Characteristic reaction in AlSi7Cu3 containing different Ti contents

Table 5-7 Chemical composition of Al-Si-Cu alloys containing different Zn content

Table 5-8 Characteristic reactions in AlSi7Cu3 containing different Zn contents

Table 5-9 Chemical composition of AlSi7Cu3 alloy containing different Mg contents

Table 5-10 Characteristic reactions and temperatures in AlSi7Cu3 alloy containing Mg

Table 5-11 Chemical composition of AlSi7Cu3 alloy containing different Sr contents

List of figures:

Fig. 3-1 Hierarchical classification of various casting processes

Fig. 3-2 Example of cylinder heads with gating system poured by gravity a) top casting b) bottom casting and c) tilt casting

Fig. 3-3 Example of engine and appropriate cylinder head

Fig. 3-4 Car engine cylinder head and demands on SDAS in outer and inner part of cylinder in combustion chamber area

Fig. 3-5 Solidification under equilibrium conditions

Fig. 3-6 Binary Phase Diagram and equilibrium solidification

Fig. 3-7 Solidification under non-equilibrium condition

Fig. 3-8 Link between the Constitutional Phase Diagram and Constitutional Undercooling

- Fig. 3-9 Transition in Growth Morphology
- Fig. 3-10 Growth of the tip of dendrites
- Fig. 3-11 Dendritic structure
- Fig. 3-12 Feeding of mushy zone during the solidification (a) mass; (b) interdendritic feeding
- Fig. 3-13 Cooling Curve Time Derivative and Base Line Obtained by Thermal Analysis of AlSi7Cu4 alloy (unrefined and unmodified)
- Fig. 4-1 Design of laboratory experiments
- Fig. 4-2 Tilt Pouring Gravity Die Casting Process
- Fig. 4-3 In situ thermal analysis on the real casting of Al-Si7Cu3 alloy
- Fig. 4-4 Positions of thermocouples in cylinder head
- Fig. 4-5 Sampling and measurement of SDAS in AlSi7Cu3 cylinder head
- Fig. 4-6 Design of permanent metal mold
- Fig. 4-7 Experimental conditions
- Fig. 4-8 Position of thermocouples in mold cavity and in casting
- Fig. 4-9 Representative points on the cooling curve of the AlSi7Cu3 alloy
- Fig. 4-10 Linear interception method
- Fig. 4-11 Scanning Electron Microscope JEOL JSM 5410
- Fig. 4-12 Principle of computer tomography (CT)
- Fig. 4-13 Sub- μ CT -System at the Institute Fraunhofer EZRT, Fürth
- Fig. 4-14 Edge blurring by limited focal spot size
- Fig. 4-15 Simulation of solidification process of AlSiCu alloy in the permanent metal mold using Simtec/WinCast software
- Fig. 5-1 Light optical microphotograph of the basic alloy, AlSi7Cu3
- Fig. 5-2 SEM microphotograph of the basic AlSi7Cu3 alloy
- Fig. 5-3 EDS Spectrum of the phase field ‘‘0’’ in the basic alloy
- Fig. 5-4 SEM Photograph and EDS Spectrum of the phase field ‘‘1’’ in the basic alloy
- Fig. 5-5 SEM photograph and EDS Spectrum of the phase field ‘‘2’’ in the basic alloy
- Fig. 5-6 SEM photograph and EDS Spectrum of the phase field ‘‘3’’ in the basic alloy
- Fig. 5-7 SEM photograph and EDS Spectrum of the phase field ‘‘4’’ in the basic alloy
- Fig. 5-8 SEM photograph and EDS Spectrum of the phase field ‘‘5’’ in the basic alloy
- Fig. 5-9 CT sample and 3D Rendation with the 2D Reconstruction of the Slice ‘‘0’’
- Fig. 5-10 Absorption coefficients of the main alloying elements in AlSi7Cu3 alloys
- Fig. 5-11 Computer aided cooling curves recorded in cylinder head
- Fig. 5-12 SDAS values in the combustion chamber area of AlSi7Cu3 cylinder head

- Fig. 5- 13 Variation of SDAS as a function of mold temperature and cooling conditions
- Fig. 5-14 Simulation results and the appropriate microphotograph of AlSi7Cu3 alloys for mold temperatures: a) 350 °C, b) 300 °C and c) 250 °C without water cooling of mold
- Fig. 5-15 Simulation results and the appropriate microphotograph of AlSi7Cu3 alloys for mold temperatures: a) 350 °C, b) 300 °C and c) 250 °C with water cooling of mold
- Fig.5-16 Experimental SDAS values versus calculated SDAS values of AlSi7Cu3 alloy solidified in the permanent metal mold
- Fig. 5-17 The effect of pouring temperature on SDAS in Al-Si7-Cu3 alloy
- Fig. 5-18 Cooling curves and microphotographs of Al-Si7 and Al-Si9 alloys containing 1, 2 and 4 wt% Cu
- Fig. 5-19 Effect of different Cu contents on the $T^{\alpha,den}_{nuc}$ and $T^{\alpha,den}_{coh}$ temperatures in the Al-Si7 and Al-Si9 alloys
- Fig. 5-20 Effect of Cu on $T^{Al-Si}_{E, nuc}$ and $T^{Al-Cu}_{E, nuc}$ eutectic temperatures in Al-Si7 and Al-Si9 alloys
- Fig. 5-21 Solidus temperatures of Al-Si7 and Al-Si9 alloys containing different Cu contents
- Fig. 5-22 Effect of Cu on the SDAS in Al-Si7 and Al-Si9 alloys
- Fig. 5-23 Influence of Cu on t_f and SDAS in AlSi7 and AlSi9 alloys
- Fig. 5-24 Influence of Cu on $\Delta\tau^*$ and SDAS in AlSi7 alloy
- Fig. 5-25 Influence of Cu on $\Delta\tau^*$ and SDAS in AlSi9 alloy
- Fig. 5-26 Cooling curves and microphotographs of AlSi7Cu3 alloy containing different Ti contents
- Fig. 5-27 Effect of Ti on $T^{\alpha,den}_{nuc}$ and $T^{\alpha,den}_{dcp}$ temperatures in AlSi7Cu3 alloy
- Fig. 5-28 Effect of Ti on $T^{Al-Si}_{E, nuc}$ and $T^{Al-Cu}_{E, nuc}$ in AlSi7Cu3 alloy
- Fig. 5-29 Effect of Ti on T_{sol} in AlSi7Cu3 alloy
- Fig. 5-30 Effect of Ti on the SDAS in AlSi7Cu3 alloy
- Fig. 5-31 Influence of Ti on t_f and SDAS in AlSi7Cu3 alloy
- Fig. 5-32 Influence of Ti on $\Delta\tau^*$ and SDAS in AlSi7Cu3 alloy
- Fig. 5-33 Cooling curves and microphotographs of AlSi7Cu3 alloy containing different Zn contents
- Fig. 5-34 Effect of Zn on $T^{\alpha,den}_{nuc}$ and $T^{\alpha,den}_{dcp}$ temperatures in AlSi7Cu3 alloy
- Fig. 5-35 Effect of Zn on T^{Al-Si}_{nuc} and T^{Al-Cu}_{nuc} temperatures in AlSi7Cu3 alloy
- Fig. 5-36 Effect of Zn content on T_{sol} in AlSi7Cu3 alloy
- Fig. 5-37 Effect of Zn on the SDAS in AlSi7Cu3 alloy
- Fig. 5-38 Influence of Zn content on t_f and SDAS in AlSi7Cu3 alloy

- Fig. 5-39 Influence of Zn content on $\Delta\tau^*$ and SDAS in AlSi7Cu3 alloy
- Fig. 5-40 Cooling curves and microphotographs corresponding to minimum, medium and maximum Mg content in AlSi7Cu3 alloy
- Fig. 5-41 Effect of Mg content on $T_{nuc}^{\alpha,den}$ and $T_{coh}^{\alpha,den}$ in AlSi7Cu3 alloy
- Fig. 5-42 Effect of Mg content on $T_{E,nuc}^{Al-Si}$ and $T_{E,nuc}^{Al-Cu}$ temperatures in AlSi7Cu3
- Fig. 5-43 Effect of Mg content on T_{sol} temperature in AlSi7Cu3 alloy
- Fig. 5-44 Influence of Mg on the SDAS in AlSi7Cu3 alloy
- Fig. 5-45 Influence of Mg on the SDAS and t_f in AlSi7Cu3 alloy
- Fig. 5-46 Influence of Mg on the SDAS and $\Delta\tau^*$ in AlSi7Cu3 alloy
- Fig. 5-47 Cooling curves and the corresponding microphotographs of AlSi7Cu3 alloy containing 1 and 143 ppm Sr
- Fig. 5-48 Influence of Sr addition on the $T_{E,G}^{Al-Si}$ and $\Delta T_{E,G}^{Al-Si}$ in AlSi7Cu3 alloy
- Fig. 5-49 Influence of Sr addition on the $T_{E,NUC}^{Al-Cu}$ and total fraction of Cu-bearing phases in AlSi7Cu3 alloy
- Fig. 5-50 Influence of Sr on the SDAS value in AlSi7Cu3 alloy
- Fig. 5-51 The comparative effect of alloying elements on T_{liq} temperature
- Fig. 5-52 The comparative effect of alloying elements on T_{DCP}
- Fig. 5-53 The comparative effect of alloying elements on T_{Al-Si}
- Fig. 5-54 The comparative effect of alloying elements on T_{Al-Cu}
- Fig. 5-55 The comparative effect of alloying elements on SDAS
- Fig. 5-56 The comparative effect of mold temperature and pouring temperature on SDAS

Appendix

Table 1A Experimental SDAS and calculated SDAS values based on the t_f and Δt^* in Al-Si7 and Al-Si9 alloys containing 1, 2 and 4 wt%

Mathematical model	SDAS = $5.5(M t_f)^{0.33}$					
Alloy	Al-Si7			Al-Si9		
Cu, wt%	1	2	4	1	2	4
SDAS _{exp} , μm	56.8	54.4	50.2	48.7	47.2	46.1
t_f , s	1170.4	1156.0	1156.0	1135.2	1144.0	1115.0
Δt^* , s	300.4	286.4	266.4	220.4	213.8	187.2
SDAS _{calc} (based on t_f), μm	56.6	56.4	56.4	56.0	56.2	55.7
Dev', %	0.3	-3.6	-12.3	-15.1	-19.0	-20.9
SDAS _{calc} '(based on Δt^*), μm	51.9	51.1	49.9	46.9	46.4	44.4
Dev'', %	8.6	6.0	0.6	3.7	1.7	3.6

Table 2A Experimental SDAS and calculated SDAS values based on the t_f and Δt^* in AlSi7Cu3 alloy containing different Ti contents

Mathematical model	SDAS = $5.5(M t_f)^{0.33}$					
Ti, wt%	0.08	0.10	0.11	0.12	0.13	0.14
SDAS _{exp} , μm	64.1	64.5	55.9	51.2	53.2	52.0
t_f , s	981.3	999.7	912.0	803.4	726.8	718.2
Δt^* , s	83.6	121.1	112.2	47.8	90.1	67.5
SDAS _{calc} (based on t_f), μm	114.2	114.9	111.5	106.9	103.4	103.0
Dev', %	-78.2	-78.1	-99.4	-108.8	-94.4	-98.1
SDAS _{calc} '(based on Δt^*), μm	41.4	46.3	45.2	35.0	42.3	38.8
Dev'', %	35.4	28.3	19.1	31.6	20.4	25.3

Table 3A Experimental SDAS and calculated SDAS values based on the t_f and Δt^* in AlSi7Cu3 alloy containing different Zn contents

Mathematical model	SDAS = $5.5(M t_f)^{0.33}$				
Zn, wt%	0.9	1.2	1.8	2.4	2.8
SDAS _{exp} , μm	65.4	63.3	62.3	59.0	58.6
t_f , s	909.0	944.0	967.0	977.0	1003.0
Δt^* , s	223.4	220.4	203.2	196.3	180.0
SDAS _{calc} (based on t_f), μm	52.1	52.7	53.2	53.3	53.8
Dev', %	20.4	16.7	14.7	9.6	8.2
SDAS _{calc} '(based on Δt^*), μm	62.3	62.0	60.4	59.7	58.0
Dev'', %	4.8	2.0	3.1	-1.1	1.0

Table 4A Experimental SDAS and calculated SDAS values based on the t_f and Δt^* in AlSi7Cu3 alloy containing different Mg contents

Mathematical model	SDAS = $5.5(M t_f)^{0.33}$					
Mg, wt%	0.22	0.55	1.1	1.6	2.1	2.97
SDAS _{exp} , μm	66.0	63.8	56.3	52.5	51.2	48.8
t_f , s	1008.4	972.6	921.5	893.1	871.1	808.3
Δt^* , s	331.1	301.7	292.0	285.1	269.6	254.6
SDAS _{calc} (based on t_f), μm	67.7	66.9	65.8	65.1	64.6	63.0
Dev, %	-2.6	-4.9	-16.8	-24.0	-26.2	-29.0
SDAS _{calc} (based on Δt^*), μm	59.0	57.2	56.6	56.1	55.1	54.1
Dev, %	10.7	10.4	-0.5	-7.0	-7.7	-10.8

NOMENCLATURE

λ_1 (DAS)	the primary dendrite arm spacing
λ_2 (SDAS)	the secondary dendrite arm spacing
λ_3	the tertiary dendrite arm spacing
R	interface velocity
G_L	the thermal gradient in the liquid in front of dendrites
t	time
T	Temperature
t_f	the solidification time
a, b, A, C, n	the alloy constants
M	coarsening parameter
ΔH	the enthalpy of the liquid or solid due the cooling
ΔH_f	the latent heat of fusion
Δh_f	latent heat per unit volume
V	volume of metal
A	area of the casting
q_e	external heat flux
dT/dt	cooling rate
c	heat capacity
f_s	fraction solid
f_L	fraction of liquid
C_0	the initial concentration
C_s	concentration of solute in solid phase
C_L	concentration of solute in liquid phase

$T_L(T_{liq} = T_{nuc}^{\alpha,den})$	liquidus temperature
$T_s (T_{sol})$	solidus temperature
κ	partition coefficient
d	thickness of solute layer
d'	mushy zone depth
D	coefficient of diffusion of the solute in the liquid
ΔT_r	Gibbs-Thomson undercooling
ΔT_c	undercooling due to concentration difference at the solid/liquid interface
ΔT_t	undercooling due to temperature difference at the solid/liquid interface
Γ	Gibbs-Thomson coefficient
κ	curvature of solid/liquid interface
r_1, r_2	principal radii of curvature
σ	solid/liquid interface energy
Δs_f	entropy of melting
ΔG	the change of Gibbs free energy
ΔG_i	Gibbs free energy of interface
ΔG_v	Gibbs free energy of volume
Δg	the difference between the liquid and solid per unit volume
$T^{\alpha,DEN}_{MIN}$	α Al- dendrite under cooling temperature
$T^{\alpha,DEN}_G$	α Al- dendrite growth (recalescence) temperature
$T^{\alpha,DEN}_{COH}$	α Al- dendrite coherency point
$T^{Al-Si}_{E,NUC}$	Al-Si eutectic nucleation temperature
$T^{Al-Si}_{E,MIN}$	Al-Si eutectic nucleation temperature
$T^{Al-Si}_{E,G}$	Al-Si eutectic growth temperature
ΔT^{Al-Si}_E	depression of the Al-Si eutectic growth temperature

$T_{E,NUC}^{Al-Cu}$	Copper rich eutectic nucleation temperature
$T_{E,MIN}^{Al-Cu}$	Copper rich eutectic minimum temperature
$T_{E,G}^{Al-Cu}$	Copper rich eutectic growth temperature
Δt^*	the time interval between the dendrite coherency point and nucleation of the Al-Si eutectic
μ	Absorption coefficient
T_{pour}	pouring temperature of the alloy

Lebenslauf

Name: Jelena Pavlovic-Krstic, Dipl.- Ing.
geb. am: 02.01.1979.
in: Zajecar / Serbien
Staatsangehörigkeit: serbisch
Familienstand: verheiratet
Wohnort: Magdeburg



Dienstanschrift:
Institut für Fertigungstechnik und Qualitätssicherung,
Universität Magdeburg
Universitätsplatz 2, 39106 Magdeburg
Tel: +49 (0) 391 67 11 610
Fax: 49 (0) 391 67 12 420

E-mail: jelena.pavlovic@ovgu.de

1987-1994	Grundschule, "Timocki partizani" Knjazevac, Serbien
1994-1997	Gymnasium Knjazevac, Knjazevac, Serbien
	30.06.1997 Abitur
10/1997 - 12/2003	Studium der Technologie und Metallurgie, Fakultät für Technologie und Metallurgie, Universität Belgrad
	29.12.2003 Diplom
01/2004 - 10/2006	Magisterstudium an der Universität Belgrad, Lehrstuhl: Metallurgie und metallische Werkstoffe.
	04.10.2006. Magisterium
Seit 15.01.2007.	Promotion, Universität des Magdeburg, Institut für Fertigungstechnik und Qualitätssicherung, Ur- und Umformtechnik
01.03.2004 – 01.01.2007.	Wissenschaftliche Mitarbeiterin am Fakultät für Technologie und Metallurgie, Lehrstuhl für Metallurgie, Universität Belgrad
01. 10.-31.12.06.	Forschungsarbeit und Weiterbildung an der RWTH Universitäts Aachen, IME Metallurgische Prozesstechnik und Metallrecycling
Veröffentlichungen	13 zum Thema der Doktorarbeit 12 im Fachgebiet: Metallurgische Prozesstechnik und Metallrecycling
